universität innsbruck

Cryogenic Cave Carbonates from the Ural Mountains (Russia)

MSc Thesis

Töchterle, Paul, BSc

24.04.2018

Supervision:
Dr. Yuri Dublyansky

paul.m.toechterle@gmail.com

Eidesstattliche Erklärung

Ich erkläre hiermit an Eides statt durch meine eigenhändige Unterschrift, dass ich die vorliegende Arbeit selbständig verfasst und keine anderen als die angegebenen Quellen und Hilfsmittel verwendet habe. Alle Stellen, die wörtlich oder inhaltlich den angegebenen Quellen entnommen wurden, sind als solche kenntlich gemacht.

Die vorliegende Arbeit wurde bisher in gleicher oder ähnlicher Form noch nicht als Magister-/Master-/Diplomarbeit/Dissertation eingereicht.

Datum	Unterschrift

Table of Contents

Geheimnisvoll am lichten Tag

Läßt sich Natur des Schleiers nicht berauben,

Und was sie deinem Geist nicht offenbaren mag,

Das zwingst du ihr nicht ab mit Hebeln und mit Schrauben.

Goethe, *Faust. Der Tragödie erster Teil*, (1808)

Acknowledgements

After three years of working on this project, I owe my deepest gratitude to everyone involved - and there were many of them.

Firstly, I want to thank my supervisor Yuri Dublyansky for his never-ending patience, support and guidance. Christoph Spötl and Marc Luetscher provided countless thought-provoking ideas but also advice and direction when it was due. I'm particularly indebted to Gabriella Koltai for U/Th- and LA-ICP-analyses. Gabi was also heavily involved in fluid inclusion analyses and petrographic work. Additional fluid inclusion work on the SB-10 sample was done by Maialen Lopez. Pèter Nèmeth executed TEM analyses and also provided guidance in the interpretation of data. Olga Kadebskaya provided fundamental directions on how to approach morphological classification of CCCs.

And of course, I am grateful for all the people in my life that were supportive of me throughout the entire time and cheered me up during the writing phase:

My parents and my sister Nina, my dear colleagues at the Innsbruck Quaternary research group, specifically my office mates Kathi, Katee, Sam, Zhijun, Haiwei and our lab-mom Manuela.

Most of all, I owe it to my girlfriend Jana that I completed this thesis unharmed. Thanks for being there with kindness and understanding.

Abstract

Coarsely crystalline cryogenic cave carbonates (CCC_{coarse}) are widely used indicators of past permafrost conditions. Nevertheless, details of their formation with respect to macroscopic morphology, stable isotope evolution and potential metastable precursor phases are poorly understood.

CCC_{coarse} were found in 5 caves located along a north-south transect of the Ural Mountains, Russia. A comprehensive data set was generated including results of carbonate stable isotope composition, stable isotopic composition of fluid inclusion water, stable oxygen isotope thermometry, trace element composition, X-ray diffraction and transmission properties and U/Th disequilibrium dating.

Detailed petrographic characterization of the samples allows for the proposal of a morphological classification scheme for CCC_{coarse}. Non-crystallographic branching of crystallites, also referred to as crystal splitting, is identified as the mechanism enabling morphological variety in CCC_{coarse}. Splitting propensity is likely related to physico-chemical properties of the mineral forming solution such as Mg^{++} concentration and supersaturation with respect to carbonate minerals.

Numerical modelling of C and O stable isotope evolution shows that open system style degassing of CO_2 during CCC_{coarse} formation accounts for 10 – 20% of the observed isotopic trends. These results support a model of slow and continuous degassing of CO_2 via nucleation of gas bubbles in co-precipitating ice in compliance to freezing experiments.

Fluid inclusion analyses suggest that early stages of CCC_{coarse} formation take place at isotopic equilibrium between carbonate minerals and the parent solution. However, oxygen isotope fractionation ($^{18}\alpha_{cc-water} = 1.0318 \pm 0.0005$) appears to be smaller than expected from literature values extrapolated to 0°C.

Diffraction properties of a CCC_{coarse} specimen indicate that it formed via non-classical crystallisation pathways. Crystallisation by particle attachment (CPA) of poorly crystalline, or even amorphous precursor phases can explain diffraction data.

1 Introduction

Caves in karst terrains are scientifically valued for hosting archives of environmental changes over long periods of time. So-called speleothems are secondary mineral deposits that slowly form from drip- and seepage waters in caves. In doing so, they track hydro-chemical signals of the infiltrating water which can be used to gain information past precipitation or vegetation (McDermott, 2004; Fairchild and Baker, 2012). In contrast to other long-term climate archives such as ice cores or marine sediments, speleothems can be precisely dated using radiometric methods (Henderson, 2006).

Cave based paleoclimate records are usually derived from two particular types of speleothems, i.e. stalagmites and flowstones. Since the early 2000's, a newly recognised third type, referred to as cryogenic cave carbonates (CCCs), has gained momentum. CCCs are believed to form in freezing pools of water during times of thawing permafrost (Žák et al., 2018). At least 40 studies on CCCs have concerned themselves with both the process of formation, as well as the paleoclimatic implications of CCCs (Lacelle et al., 2006; Richter et al., 2008; Richter and Riechelmann, 2008; Spötl, 2008; Žák et al., 2008; Žák et al., 2009; May et al., 2010; Richter et al., 2010; Žák et al., 2012; Luetscher et al., 2013; Chaykovskiy et al., 2014; Dublyansky et al., 2014; Kluge et al., 2014a; Kluge et al., 2014b; Bartolomé et al., 2015; Dublyansky et al., 2015; Colucci et al., 2017; Pavuza and Spötl, 2017).

CCCs are categorized into two subtypes: CCC_{fine} and CCC_{coarse}. The wording suggests discrimination based on grain size. However, these terms refer to two very different genetic models that will be introduced hereafter. Grain size is only a symptomatic property and the discrimination is ill-defined. The diagnostic property between both types is in fact the stable isotopic signature of CCCs (figure 1-1). CCC_{coarse} show unusually low $\delta^{18}O_{cc}$ values accompanied by relatively heavy $\delta^{13}C_{cc}$ composition compared to common speleothems. In large specimen, a negative trend is commonly observed. CCC_{fine} on the other hand are typically enriched with respect to both ^{18}O and ^{13}C.

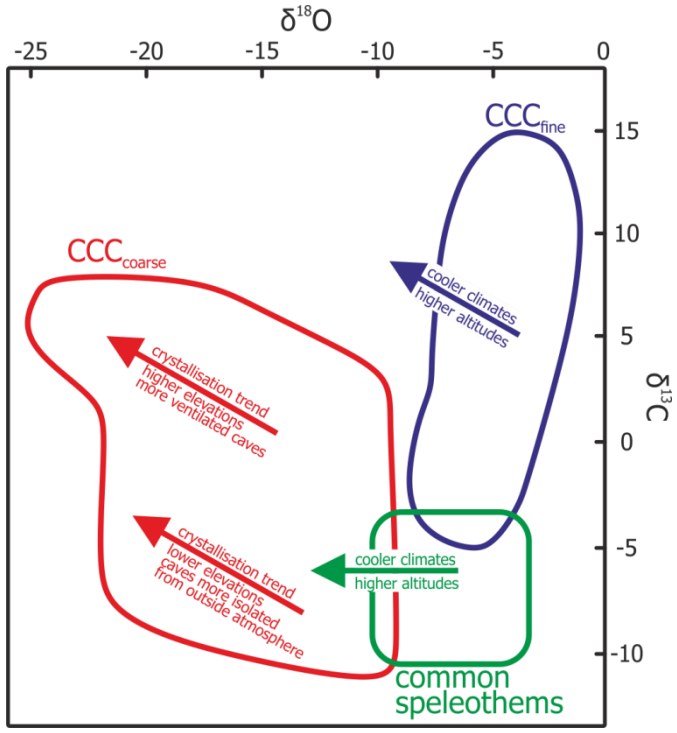

Figure 1-1: The difference between CCC_{coarse}, CCC_{fine} and common speleothems based on C and O stable isotopes. Fields delineate where the areas where reported CCC specimen are plotting. Diagram modified from (Žák et al., 2018).

1.1 Genetic model

Žák et al. (2004) were the first to present a coherent model explaining the isotopic trends observed in CCCs. The enigmatically depleted $\delta^{18}O_{cc}$ values as low as -30‰ [VPDB] found in CCC_{coarse} inspired the idea of co-precipitation of carbonate minerals and ice. As water freezes, heavy ^{18}O is preferentially incorporated in the ice, leaving the residual liquid depleted. Minerals forming from this residual liquid phase will reflect this depletion in their $\delta^{18}O$ signature.

Mineral formation assumes a critical level of saturation which may or may not be the case for natural waters in caves. However, freezing of water can force saturation. Most ions dissolved in water are not very soluble in ice and are only incorporated into the crystal lattice at high supersaturation (Killawee et al., 1998). During freezing of water, solutes accumulate in the residual aqueous solution to the point where (super-) saturation is reached. This process will be hereafter referred to as *freezing induced supersaturation* (FIS). FIS is the generalized concept of cryogenic mineral formation. In caves however, the process can be dissected further.

1.1.1 CCC_{fine} formation

As a thin film of water freezes onto a pre-existing iced surface, FIS leads to rapid degassing of isotopically light CO_2. The $\delta^{13}C$ value of residual HCO_3^- rises accordingly. For solutions saturated with respect to $CaCO_3$, degassing of CO_2 will cause precipitation of carbonate minerals according to equation (1):

$$Ca^{++} + 2\,HCO_3^- \leftrightarrow CaCO_3 + H_2O + CO_2 \uparrow \quad (1)$$

The precipitated minerals will be significantly enriched in ^{13}C. As a result of evaporation during freezing, precipitates are also slightly enriched in ^{18}O. Fine grained powders with such isotopic compositions forming in close proximity to ice have been reported previously from numerous environments such as Aufeis formations in arctic Canada (Clark and Lauriol, 1997), the Antarctic dry valleys (Nakai et al., 1975) and are even suspected to exist on Mars (Socki et al., 2010).

In caves, evaporation and rapid degassing of CO_2 are processes commonly observed in well ventilated chambers close to the entrance, where air exchange with the outside atmosphere inhibits isotopic or chemical equilibration of the system. This situation consequently can be described as an *open system*. The genetic model for CCC_{fine} is well established and validated by numerous modern analogues (e.g. Clark and Lauriol, 1992; Lacelle et al., 2009).

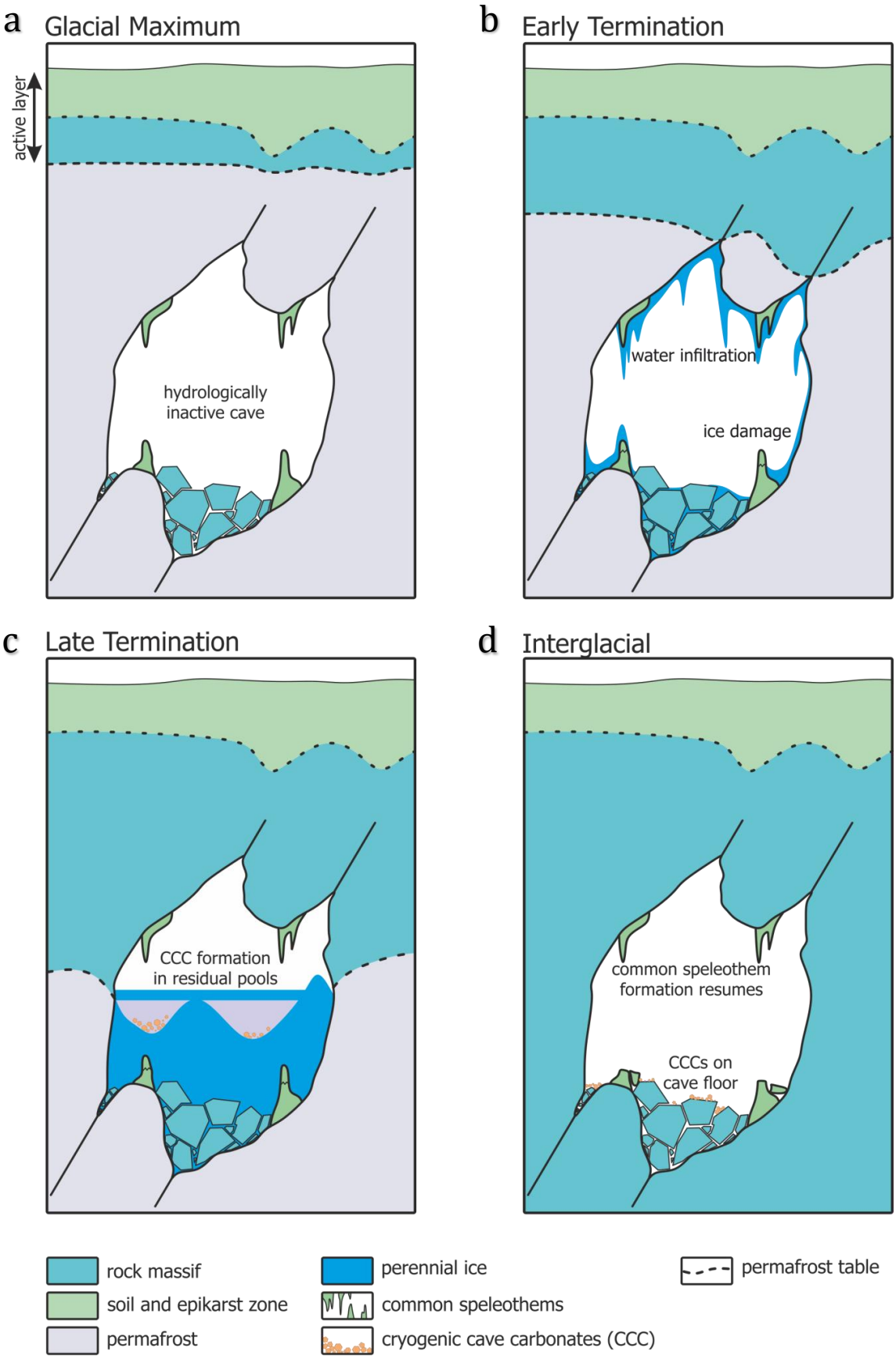

Figure 1-2: Paleoclimatic interpretation of CCC_{coarse} formation, modified after Žák et al. (2012). **a)** Hydrologically inactive cave surrounded by permafrost during glacial conditions. **b)** Water infiltration as the seasonally thawing active layer intercepts the cave ceiling. A body of ice will form. **c)** Further thawing allows for the formation of large pools of water that slowly freeze. FIS triggers precipitation of CCC_{coarse}. **d)** During full interglacial conditions CCC_{coarse} are found as lose accumulations on the cave floor.

1.1.2 CCC_{coarse} formation

The genesis of CCC_{coarse} is more elusive. As mentioned before, many samples show extraordinarily low $\delta^{18}O_{cc}$ values which separate them from their fine-grained counterpart. Numeric modelling has confirmed that such low values can be explained by Rayleigh fractionation in a water-ice-carbonate system (Žák et al., 2004; Kluge et al., 2014a). The proposed model envisages a static, slowly freezing pool of water as the CCC–forming environment. CO_2 escape and evaporation must be limited to produce the observed isotopic trend. This could be brought about by an ice "lid" (Kluge et al., 2014a) but solid evidence for this hypothesis is lacking.

The described environment is uncommon in caves today. In fact, the only report of modern CCC_{coarse} formation has been published recently by Colucci et al. (2017). The occurrence of CCC_{coarse} is commonly attributed to thawing permafrost conditions (Žák et al., 2008; Richter et al., 2010; Žák et al., 2012; Luetscher et al., 2013; Spötl and Cheng, 2014).

Figure 1-2 depicts the process in a conceptual fashion. During climatic cold periods, periglacial environments are strongly affected by permafrost. Karst caves are hydrologically inactive because water infiltration is inhibited by permafrost (figure 1-2a). As climate warms, the active layer (i.e. a zone where soil and bedrock thaw seasonally) gradually grows in thickness. At one point, the permafrost table will intercept the cave ceiling and seepage pathways open. Water will enter the cave environment that is still colder than 0 °C and freezing will ensue. Continuous infiltration will eventually lead to the formation of a large body of perennial ice in the cave (figure 1-2b). Frost damage like broken stalagmites can be identified as artefacts of extensive cave ice formation. As permafrost degradation progresses, pools of drip water can form on top of the perennial ice body. Slow freezing of such a pool will trigger FIS which potentially leads to the formation of CCC_{coarse} in isolated pockets of residual solution (figure 1-2c). With the progression of the glacial termination the permafrost table will continue to drop and ice bodies inside the cave will thaw completely. During full interglacial conditions (figure 1-2d) permafrost will have receded entirely and CCC_{coarse} will be left as lose accumulations on the cave floor (figure 1-3).

Figure 1-3: Typical occurrence of CCC_{coarse} in the field. Light coloured patches with lose grains up to several cm in diameter cover a collapse section of the cave floor in Vodorazdelnaya Cave, east Sayan, Russia. (Foto courtesy of Y. Dublyansky)

Depending on the depth of the cave, this process is susceptible to repetition as climate fluctuates (Žák et al., 2012). Preliminary results indicate that CCCs found in Great Britain even reveal the permafrost response to Daansgard-Oeschger oscillation during the last glacial cycle (Luetscher et al., 2017).

1.2 The Focal Points of this Thesis

The climatic interpretation of CCC_{coarse} as markers of permafrost degradation seems to be firmly established. However, the very process of formation through FIS remains poorly understood. In this thesis, three open questions will be addressed.

1.2.1 Isotopic Evolution and the Mechanisms of CO_2 Escape

The C and O stable isotope composition of CCC_{coarse} as depicted in figure 1-1 supports the model of precipitation during progressive freezing of water in a system that partially restricts evaporation and degassing of CO_2. This general description however fails to provide an in-depth picture of what such a system would look like in nature.

The established interpretation is that of an ice-capped pool of water. Yet, this model faces the problem that CO_2 must escape somehow for carbonate precipitation to be possible. In a completely closed system, CO_2 would accumulate in the solution, lowering pH and inhibiting $CaCO_3$ precipitation. Two possible mechanisms for the degassing of CO_2 are currently being discussed within the CCC community.

- The *soda can* model assumes that pressure builds up underneath an ice lid due to degassing of CO_2 and other gaseous compounds. This lid eventually fractures and lets CO_2 degas analogous to a can of soda, forcing carbonate minerals to precipitate from the residual solution. This model has not been exhaustively mentioned in the literature so far and is based on personal communication about field observations in modern ice caves with M. Luetscher, Y. Dublyansky, C. Spötl and G.M. Moseley.
- The second model envisages the nucleation of gaseous bubbles that are subsequently incorporated into ice. Experimental studies have confirmed the formation of gaseous inclusions in ice due to increasing supersaturation (Killawee et al., 1998), but there is no evidence to suggest that this process contributes to the isotopic composition of CCC_{coarse}.

Through detailed examination of stable isotope transects of CCC_{coarse} specimens, fluid inclusion analyses and petrographic observations, the formational processes of CCC_{coarse} are discussed (section 6.1). A numerical model (chapter 5) helps to understand effects of degassing to the stable isotopic composition of CCC_{coarse} quantitatively.

1.2.2 Morphology

CCC_{coarse} come in a vast variety of shapes and sizes. This morphological diversity has been appreciated by the scientific community but the reasons for it are unknown. Petrographic studies on common speleothems have revealed close links between crystal fabrics and physico-chemical properties of cave water (e.g. Frisia et al., 2000; Mattey et al., 2010; Frisia, 2015). A similar connection for CCC forming environments is hypothesized. By investigating CCC_{coarse} petrographically and comparing mineral fabrics to results from chemical and crystallographic analyses, a causal connection between the morphology of CCC_{coarse} and formational processes will be discussed (section 6.2). Moreover, a morphological classification scheme based on this hypothesis is proposed (section 4.1).

1.2.3 Precursor Phases

Precursors are of interest to CCC research for two main reasons. i) Evidence of precursor phases could further improve the understanding of CCC formation, especially with respect to morphology and isotopic evolution. ii) Recrystallization and/or dehydration processes could lead to open system behaviour with respect to U and consequently introduce dating biases. A solid understanding of potential metastable precursors to calcite could help in sample selection for paleoclimate reconstructions.

All studies that have analysed CCCs with X-ray diffraction methods have reported calcite as the only occurring mineral. Yet, it was recurrently mentioned that metastable phases could initially form and only recrystallize to calcite after temperature inside the cave has risen (Žák et al., 2004; Žák et al., 2018). This notion is inspired by the fact that minerals like vaterite (μ-$CaCO_3$) and hydrated $CaCO_3$ polymorphs like monohydrocalcite ($CaCO_3 * H_2O$) and ikaite ($CaCO_3 * 6\ H_2O$) are reported frequently from environments with sub-zero conditions (e.g. Jansen et al., 1987; Grasby, 2003; Dahl and Buchardt, 2006).

Results from structural and chemical analyses (sections 4.2.5, 4.2.6 and 4.2.7) provide clues on the existence of metastable precursor phases in CCC_{coarse} that complement the enhanced genetic interpretation of stable isotopes and crystal morphology (section 6.3).

2 Study Sites

The samples presented herein were found in 5 different caves spread out over a north-south transect through the Eurasian continent along the Ural Mountains (table 2-1). Today, none of the studied sites show permafrost and are free of perennial ice bodies. Cave surveys with markers of sample locations and an overview map featuring modern permafrost extent (Kotlyakov and Khromova, 2002) are presented in the appendix.

In all cases, CCC_{coarse} were found in large chambers at least 100 m from the entrance. Monitoring of temperature reveals stable microclimates with positive temperatures between 5 and 7 °C and poor ventilation (Y. Dublyansky, pers. comm.). CCC_{coarse} are absent from smaller chambers and narrow passages in studied caves.

Table 2-1: List of caves where samples presented in this study were found, listed from north to south.

Cave Name	Region	Abbreviation	Latitude [°N]	Longitude [°E]	Elevation [m a.s.l]
Div'ya	Northern Ural	DIV	61.797	56.725	240
Viasherskaya	Central Ural	VIA	59.088	57.656	335
Rossiyskaya	Central Ural	ROS	58.850	57.607	335
Usvinskaya	Central Ural	USV	58.690	57.609	245
Victoria	Southern Ural	VIC	53.049	57.045	271

3 Methods

3.1 Optical Petrography

Doubly polished sections between 150 and 400 µm in thickness were manufactured from 19 samples, using SiC sand paper and diamond suspension as abrasives. These thick sections were investigated microscopically under transmitted light and epifluorecent blue-light. Additionally, microscopic images of whole specimens were made using a Keyence VHX900 digital microscope.

3.2 Carbonate Stable Isotope Analysis

Analyses of $\delta^{13}C_{cc}$ and $\delta^{18}O_{cc}$ of carbonate samples were performed at the University of Innsbruck. Large specimens were cut and polished with SiC powder and diamond suspension. Powders for analysis were drilled at a resolution of 250 µm along linear transects using a high precision milling machine. If the complex geometry of a sample does not allow for a continuous trace to be drilled, powders were hand-drilled from prominent layers using a diamond-tipped dental drill. For sample NU8 individual specimens were hand-picked from the main sample based on their morphology. Grains smaller than 4 mm were ground in an agate mortar and 3 aliquots of the powder were separated for analysis. For grains larger than 4 mm at least 2 aliquots (e.g. core & rim of the specimen) were drilled with a diamond tipped dental drill.

Samples designated for thermometric calculations were taken from the crushed material left over after fluid inclusion stable isotope analyses. These powders were removed from the crushing devices immediately after analyses and transferred to plastic vials. Samples were then homogenised by thoroughly shaking the plastic vial before 3 aliquots were separated for carbonate stable isotope analysis. The $\delta^{18}O_{cc}$ and $\delta^{13}C_{cc}$ values reported in the results section of this thesis in the context of fluid inclusion analysis and thermometry are the mean values of these aliquot measurements.

Sample amounts used for stable isotope analysis were typically between 0.10 and 0.80 mg. All stable isotope measurements were done on a Thermo Scientific Delta V Plus isotope ratio mass spectrometer (IRMS) connected to a GasBench II interface (Spötl and Vennemann, 2003). After correction to in-house reference material, the setup typically performs at a precision (1σ) of ± 0.06 ‰ for $\delta^{13}C_{cc}$ and ± 0.08 ‰ for $\delta^{18}O_{cc}$ (Spötl, 2011).

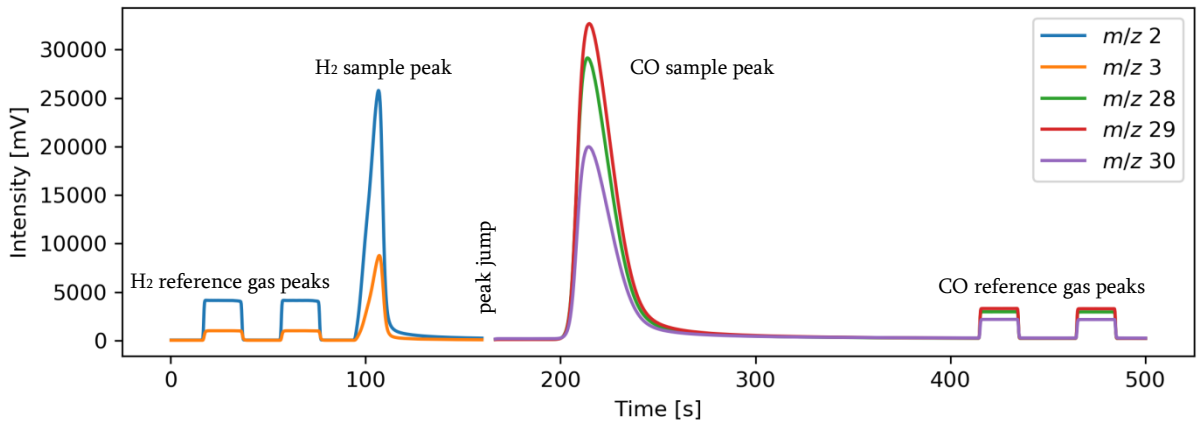

Figure 3-1: Chromatogram of a fluid inclusion analysis derived from a measurement on sample SB10. The left half of this diagram shows the part of the measurement dedicated to determining the δ^2H values of the sample while the part right of the peak jump is dedicated to determining the $\delta^{18}O$ of the evolved CO. Each colour corresponds to the output trace of a single detector that has been tuned to pick up the signal of a specific mass/charge ratio (m/z).

3.3 Fluid Inclusion Analysis

3.3.1 Experimental setup

Analyses to determine the isotopic composition of aqueous fluid inclusions (δ^2H_{water} and $\delta^{18}O_{water}$) were carried out at the stable isotope facilities at the University of Innsbruck. The setup comprises a custom built crushing device (Dublyansky, 2012) in line with a cryo-trapping unit, a Thermo Scientific TC/EA pyrolysis reactor equipped with a molecular sieve for gas chromatography, a Thermo Scientific Con-Flo II interface and a Thermo Scientific Delta V Advantage IRMS. The working principle of this method was described in detail by Dublyansky and Spötl (2009). In short, the aqueous fluid inclusions entrapped in the sample material are released by crushing a sample aliquot at 110 °C. The released fluid evaporates and is transported via a continuous flow of helium into a cryo-trapping cell that can be cooled to -150 °C. When the fluid has evaporated entirely and accumulated inside the cryo-trapping cell, it is released again by flash-heating it to 100 °C and transferred by helium flow to the TC/EA reactor where a pyrolysis reaction with glassy carbon at 1400 °C produces the measurable gases H_2 and CO (eq. 2).

$$H_2O + C \xleftrightarrow{1400\,^{\circ}C} H_2 \uparrow + CO \uparrow \quad (2)$$

The evolved gases are passed through a molecular sieve and analysed sequentially in the IRMS. The result of this procedure is a chromatogram with separate traces for each of the relevant isotopologues (figure 3-1). The area occupied by a peak is proportional to the concentration of the corresponding isotopologue. Therefore, the ratio between two peak areas is proportional to the isotopic ratio.

3.3.2 Data correction and calibration

To determine a sample's δ-value, it is necessary to compare its isotope ratio to a reference gas with a known δ-value. An algorithm that considers the influence of electronic signal amplifiers, backgrounds and a range of other factors returns an instrument-scale δ-value that has been calibrated against in-house reference gases for H_2 and CO.

Conversion of the instrument-scale values to VSMOW standard is done by calibration against in-house reference waters, which, in turn, are calibrated against International Atomic Energy Agency (IAEA)-supplied standards VSMOW, SLAP and GISP. These in-house reference waters are injected into a designated port on the crushing device with a syringe. Apart from the act of injecting, the measurement procedure for the reference waters is the same as for actual samples.

Every day, two isotopically distinct in-house standard waters are measured three to five times each with varying amounts between 0.2 and 0.5 µL. Results for injection volume, peak area and instrument scale δ-values are transferred to a spreadsheet where calibration lines are generated to account for amount-dependent fractionation occurring during freezing, flash heating or pyrolysis.

3.3.3 Water amount and content

The described method also allows for calculation of water yield from a measurement and specific water content in the sample material. A linear model (injection volume [µl] = a * area [Vs] + b) is fitted to the data derived from in-house standard measurement for H_2. This model is then used to calculate the water volume released by the crushing of a sample. The water content [µl g^{-1}] is subsequently determined by normalising the volume to the weight of the sample. The precision of this method is limited by the efficiency of crushing which in turn is determined by the size of the sample. Also, sometimes a sample is deliberately not crushed completely to optimize the water amount for analysis. In such cases, the water content will be underestimated.

3.3.4 Analytical uncertainty

Product specifications by the manufacturer for standard setup[1] report an analytical precision of ±0.2 ‰ for $\delta^{18}O$ and ±2 ‰ for $\delta^{2}H$ respectively (Kracht and Hilkert, 2016). However, because the system used for this study replaced the auto sampler with custom built peripherals, the manufacturer's numbers cannot be transferred to this specific setup. Consequently, the precision of this setup was determined by repeated measurements of a standard material.

[1] The standard setup consists of an auto sampler, a TC/EA unit, a ConFlo II interface and a Delta V Advantage IRMS.

Additionally, tests have shown that shifts in the measured isotopic composition frequently occur on crushed samples that do not occur on injections of water standards. This observation gives rise to speculations about unknown processes associated with the act of crushing itself affecting the results. To account for these enigmatic effects, a mineral standard that hosts aqueous fluid inclusions with known isotopic composition is needed.

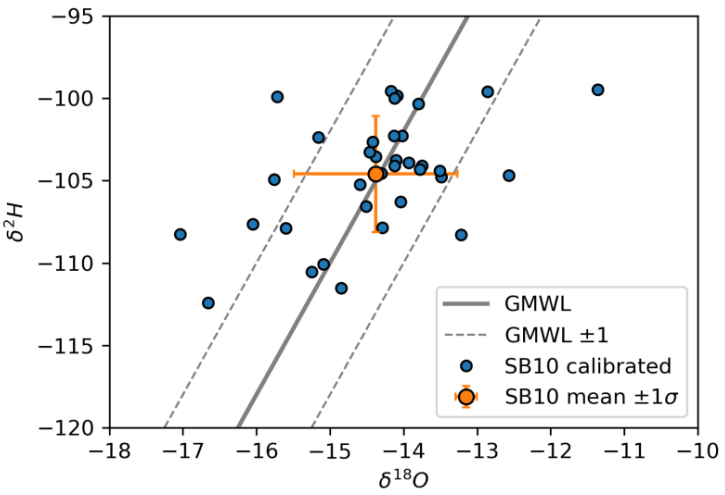

Figure 3-2: Results from 35 measurements on aliquots of reference sample SB10 (blue dots). The mean value of these measurements as well as the 1σ spread of the data is indicated in orange. Also, the global meteoric water line (GMWL: $\delta^{18}O = 8^* \delta^2H + 10$) is depicted with a margin of ±1‰ $\delta^{18}O$. All values are reported on the VSMOW scale.

Ideally, a standard material would be synthetic calcite hosting aqueous fluid inclusions of known composition. However, at this point in time no such material is commercially available. Therefore, natural calcite crystals (sample ID: *SB10*) from a hypogene karst system (Dublyansky et al., 2009) that are believed to be reasonably homogeneous with respect to the isotopic composition of their fluid inclusions were chosen as a standard. Overall 43 measurements were performed over the course of 16 days. Only results that yielded water amounts between 0.1 and 0.6 µL were evaluated, which equates to a total of 35 measurements that are plotted in figure 3-2. Calculated averages and standard deviations from these data are $\delta^{18}O_{water}$ = -14.3 ±1.1 ‰ and δ^2H_{water} = -104.7 ±3.4 ‰ against the VSMOW standard. This mean isotopic composition is on the global meteoric water line, consistent with the genetic interpretation for this calcite published in the literature (Dublyansky et al., 2009).

Assuming that the spread of the data is caused by methodological parameters rather than the natural variability of the isotopic composition of fluid inclusions in the sample, the standard deviation may be interpreted as an empirically derived analytical uncertainty for this method. However, this assumption is most likely not justified because a contribution of natural variability cannot be excluded without further constraints. Using the derived standard deviations as analytical errors is therefore a rather conservative approach because it is likely to include natural variability on top of analytical uncertainty.

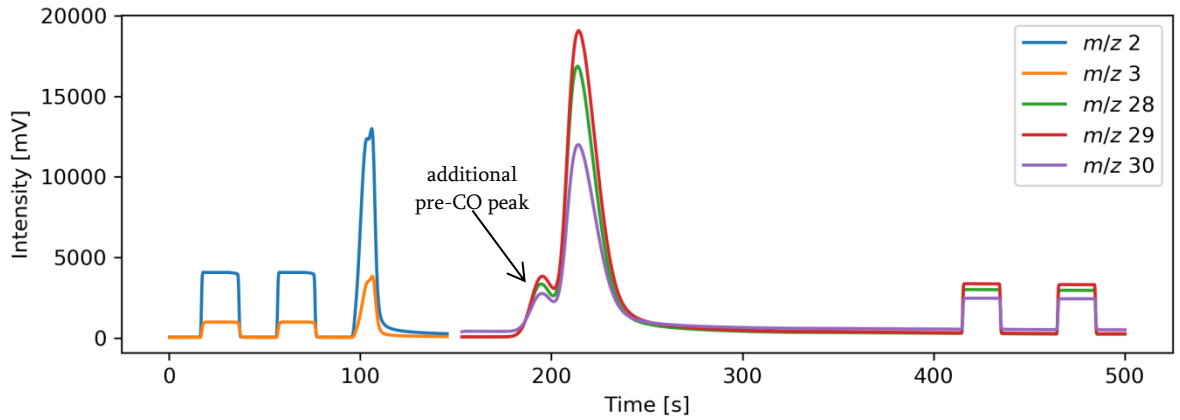

Figure 3-3: Chromatogram of a fluid inclusion analysis performed on a CCC sample. The peak shape differs notably from figure 3-1. Especially the CO part of the chromatogram shows a pronounced double peak on all measured m/z ratios.

3.3.5 Gas chromatography and the peak detection problem

As with all spectrometric methods, the quality of fluid inclusion stable isotope results hinges on the accuracy of peak- and background detection. Depending on how the peak start and end times as well as the backgrounds are defined, the calculated isotopic ratios will be altered. As was briefly mentioned in section 3.3.2, the default method employs an automated peak- and background detection. Therein, the start and end time of a peak are defined as the moment when the slope of a detector trace (i.e. m/z 2 for H_2 and m/z 28 for CO) surpasses 2 mV s^{-1} or falls below 4 mV s^{-1}, respectively. The background value for this peak is defined as the intensity value at the starting point for each measured m/z ratio.

The method as described so far is reliable for *'clean'* samples, meaning that the fluid entrapped in the inclusions is chemically similar to 'normal' meteoric water and does not contain noteworthy amounts of contaminants. Gaseous inclusions may also cause unwanted but indiscernible contributions to the overall signal. As shown in figure 3-3, some samples distinctly show additional peaks besides the ones corresponding to H_2 and CO. In most of these cases, an additional peak is slightly overlapping the rising leg of the main CO peak. The relative intensity of this small *'pre-CO peak'* compared to the main CO peak is highly variable. The origin of this additional peak is unknown.

Figure 3-4 shows a close-up view of a pre-CO peak partly overlapping the main CO peak. Based on the automated peak detection algorithm, a start point (start 1) and end point (end) have been defined. Following this definition, both the main CO peak

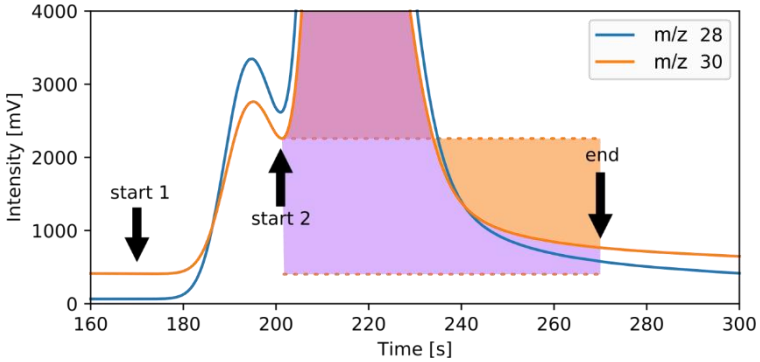

Figure 3-4: Close-up view of the main CO peak from figure 3-3. Only m/z traces relevant to $\delta^{18}O$ calculation are depicted. Dashed lines delineate the background of m/z 28 intensity values at start 1 and start 2 respectively. Shaded areas correspond to the calculated areas based on these backgrounds: pink – area occupied by either of the background values; lilac – area exclusive to the background value from start 1; orange – area exclusive to the background value from start 2. Note that the orange area will receive a negative sign.

as well as the pre-CO peak will be used to calculate the peak area and subsequently the area ratio. The area ratio is proportional to the isotopic ratio.

Including or excluding the pre-CO peak into area calculation will yield different $\delta^{18}O$ values. To control the influence of the pre-CO peak, the following logic for peak and background definition was applied to all analyses presented in this thesis:

- If no distinct pre-CO peak is visible (i.e. slope increasing linearly), the automated peak detection was applied.
- If a distinct pre-CO peak can be seen, the start time of the main CO peak was set manually to the local minimum between pre-CO peak and main CO peak. If no local minimum is present because of extensive overlap, the start time was set at the inflection point on the rising leg of the trace. The endpoint of the main CO peak remains unchanged from the automated peak detection.
- The starting time of the pre-CO peak itself is consequently defined as the starting time according to automated peak detection. The end time of the pre-CO peak is equal to the start point of the main CO peak at the local minimum or deflection point.
- Background values for calculation of peak areas are defined as the value at the starting time of a given peak according to this logic.

This approach may potentially lead to negative areas as illustrated in figure 3-4. Because of the strong overlap between the pre-CO peak and the main CO peak, the resulting background level defined at start 2 is much higher than at start 1.

3.4 $^{230}Th/^{234}U$ Disequilibrium Dating

^{230}Th and ^{234}U are both radiogenic isotopes within the U-series decay chain. U-Th dating is based on the very different partitioning coefficients of the U and Th in aqueous environments (Bourdon, 2003). Th is almost insoluble in water and is therefore only incorporated into minerals as adsorption on detrital inclusions. U however is readily incorporated into the crystal lattice of carbonate minerals. It is therefore assumed that a closed system completely devoid of Th is formed when a speleothem precipitates from groundwater, and, at least for clean specimens, this assumption holds true. Hence it is possible to determine the time passed since the formation through the state of disequilibrium between U and ^{230}Th isotopes until secular equilibrium is reached after approximately 600.000 years using equation 3 (Kaufman and Broecker, 1965):

$$\frac{^{230}Th}{^{234}U} = 1 - e^{\lambda^{230}Th} + 10^{-3}\delta^{234}U(t) * \frac{\lambda_{230}}{\lambda_{230} - \lambda_{234}} * \left(1 - e^{-(\lambda_{230} - \lambda_{234})t}\right) \quad (3)$$

Large CCC_{coarse} specimens over 0.5 cm in diameter were prepared for analysis by cutting with a diamond coated band saw and subsequent polishing with SiC powder and diamond suspension. Afterwards, the polished surface was cleaned with ethanol wipes and ultrasonic cleaning in de-ionized water. Based on estimates for U content of a sample between 10 and 100 mg of powder were drilled from the samples using a diamond tipped dental drill. Drilling was done in a laminar flow hood to mitigate the risk of contamination with dust particles.

Calcite grains that were too small for this procedure were only cleaned on the outside by ultrasonic cleaning in de-ionized water. Powders were generated by grinding the sample in an agate mortar. In some cases, small calcite particles were also dissolved whole in acid during chemical preparation.

Analyses were performed at the Xi'an Jiaotong University (China) by Dr. Gabriella Koltai on a Thermo Fisher Neptune Plus inductively coupled mass spectrometer. The decay constants used for age calculations were $\lambda^{238} = 1.55125*10^{-10}$ (Jaffey et al., 1971), $\lambda^{234} = 2.82206*10^{-6}$ (Cheng et al., 2013) for U and $\lambda^{230} = 9.1705*10^{-6}$ for Th (Cheng et al., 2013). $\delta^{234}U_{initial}$ was calculated based on ^{230}Th age (t), i.e., $\delta^{234}U_{initial} = \delta^{234}U_{measured} * e^{\lambda 234 * t}$.

3.5 Laser Ablation Inductively Coupled Plasma Mass Spectrometry (LA-ICP-MS)

Polished slabs of CCC_{coarse} were investigated using the laser ablation setup at Royal Holloway University of London by Dr. Gabriella Koltai. The system comprises a two-volume laser ablation cell equipped with a 193 nm ArF laser coupled to a quadrupole ICP-MS (Müller et al., 2009).

For both analysed samples, two profiles were ablated in parallel to the profile drilled for carbonate stable isotope analysis. Concentrations were determined for ^{25}Mg, ^{27}Al, ^{31}P, ^{51}V, ^{55}Mn, ^{57}Fe, ^{65}Cu, ^{66}Zn, ^{75}As, ^{85}Rb, ^{88}Sr, ^{89}Y, ^{138}Ba, ^{208}Pb and ^{238}U by normalizing the results to international standard materials NIST SRM 610 and NIST SRM 612 (Jochum et al., 2011).

3.6 Powder X-ray Diffraction (PXRD)

Samples for powder X-ray diffraction were prepared by drilling small amounts of calcite powder from the specimen using a diamond tipped dental drill. After grinding thoroughly with an agate mortar, the powders were applied between two slivers of plastic film covered in laboratory grease and mounted on a sample holder. Analyses were subsequently carried out at the Chemistry department of the University of Innsbruck on a Stoe Stadi P powder diffractometer in transmission geometry equipped with a Molybdenum X-ray tube ($\lambda(K_{\alpha 1}) = 70.93185$ pm). Scans were run over a 2Θ range between 2° and 45° with a step width of 0.7° and 20s of measurement time per step. Results were matched to a database (ICDD, 2015).

3.7 Transmission Electron Microscopy (TEM)

TEM is a technique that is used to get localised information on the crystallographic structure of a sample. The working principle (figure 3-5) is based on the interaction of a high-energy electron beam, typically between 100 and 400 keV, with a very thin sliver of a sample. Analyses yield two kinds of images:

i) A bright field image, where the sample is depicted in greyscale; the grey-scale values correspond to the relative intensity of the transmitted beam. Light areas are translucent to the electrons, dark areas block them.

ii) A selected area electron diffraction (SAED) pattern where electrons, scattered at a given angle within the sample, arrive at the same distance from the centre of the image. For mono-crystalline samples the result will be a pattern of distinctly illuminated spots where the spots position is determined by the crystal structure. Polycrystalline or amorphous materials will generate concentric ring patterns. Because of the high energy of primary radiation (i.e. short wavelength) it is possible to resolve features at a crystallographic scale, such as dislocations or artefacts of recrystallization from a precursor phase.

Powder aliquots for TEM were drilled from selected specimens using a diamond tipped dental drill. A few milligrams of the powder were dispersed over a 3mm lacey-carbon coated copper grid, which serves as a sample holder. Analyses were performed by Dr. Pèter Nèmeth at the Institute of Materials and Environmental Chemistry of the Hungarian Academy of Sciences in Budapest on a MORGAGNI 268D transmission electron microscope.

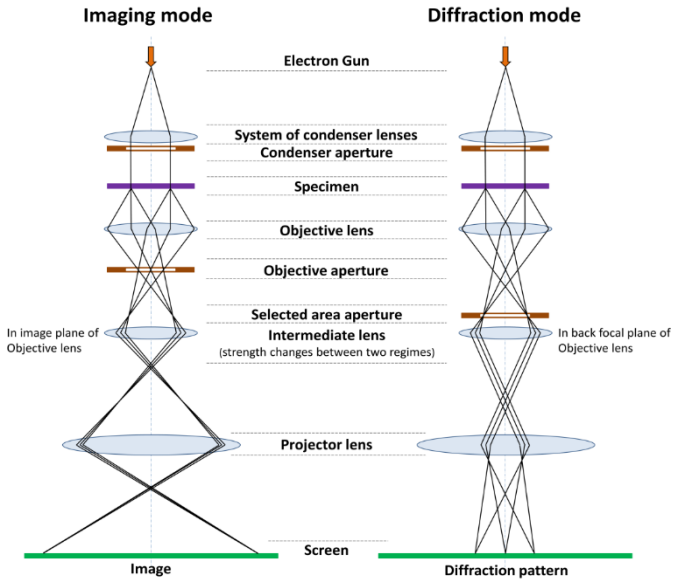

Figure 3-5: Schematic of the optical path of TEM. The imaging mode produces bright field images of the sample, while the diffraction mode generates SAED patterns. The difference lies solely in the position of the aperture.
(Image source: Wiki Commons;
https://en.wikipedia.org/wiki/Transmission_electron_microscopy)

4 Petrographic and Analytical Results

4.1 The Morphology of CCC_{coarse}

A striking feature that separates CCC_{coarse} from other generic types of speleothems is their morphological variety. In previous studies on CCC_{coarse}, authors often describe the studied samples in great detail but so far, no contribution has established a direct link between morphology and the physico-chemical properties of CCC_{coarse} such as crystal structure or chemical and isotopic composition. However, researchers tend to put great efforts into morphological characterization of their samples. Such efforts are testimony to a vague suspicion within the CCC community, that crystal morphology may hold meaningful information that can be interpreted.

4.1.1 A Brief Introduction to Speleothem Petrography

Calcite fabrics of speleothems nowadays are mostly described using a scheme by Frisia (2015). Therein, 12 different fabrics were identified and their appearance related to growth mechanisms and physico-chemical properties of the parent fluid (drip rate, saturation index with respect to calcite (SI_{cc}), Mg/Ca ratio, and pH amongst others). This approach only considers fabrics and intentionally neglects macroscopic morphology. Also, it was developed on stalagmites and flowstones and may therefore have limited applicability to other types of speleothems.

On macroscopic scales, speleothems are conventionally categorized into a scheme of multiple types and subtypes (e.g. Hill and Forti, 1986). This classification is mostly based on formational processes or simply the shape of specimen. However, many authors have struggled to characterize CCC_{coarse} within this framework which led to a sprawling list of terms being used to characterize CCC morphologies (for example the terms used in Žák et al., 2004; Richter et al., 2008; Richter and Riechelmann, 2008; Richter et al., 2010).

In the following chapter, a novel approach for classifying CCC_{coarse} is proposed. The aim is to reduce the number of terms used to describe morphological varieties to a minimum by identifying simplified *building blocks* and using these to describe more complex geometries. This is done by combining calcite fabrics and macroscopic geometry to define end-members in what appears to be a morphological spectrum. Furthermore, it is desirable for these newly introduced terms to have genetic implications and go beyond purely descriptive terminology. To achieve this goal, two fundamental concepts should be introduced. i) the model of evolving crystal morphology by Sunagawa (2005) and ii) the concept of mineral ontogeny (e.g. Grigor'ev, 1961).

The model proposed by Sunagawa (2005) relates the morphology of a crystal to physiochemical properties of the mineral forming medium (i.e. an aqueous solution in the case of speleothems) at the time of crystallisation. The model assumes three basic growth mechanisms: spiral growth, two-dimensional nucleation growth and adhesive growth (figure 4-1). Each of these mechanisms will result in a different crystal morphology. Which growth mechanism is active is determined by the driving force (eq. 4).

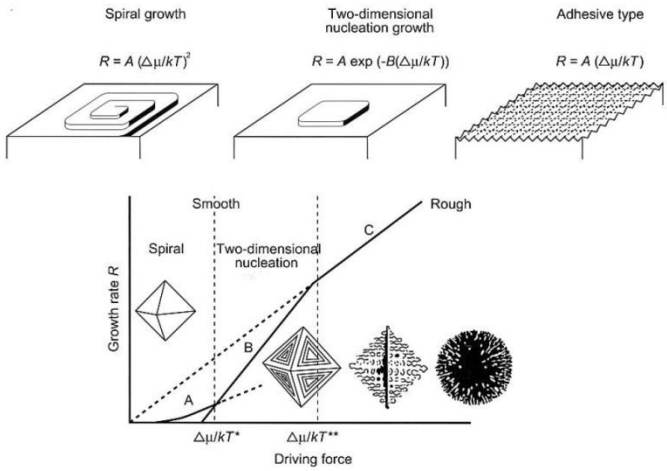

Figure 4-1: Schematic of the three fundamental mechanisms of crystal growth. The diagram shows crystal morphology as a function of growth rate and driving force. Zones A, B and C are the respective domains of the three fundamental growth mechanisms. The depicted schematics assume the driving force for crystal faces (111) (Sunagawa, 2005).

$$ln(S) = {}^{\Delta\mu}/_{kT} \qquad (4)$$

where S is the supersaturation ratio, Δμ the relative change in chemical potential introduced by crystallisation, k is the Boltzmann constant and T refers to temperature in K. For CCCs, T is quasi-constant at or slightly below 0 °C. In this case, ln(S) is solely a function of Δμ.

Accordingly, crystal morphology represents the growth mechanism and consequently also the driving force during crystallisation. However, this concept can only be applied to one type of crystal face at a time because Δμ for a given phase transition is not the same in all crystallographic directions.

According to this model, smooth euhedral crystal faces form by slow spiral growth at low supersaturation, close to equilibrium conditions. With supersaturation increasing to Δμ/kT*, two-dimensional nucleation growth will commence and produce a hopper morphology at higher growth rates. Above Δμ/kT** lies the domain of adhesive type growth which will produce stepped surfaces (Frisia et al., 2000) or dendritic patterns.

To produce spherical crystals or *spherulites* from solutions or gels, driving forces greater than Δμ/kT** are needed (Shtukenberg et al., 2012). In this driving force domain, adhesive growth can lead to non-crystallographic branching. This term refers to a crystallite splitting apart into multiple fibres during growth with a rather small angle of deflection. Depending on the rate of splitting versus the growth rate and deflection angle of the crystallites, a variety of different (sub-) spherical morphologies can develop. In theory, any crystalline material can be subject to non-crystallographic branching and crystal splitting. The splitting propensity of a crystalline substance is highly complex and depends not only on the driving force, but also on the type of crystallization medium (melts vs. solution vs. solid state matter) and a variety of physico-chemical properties thereof (foreign ion concentration, temperature, presence of ligands or impurities, etc.).

The second fundamental concept was developed in the 1950's and 1960's in Russia and is known as mineral ontogeny (e.g. Grigor'ev, 1961). This independent branch of mineralogy, however, was never really adopted by western scientists (Self and Hill, 2003). The fundamental idea is to think of a mineral specimen as a physical arrangement of different hierarchical levels of so-called minor mineral bodies (MMBs). A single mineral specimen is made up of multiple MMBs that can in turn be organized hierarchically into one or more levels. Self and Hill (2003) have found a particularly accessible way of describing this concept:

"The hierarchy scheme of MMBs is not the same as the classification of speleothems into types and subtypes […] 'Speleothem' is a descriptive term and can only be used to indicate the morphology of a MMB. In ontogeny, speleothems can appear on different organizational levels; i.e., they can be composed of individual crystals, crystal aggregates, or groups of aggregates. For example, selenite needles are individuals, flowstones and coralloids are both aggregates, but stalactites are multiaggregates."

In other words, any speleothem comprises at least one hierarchical layer of fundamental building blocks that – in mineral ontogeny – are called MMBs. MMBs are defined based on mineralogical properties such as but not limited to crystallographic orientation or chemical composition. A combination of discernible MMBs of one level generates a higher hierarchical level. In contrast to the model by Sunagawa, mineral ontogeny does not come with a-priori implications on physico-chemical properties.

4.1.2 Morphology of CCC_{coarse} from the Ural Mountains

The studied samples show diverse macro- and microscopic morphologies. All samples presented herein have been documented and studied petrographically using transmitted light microscopy and high-resolution microphotography.

4.1.2.1 Transmitted Light Microscopy

In transmitted light, CCC_{coarse} commonly show patterns that can be described as fibrous or elongate columnar fabrics, following Frisia et al. (2000) (figure 4-2a, b, d, f, g, h). Crystallites are highly elongated and oriented (sub-) radially around a common nucleation point. Towards the rim, crystallites seem to be continuously deflected by a certain angle, creating a fan shape. This (sub-) radial splitting towards the rim can be very pronounced (figure 4-2d) or may be practically absent (figure 4-2a). In cross-polarized light (figure 4-2b, f, g) sweeping extinction is prevalent indicating an inhomogeneous orientation of the crystallographic axes.

This type of fabric is often accompanied by changes to darker colours (figure 4-2a, b, d, e, g, h). The character of these changes goes from nuanced and gradual to intense and abrupt. Depending on the cutting angle of the petrographic section, triangular patterns are emerging that appear to be oriented perpendicular to the crystallographic c-axis (figure 4-2e). When looking at the samples in epifluorecent light, fluorescence is congruent with colour patterns in transmitted light (figure 4-2c).

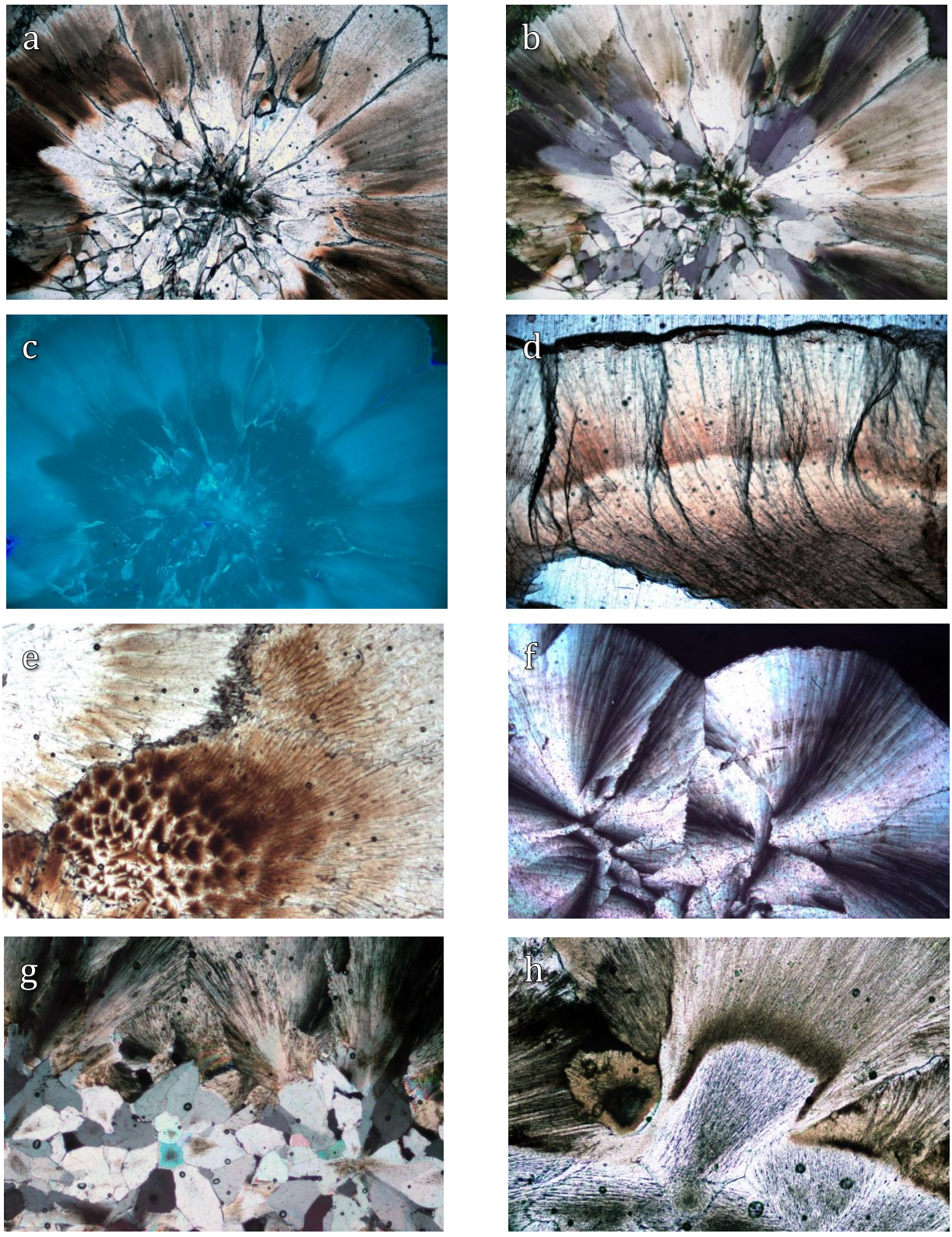

Figure 4-2: a) - c) DIV36 in transmitted (a), cross polarized (b) and epifluorecent light. Image width = 10 mm **d)** DIV33 in transmitted light. Image width = 5 mm **e)** ROS1 in transmitted light. Image width = 5 mm **f)** USV02 in cross polarized light. Image width = 10 mm **g)** DIV04 in cross polarized light. Image width = 5 mm **h)** DIV03 in transmitted light. Image width = 2.5 mm

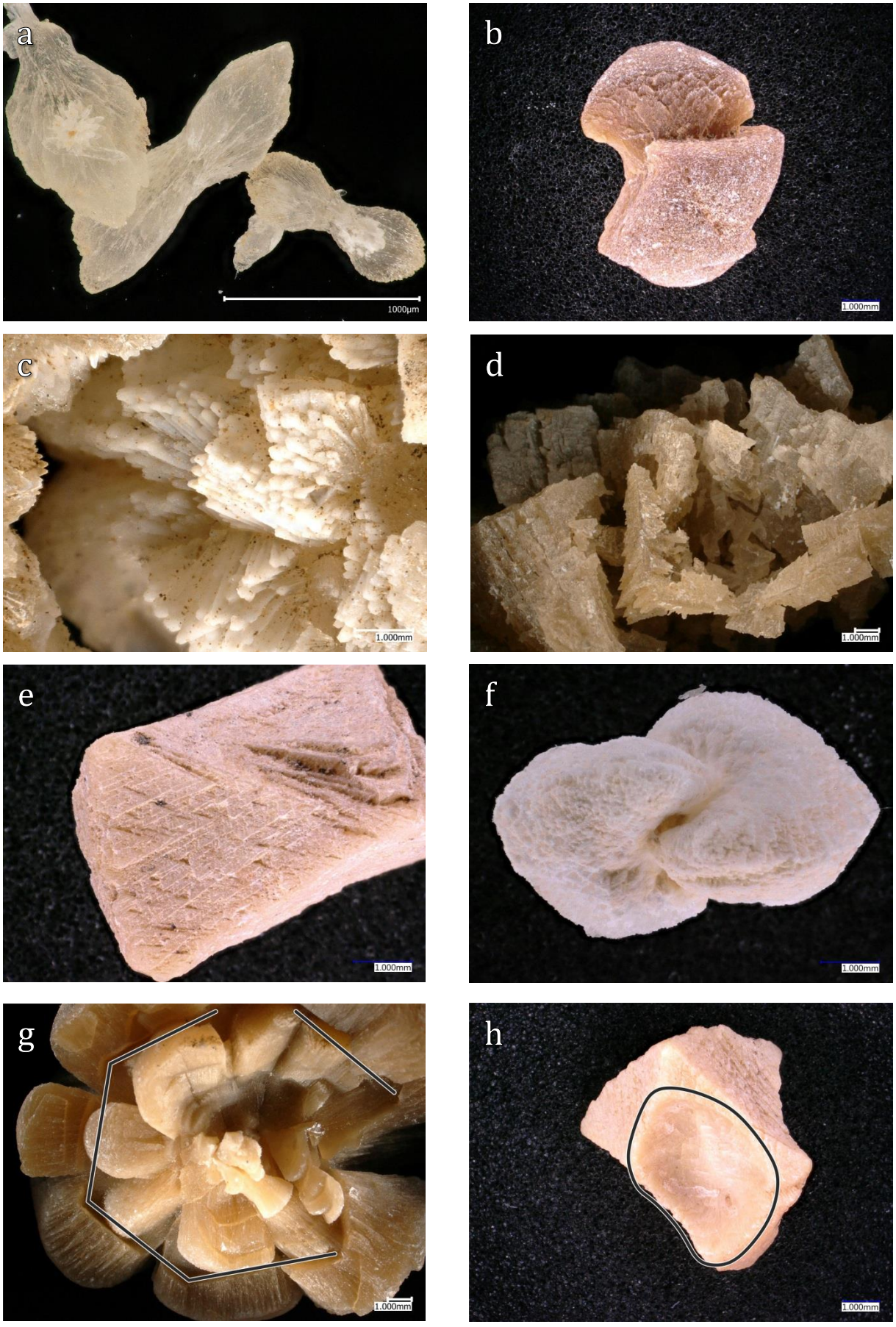

Figure 4-3: a) VIC06 **b)** TET01d **c)** DIV15 **d)** DIV10 **e)** TET01a **f)** ROSba **g)** DIV08 **h)** TET01c

Some samples show distinctly different fabrics. In figure 4-2g for example, the outer part is composed of a radially split fabric that has been described in the paragraphs beforehand. The inner part however consists of much larger crystal individuals with subhedral to euhedral morphology and uniform extinction in cross-polarized light. This extinction type indicates uniform crystallographic orientation. The interface between the inner and outer fabric domain is sharp and well defined. Figure 4-2b shows an example where a gradual transition from uniform extinction to sweeping extinction coinciding with a change in colour is observed. The central part of the uniformly extincting areas often displays characteristic streaking that manifests itself as a brownish hue covering the centre of a crystal (figure 4-2a-c, g, h).

In summary, there are two distinct types of fabrics that are hereafter referred to as *split* and *blocky*. However, numerous transitions between both types can be observed. It is therefore helpful to think of these types as end members of a spectrum.

4.1.2.2 Microphotography

Samples were also studied and documented using high resolution imaging on whole samples or fragments. Similar to observations outlined in section 4.1.2.1, two basic types of micro-morphological patterns can be described, that are found in all studied CCC_{coarse}.

Figure 4-3a, b, c and f show specimens comprising elongated, needle shaped crystallites that are oriented radially with respect to a common origin. They are arranged in bunches of several individuals with sharp and well defined long edges. These bunches terminate in an irregular and spiky fashion. The crystallite bunches can also show considerable internal deflection angles that are also not always constant throughout the sample (figure 4-3b).

Samples that show blocky fabric in cross-polarized light also show distinctive macro-morphology (figure 4-3d, e, h). Skeletal structures of aligned crystals are frequently found (figure 4-3d, figure 4-4). Where larger crystal faces have developed, it is common to see stepped surfaces sensu Frisia et al. (2000) (figure 4-3e). Specimens commonly develop a macroscopic morphology resembling a four-sided pyramid (figure 4-5).

Figure 4-4: Transition zone between multiple morphologies in sample DIV33.

Some specimens also show characteristic notches and recesses. Figure 4-3g shows an almost perfectly hexagonal edge rimming the sample and cutting through crystallites. Similar features repeat all over the depicted side of the sample but do not

occur on other sides but can also be found on many samples showing this type of fabric and colour. In other cases, a concave recess with a very smooth surface is observed (figure 4-3h). The crystallographic orientation of the specimens seems to be unaffected by these cavities. There are also samples with flat surfaces where crystal growth appears to have been mechanically restricted, whereas the opposing side shows uninhibited growth. Such samples give the impression of having grown on a solid surface. The origins of these *moulds* are unknown and they will be addressed in a purely geometrical sense hereafter.

Figure 4-5: Pyramidal shape with stepped surfaces. This morphology is exclusively associated with blocky texture in transmitted light.

4.1.3 Proposal of a new Classification Scheme

Classifying the samples using the descriptive terminology used in previous contributions (e.g. Hill and Forti, 1986; Richter et al., 2008; Žák et al., 2008; Chaykovskiy et al., 2014; Žák et al., 2018) was only partly successful for two main reasons:

Firstly, there is no common terminology that has been agreed upon. Many terms are used by multiple authors but with inconsistent meaning. Popular terms that are being used inconsistently for example are “rhombohedral”, “spherical”, “spherulite”, “skeletal”, “dumbbell-shaped” or “aggregate” amongst others.

Secondly, many of the observed samples simply do not fit any category unambiguously, mostly because they show characteristics of two or more categories. For example, there are many cases where a transition between “skeletal” and “spherical” morphologies can be described (figure 4-4). Authors previously overcame these issues by creating new categories.

Hereafter, a new classification scheme for CCC_{coarse} is proposed (figure 4-6). The aim is to reduce the number of descriptive terms to a minimum while appreciating morphological transitional forms. This is achieved by applying ideas of Grigor'ev (as presented in Self and Hill, 2003) and Sunagawa (2005) to micro- and macroscopic observations.

The horizontal axis of the diagram depicts a spectrum of morphologies associated with varying propensity to crystal splitting during growth. Classification is based on calcite fabric from blocky to (partially) split to spherulitic (i.e. fully split). Diagnostic features can sometimes be identified without petrographic sections by simply identifying the degree of splitting of crystallites along the growth axis of a specimen.

Blocky calcite is associated with low or practically absent crystal splitting. Diagnostic features are

- compact crystallite shape,
- stepped surfaces and
- uniform extinction.

Blocky fabrics can be associated with relatively low propensity to splitting at low driving force. As mentioned previously, factors such as the concentration of foreign cations or impurities can also facilitate crystal splitting, however, driving force is the dominant factor in most cases (Shtukenberg et al., 2012).

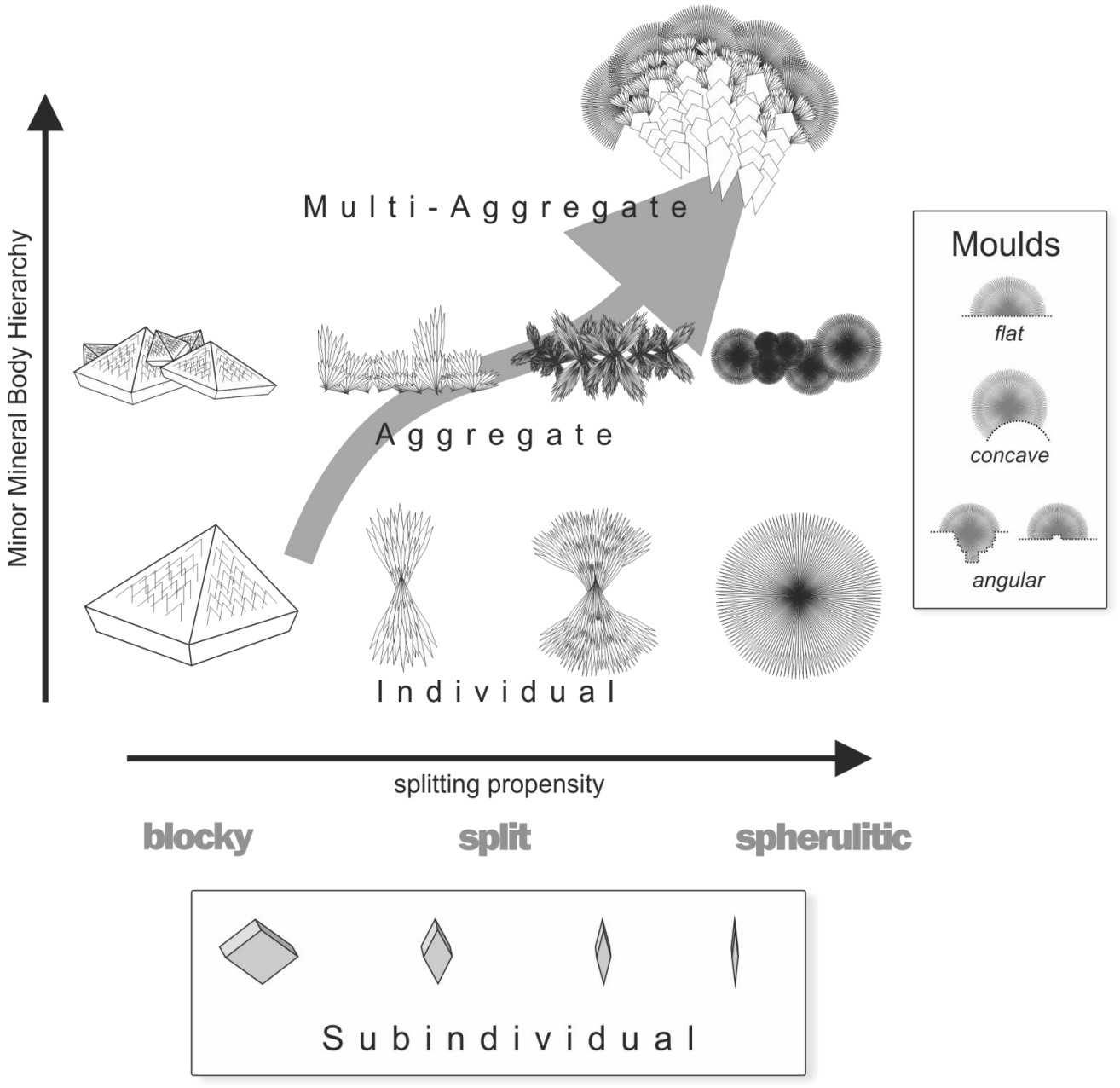

Figure 4-6: A scheme for classifying CCCs based on morphology. The horizontal axis delineates propensity of splitting of crystallites during growth. The vertical axis discriminates different hierarchical levels of minor mineral bodies sensu Self and Hill, 2003. For an exhaustive description of the concept, please refer to the main text.

In contrast to blocky fabrics, **split** fabrics are characterised by

- highly elongated crystallites
- (sub-) radial arrangement and
- sweeping extinction.

Split fabrics consequently form at relatively high driving forces or in solutions with significant enrichment in foreign cations, impurities or ligands (Shtukenberg et al., 2012).

Progressive crystal splitting will eventually lead to the formation of **spherulitic** CCC_{coarse} as the end member of the morphological spectrum. The diagnostic features are essentially the same as for split crystals. However, spherulitic CCC_{coarse} show extremely split fabrics so that individual crystallites are almost impossible to identify, even at high magnification. Yet, because of the (semi-) spherical macroscopic shape, identification is trivial.

The vertical axis of the diagram shows a hierarchy of minor mineral bodies (MMBs) sensu Grigor'ev (1961). Each level can be understood as a fundamental building block for higher levels. The lowest hierarchical level is the **subindividual**. In the context of this contribution, this term is synonymous with "crystallite". A subindividual is a MMB that shows homogenous geometric properties (e.g. blocky or acicular). However, a subindividual never exists by itself. It is always connected with at least one other subindividual to form a hierarchically higher MMB-individual. In the proposed scheme, the shape of sub-individuals is used to identify fabrics and consequently a sample's position on the horizontal axis.

Individuals comprise of several geometrically similar subindividuals. They are morphologically homogeneous, meaning they do not show any pronounced transitions between fabrics. It should be noted at this point that individuals without any morphological transitions whatsoever are hardly ever observed. Even perfectly rounded spherulitic individuals usually show some blocky micro-domains at the centre. However, these micro-domains only represent a tiny part of the entire sample. It is therefore reasonable to consider such samples homogeneous for the sake of classification.

Aggregates form by intergrowth of multiple individuals. As depicted, these aggregates don't show transitions in terms of calcite fabric. In other words, aggregates only occupy a small space along the horizontal axis. However, the size of each individual in the aggregate may vary significantly. The individuals comprising an aggregate are not arranged according to crystallographic twinning laws and are rather oriented randomly or sometimes follow non-crystallographic patterns (e.g. radial arrangements like in figure 4.3g).

The highest hierarchical level is dedicated to so-called **multi-aggregates**. This term is used for all specimens that show prominent transitions from one fabric to another and therefore occupy a larger fraction along the horizontal axis. Multi-aggregates have evolved along a path from lower hierarchical levels to higher ones by crossing over a range of driving forces during crystallization. In an extreme case, a blocky individual would start to split up into multiple split individuals. These split individuals form a split

aggregate around the blocky individual, while the driving force keeps increasing. The end results will be called a '*multi-aggregate from blocky to spherulitic*'.

Additionally, every specimen can be modified by physical inhibition of growth in one or more directions. In the proposed scheme, these modified morphologies can be geometrically described by flat, concave or angular **moulds**. Moulds can be observed with samples at all levels of hierarchy and are not causally connected to mineral fabrics. It is unknown how moulds form, but reasonable suggestions include growth obstruction by ice, gas bubbles or rock fragments (Žák et al., 2018).

4.2 Analytical Results

4.2.1 Sample Description

The following chapter is concerned with an in-depth chemical and crystallographic characterisation on a subset of 15 samples from the caves Div'ya (DIV), Rossiyskaya (ROS), Usvinskaya (USV), Viasherskaya (VIA) and Victoria (VIC). Primarily, large specimens were selected to have enough material available and many different methods could be applied to each of the samples. The samples covered in the upcoming chapter are depicted in figure 4-9. Sample classification based on the scheme, that has been proposed beforehand, is visualized in figure 4-8. Table 4-1 gives an overview of which analyses have been performed on which samples.

- DIV01 is large specimen, about 5x2 cm in size that classifies as a spherulitic aggregate. It consists of brownish-grey material and shows a relatively compact shape.
- DIV02 is a multi-aggregate from split to spherulitic. Twinning can be observed on some individuals. The split inner part is slightly translucent while the outer spherulitic part is milk-coloured.
- DIV03 is a multi-aggregate from split to spherulitic that has a crust-like appearance where the bottom side of the sample appears inhibited from growing freely.
- DIV04 is a multi-aggregate from blocky to split. However, the blocky component is not visible from the outside and only covers the innermost part of the sample.
- DIV05 is a multi-aggregate from blocky to split with a slightly translucent orange to ochre colour. A whitish layer covering some of the outer parts of the sample might indicate the start of a transition towards the spherulitic domain.
- DIV10 is a blocky aggregate with ubiquitous subhedral faces that show heavily stepped surfaces.
- DIV33 is an example of a multi-aggregate from blocky to spherulitic, consisting of brownish material.
- With a diameter of almost 7 cm, DIV38 is the largest specimen in the collection. It classifies as a multi-aggregate from blocky to spherulitic. In its vicinity, many smaller specimens of similar morphology were found.

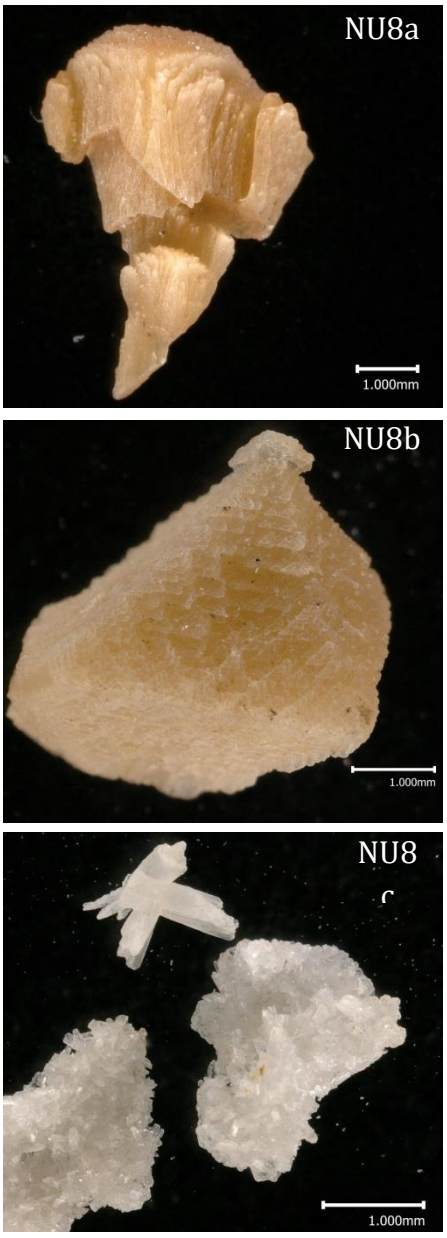

Figure 4-7: Close-up of three morphological varieties from sample NU8 that were selected for detailed analyses. **a)** split individual, **b)** blocky individual, **c)** split aggregates

- Sample NU8 is fundamentally different from the other samples taken from Div'ya cave. It comprises many (sub-) millimetre sized crystals covering an entire morphological spectrum from blocky to spherulitic on both the individual and aggregate level. Three morphological categories were picked out to perform more detailed analyses on (figure 4-7).
    - split to spherulitic individuals
    - blocky individuals and aggregates
    - split aggregates
- ROS01 is a multi-aggregate from split to spherulitic which exceptionally dark colour. A layer of whitish coating covers large parts of the sample.

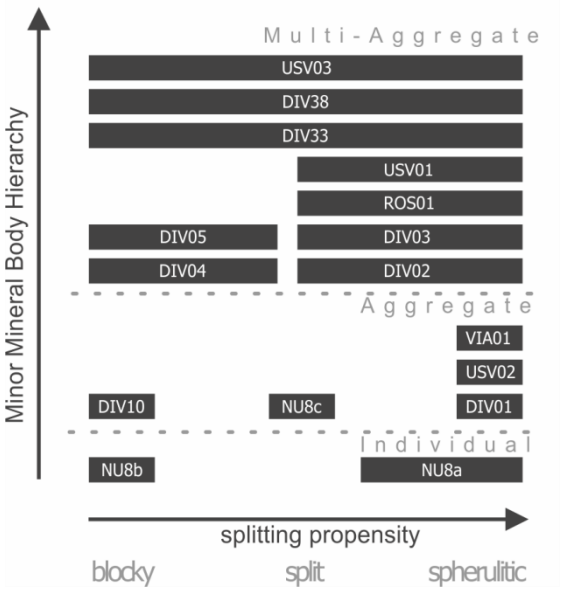

Figure 4-8: Classification of samples according to the proposed scheme. The width of bars corresponds to the approximate range of driving force covered by one sample based on visual observation.

- USV01 is another example of a large multi-aggregate covering a wide range from split to spherulitic.
- USV02 is a very dark spherulitic aggregate. There are two morphologically identical specimens in this sample.
- USV03 is again a multi-aggregate from blocky to spherulitic.
- VIA01 is a purely spherulitic aggregate.
- VIC05_glen is an unusual specimen from Victoria cave. It consists of multiple very fragile specimens made up of whitish powdery material that is agglomerated into glendonite morphology. Glendonites are pseudomorphs of calcite after ikaite ($CaCO_3 * 6H_2O$), a mineral that is unstable at room temperature. The sample was found alongside whitish-translucent split individuals and aggregates. The depicted specimen is the largest one that was found. Most others have fractured at some point in time and are now only partially preserved.

Table 4-1: Overview of analyses per sample.

Sample ID	*stable isotope transect*	*stable isotope spot measurement*	*fluid inclusion analysis*	*U/Th dating*	*thin section petrography*	*PXRD*	*TEM*	*LA-ICP*
DIV01	x		x		x	x	x	
DIV02		x	x		x			
DIV03		x	x		x			
DIV04	x		x		x	x		
DIV05	x		x		x			x
DIV10					x			
DIV33					x			
DIV38	x	x	x	x	x			
NU8		x	x	x		x		
ROS01	x		x		x			x
USV01			x	x				
USV02	x		x	x	x			
USV03			x	x				
VIA01	x		x		x			
VIC05_glen				x		x		

Figure 4-9: Photographic documentation of the samples presented in the analytical results chapter.

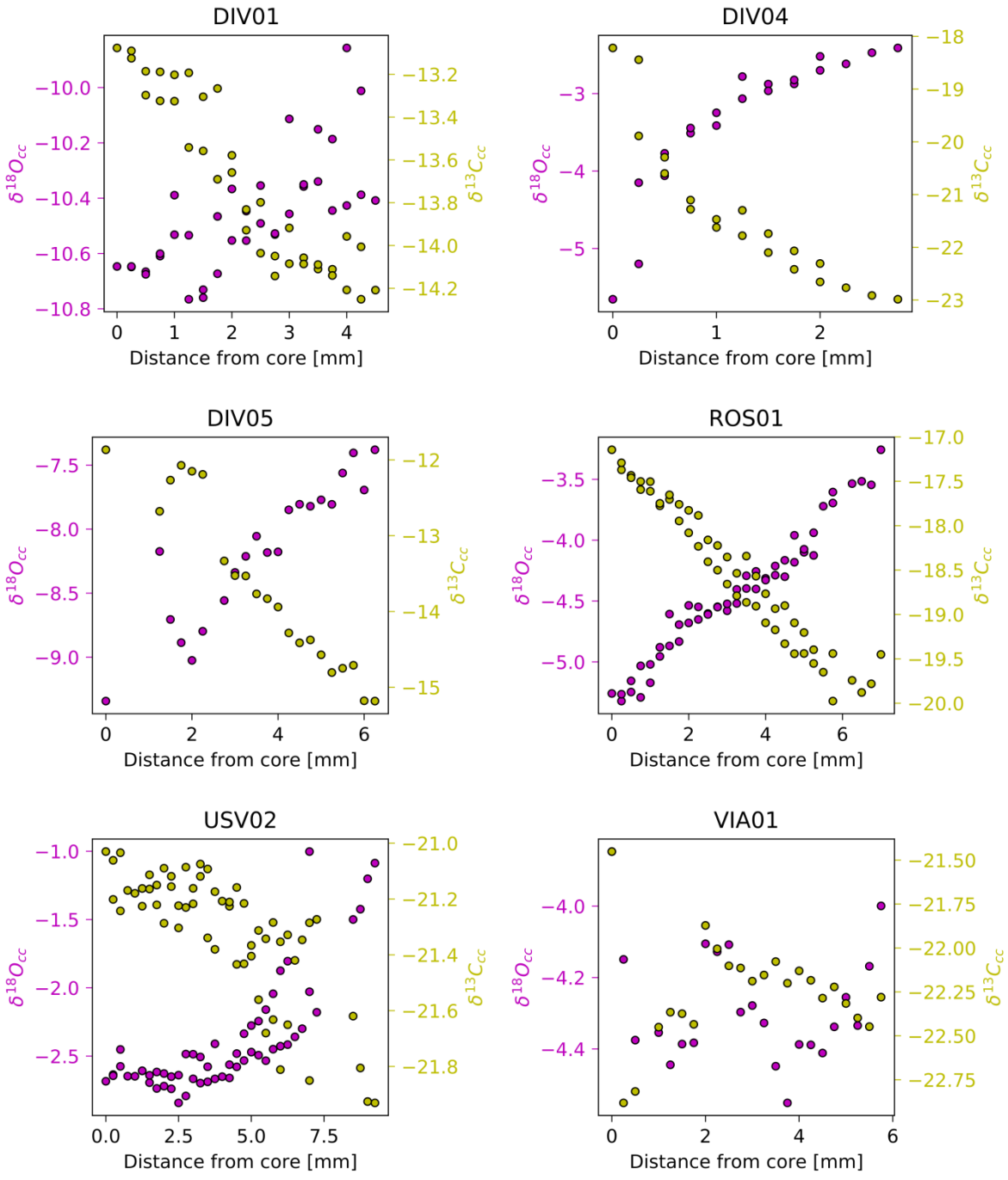

Figure 4-10: $\delta^{18}O_{cc}$ and $\delta^{13}C_{cc}$ values from high resolution profiles across 6 large CCC specimens. The x-axis of the plots corresponds to the distance of the measurement with respect to the core of the sample (i.e. nucleation point of growth). Apart from sample VIA01, all samples show a distinct anti-correlation between carbon and oxygen isotopic composition. Stable isotope values are reported in ‰ on the VPDB scale.

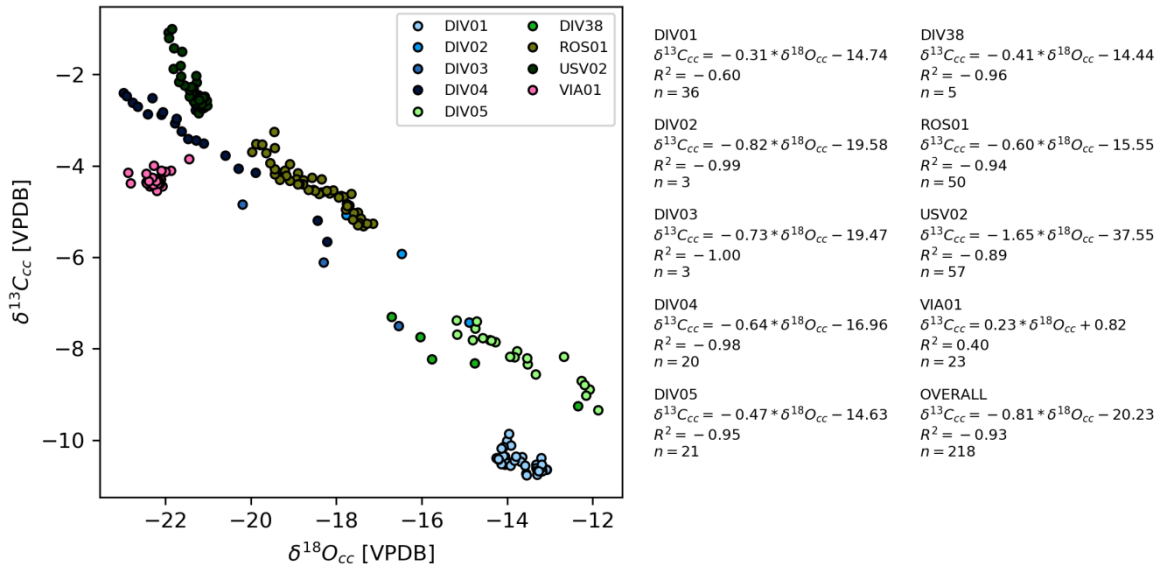

Figure 4-11: Results of $\delta^{18}O_{cc}$ and $\delta^{13}C_{cc}$ of high resolutions profiles and spot profiles of selected specimens. On the right-hand side are the corresponding linear regressions of each sample, as well as the overall linear regression, encompassing the entire data set. Stable isotope values are reported in ‰ on the VPDB scale.

4.2.2 Carbonate isotopes

Analyses on stable isotopes of C and O in CCC were performed with different strategies:

- High resolution (step 250µm) transects were produced for samples DIV01, DIV04, DIV05, DIV38, ROS01, USV02 and VIA01. Spot measurements of characteristic zones were taken from samples where complex geometry didn't allow for a continuous transect to be drilled.
- Sample NU8 was grouped into morphological varieties and subsequently analysed to compare crystal morphology with isotopic composition. These analyses were performed on two grain size fractions of the sample.
- Spot measurements to check if a sample follows the general isotopic trends that have been described in previous studies (Žák et al., 2018).

Results for and $\delta^{18}O_{cc}$ used for thermometric calculations are presented in section 4.2.3. All carbonate δ-values are reported with respect to the VPDB standard.

4.2.2.1 Stable Isotope Profiles

Plots of all high resolution profiles versus distance are shown in figure 4-10. Except from VIA01, all samples show a clear trend from low to high values with respect to $\delta^{18}O_{cc}$ and from high to low values with respect to $\delta^{13}C_{cc}$ from core to rim. The character of these trends appears exponential for DIV04 and USV02. In all other samples, the trends are linear.

Results of high resolution and spot transects in $\delta^{18}O$ – $\delta^{13}C$ space are depicted in figure 4-11. The samples generally show a strong depletion in $\delta^{18}O_{cc}$ between -22.9‰ and -11.9‰. $\delta^{13}C_{cc}$ values are less depleted ranging from -10.8‰ to -1.0‰.

There is no morphological clustering in this data set, meaning that samples plotting next to each other do not necessarily share morphological features. All samples follow an overall trend ($\delta^{13}C_{cc} = -0.8 * \delta^{18}O_{cc} - 20.2$), however, there is a significant difference in the trends derived from each sample individually.

The spherulitic aggregates (VIA01, USV02 and DIV01) show a comparably narrow range of $\delta^{18}O_{cc}$ values, typically within 1.5‰. The correlation between $\delta^{18}O_{cc}$ and $\delta^{13}C_{cc}$ in VIA01 and DIV01 is weaker. In the case of USV02 the correlation is strong but the regression has a much steeper slope. Samples classified as multi-aggregates are spread out over a much larger range of $\delta^{18}O_{cc}$ values of at least 2.8‰ up to 4.8‰ in the case of DIV04. A similar relationship, where the three spherulitic aggregate are the most tightly clustered ones, can be observed with $\delta^{13}C_{cc}$ values, albeit being less distinctive.

4.2.2.2 NU8

Sample NU8 is an accumulation of many (sub-) millimetre sized crystals showing vast variety morphological features. After separating different grain size fractions 49 specimens were picked out for stable isotope analysis, 27 from grain size fraction 2-4 mm and 22 from fraction >4 mm. There were at least two analyses performed per specimen, i.e. 124 measurements all together (figure 4-12). A complete list of samples including pictures was added to the appendix.

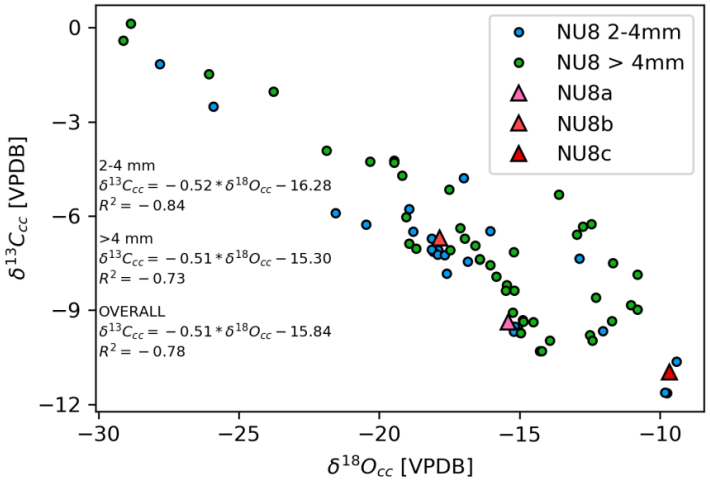

Figure 4-12: Results of $\delta^{18}O_{cc}$ and $\delta^{13}C_{cc}$ for sample NU8. Blue dots represent mean values of three repeated measurements per grain of size fraction 2-4mm. Green dots correspond to individual measurements performed on grains of size fraction > 4mm. Triangles indicate the isotopic composition of selected morphological varieties: NU8a – split individual, NU8b – blocky individual, NU8c – split aggregate. Stable isotope values are reported in ‰ on the VPDB scale.

Sample NU8 spans a notably wider range of δ values than the results reported in figure 4-11 for other CCC_{coarse} samples. $\delta^{18}O_{cc}$ for some NU8 specimens even goes as low as -29.1‰. The values are not distributed equally and concentrate around $\delta^{18}O_{cc}$ = -16‰ and $\delta^{13}C_{cc}$ = -8‰. Grains >4 mm in size partly show considerable internal variability from core to rim. Both grain size fractions show very similar linear regression trends asides from a slightly shifted intercept.

The selected morphologies NU8a, b and c, (triangles in figure 4-12) plot where the undifferentiated data set forms clusters. NU8c, which consists of split aggregates, is situated at the lower right-hand side of the plot with an isotopic composition of $\delta^{13}C_{cc}$ = -11.0‰ and $\delta^{18}O_{cc}$ = -9.7‰. NU8b, a collection of blocky individuals, lies roughly in the centre of the undifferentiated data set at $\delta^{13}C_{cc}$ = -6.7 and $\delta^{18}O_{cc}$ = -17.8‰. NU8a, comprising spherulitic and split individuals plots in between the two at $\delta^{13}C_{cc}$ = -9.4‰ and $\delta^{18}O_{cc}$ = -15.4‰.

Table 4-2: Summary of fluid inclusion measurements. Crossed out rows correspond to measurements where the water amount was either too high or too low to be reliable (i.e. <0.1 µl or >0.9 µl). Stable isotope values from these measurements were excluded from further calculations. The analytical error of these data is ±2.3‰ for $\delta^{2}H_{water}$ and ±1.1‰ for $\delta^{18}O_{water}$. The $\delta^{18}O$ offset quantifies the displacement of $\delta^{18}O$ from the corresponding value on the GMWL for a given $\delta^{2}H$.

Sample	Aliquot	Water Amount [µl]	Water Content [µl g-1]	$\delta^{2}H_{water}$ [‰VSMOW]	$\delta^{18}O_{water}$ [‰VSMOW]	δ18Owater Offset	δ18Occ [‰VPDB]	Notes
DIV01	b	0.14	0.15	-101.3	-10.5	3.4	-14.1	
DIV01	d	0.23	1.06	-106.4	-13.1	1.5	-14.1	
DIV02	b	0.14	0.07	-133.5	-18.4	-0.5	-17.2	
DIV03	a	0.31	0.48	-102.4	-16.6	-2.5	-22.5	
DIV04	a	0.32	0.25	-128.7	-14.1	3.3	-22.1	
DIV04	b	0.17	0.16	-123.0	-14.6	2.0	-21.6	
DIV38	ia	0.57	0.50	-128.2	-17.1	0.2	-15.9	Inner part
DIV38	ob	0.11	0.07	-129.4	-18.0	-0.6	-16.0	Outer part
DIV38	oc	0.11	0.08	-129.4	-18.0	-0.6	-16.0	Outer part
NU8a	a	0.44	0.89	-119.8	-18.0	-1.7	-15.4	Morphology A
NU8b	b	0.25	0.50	-140.5	-23.3	-4.5	-17.8	Morphology B
ROS01	a	0.12	0.12	-146.3	-20.4	-0.9	-18.8	
USV01	a	0.15	0.13	-139.6	-19.2	-0.5	-21.1	
USV01	b	0.21	0.10	-147.1	-23.9	-4.2	-21.1	
USV02	a	0.28	0.20	-139.0	-16.8	1.8	-22.3	
USV02	b	0.37	0.29	-138.0	-20.4	-1.9	-22.0	
USV02	c	0.34	0.24	-114.8	-16.9	-1.3	-21.8	
USV03	a	0.14	0.12	-131.9	-19.9	-2.2	-17.2	
VIA01	a	0.12	0.16	-140.7	-20.4	-1.5	-22.9	
VIA01	b	0.24	0.18	-142.6	-34.0	-15.0	-22.4	

4.2.3 Fluid inclusion analysis

Analyses to determine the H and O stable isotopic composition of water entrapped in aqueous inclusions of CCC_{coarse} were performed on 12 samples. The samples were selected using the following criteria: i) The samples had to be large enough to allow for the fluid inclusion measurement but also suitable for the manufacturing of petrographic thick sections, which is a standard procedure for this kind of analysis. ii) Samples should cover a variety of macroscopically different morphologies. iii) To make results more comparable, only samples from four different caves were examined (Div'ya: DIV01, DIV02, DIV03, DIV04, DIV05, DIV38, NU8; Usvinskaya: USV01, USV02, USV03, Viasherskaya: VIA01; Rossiyskaya: ROS01).

Whenever possible, larger specimens were broken into multiple aliquots to get up to four measurements per sample. In the case of NU8, some 20 specimens from three different morphological varieties were hand-picked from the main sample. Sample DIV38 was large enough to be separated along the growth axis into an inner and outer part. All together 30 individual measurements were performed, whereas only 20 yielded suitable water amounts (table 4-2).

4.2.3.1 Petrography of Fluid inclusions

As a part of fluid inclusion analysis, it is useful to characterise the fluid inclusions before measurements. This is to provide additional constrains for the interpretation and determine the spatial distribution of fluid within the sample.

For the analysed CCC_{coarse}, two key observations can be reported in this context.

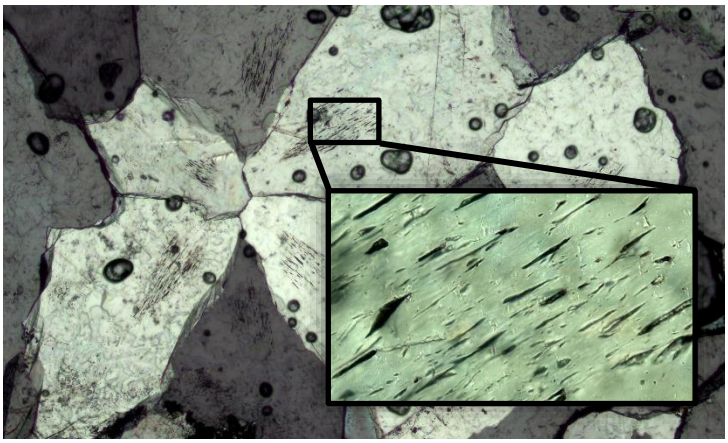

Figure 4-13: Elongated fluid inclusions occupying the central region of crystals (DIV05). Image width 5 mm, Insert width = 500µm

i) Fluid inclusions are commonly found in the central parts of the sample, associated with blocky texture (figure 4-13). The inclusions are clearly intra-crystalline, making them less prone to potential alteration processes such as leakage or refilling. They are elongated and oriented parallel to the growth direction of the crystal.
ii) Figure 4-14 shows dendritic features that are commonly observed in split fabrics with dark brown colour. These extremely elongated cavities have a dendritic appearance with numerous little spikes protruding perpendicularly to the long axis, which is again oriented parallel to the growth direction of the crystallites. Because of the extremely small size, it remains unclear whether these features are cavities that potentially contain water.

Both features have been observed in multiple specimens. It is important to stress that each of the two features is exclusively associated with the corresponding calcite fabric (i.e. blocky or split). Since the fabrics are thought of as endmembers of a spectrum, the associated fluid inclusion data can be interpreted in the same way, assuming both types hold water. Because blocky fabrics always form before the split fabrics, the respective type 1 fluid inclusion – if present - are representative of the early stages of the precipitation process. Conversely, type 2 fluid inclusion capture later stages, when the fluid has evolved further. A sample containing both types would therefore represent a mixture of both types of fluid and must be interpreted accordingly. Similarly, samples that are morphologically homogenous should yield more reproducible results than samples comprising multiple fabrics.

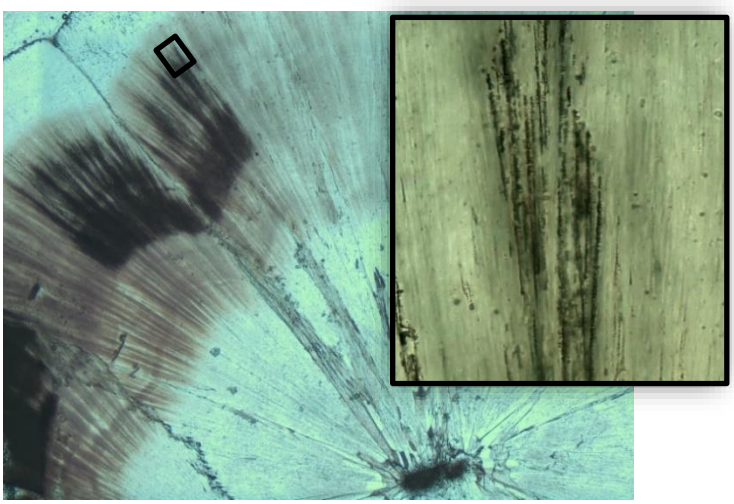

Figure 4-14: Potential water bearing features with dendritic appearance from sample DIV36. Insert width 200 µm.

Without additional information to clarify the actual water content of each fabric it is not possible to assess the effects that a mixture of two or more fluid types will have on the measurements of $\delta^{18}O_{water}$ and $\delta^{2}H_{water}$. However, it is still important to keep these observations in mind when evaluating the results.

4.2.3.2 Water content

The samples yielded highly variable water amounts resulting in a range of water contents between 0.04 and 1.06 µl g^{-1}, whereas the median content of all measurements is 0.16 µl g^{-1}. Figure 4-15 shows the averaged water contents per sample. The results were generally reproducible apart from DIV01 and DIV38, which show strong internal variability. In the case of DIV01 all but the first aliquot were only crushed partially because of the relatively high water content of this sample, thus underestimating the water content of the sample. For DIV38 the variability seems reflect the variable water content. Overall, there is no clear correlation between water content and morphology.

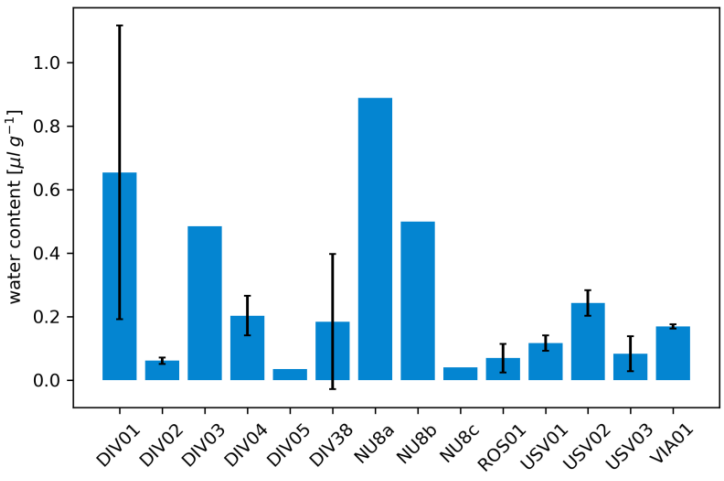

Figure 4-15: Mean water content of CCC_{coarse} samples. Error bars indicate the 1σ standard deviation of all aliquot measurements.

4.2.3.3 *Stable isotopes of fluid inclusion water*

Measurements of stable isotopes of water in fluid inclusions gave values between -147.1 ‰ and -101.3‰ for δ^2H_{water} and -20.4‰ and -9.8‰ for $\delta^{18}O_{water}$ (table 4-2, figure 4-16; water isotopes are reported with respect to the VSMOW standard). Measurements with improper water amounts were removed from the data set. Similar to the results on water content, some samples show strong internal variation while others yielded reproducible results. The internal standard deviations range from ±0.4‰ (DIV04) to ±7.0‰ (VIA01) for $\delta^{18}O_{water}$ and from ±0.7‰ (DIV38) to ±13.7‰ (USV02) for δ^2H_{water}.

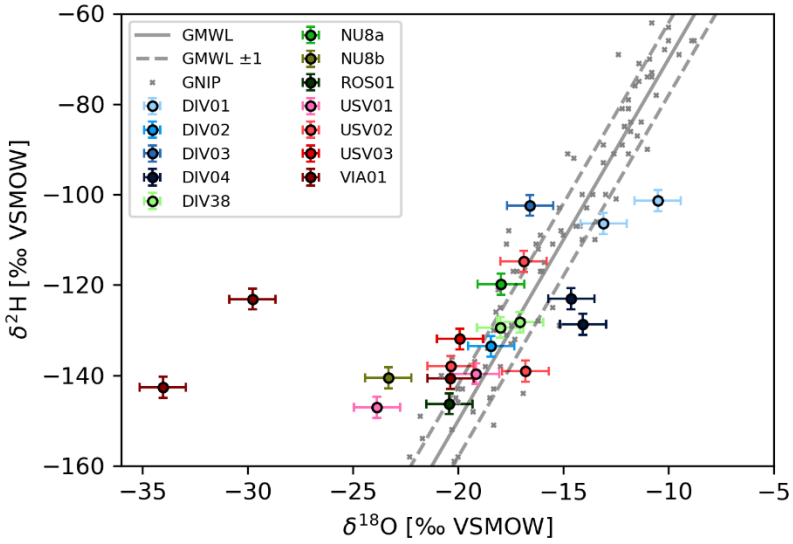

Figure 4-16: Results of stable isotope measurements of δ^2H and $\delta^{18}O$ in fluid inclusions. Additionally, the stable isotope composition of modern precipitation taken from global network for isotopes in precipitation (GNIP) stations in Perm (58.009°N 56.180°E) and Pechora (65.117°N 57.010°E) are plotted alongside the data. Precipitation data for stations Perm and Pechora downloaded from GNIP database accessed via https://nucleus.iaea.org/wiser.

In general, δ^2H values derived by this method are considered more reliable because i) they are not affected by potential errors introduced by overlapping with a pre-CO peak as described in section 3.3.5 and ii) $\delta^{18}O$ values may be subject to diagenetic alteration induced by recrystallization (Demény et al., 2016a). Table 4-2 lists the offset in $\delta^{18}O_{water}$ relative to the value on the GMWL, corresponding to the measured δ^2H_{water}. Only 13 out of 21 data points plot within a field ±1‰ $\delta^{18}O_{water}$ of the global meteoric water line (GMWL: $\delta^2H = 8^* \delta^{18}O + 10$) considering analytical error. The remaining samples plot outside of the GMWL ±1‰ $\delta^{18}O_{water}$-band. Sample DIV38 gave the most consistent results with a mean deviation of only 0.5‰ $\delta^{18}O_{water}$ from the GMWL.

Out of all 30 analyses (including measurements with improper water yield), 27 have shown a pre-CO peak overlapping the main CO peak in the chromatogram (see section 3.3.5). Ignoring measurements with

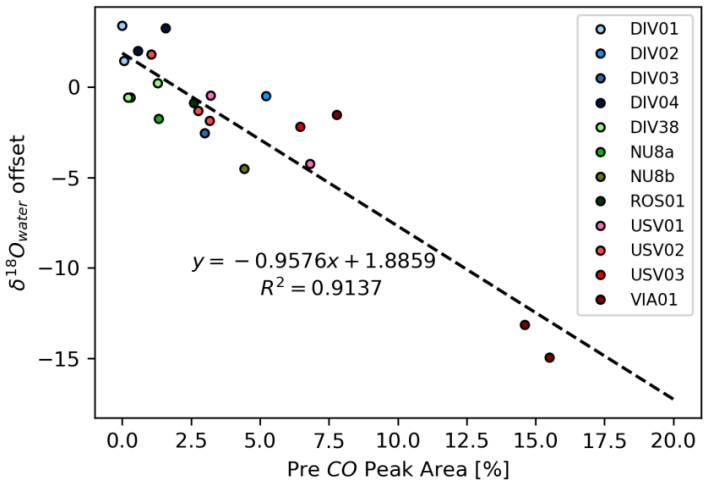

Figure 4-17: $\delta^{18}O_{water}$ offset as a function of the relative portion of the overall peak area occupied by the pre-CO peak. A clear linear correlation between the two measures was found.

improper water amounts, the area of these pre-CO peaks on average makes up 3.9% of the overall peak area, i.e. the area of the main CO peak and the pre-CO peak together. This percentage reaches up to 15.5% in extreme cases (figure 4-17). The pre-CO peak area correlates with the magnitude of $\delta^{18}O$ offset. A 1% increase in relative area occupied by the pre-CO peak will result in a $\delta^{18}O$ offset of roughly -1‰. It is noteworthy that the linear regression does not intercept at ±0‰ but at +1.9‰ $\delta^{18}O$ offset. This is caused by combining negative and positive shifts in the linear regression. Furthermore, the trend is disproportionately affected by 2 outliers of sample VIA01. This sample had very prominent pre-CO peaks that caused unusually strong overlap with the main CO peak.

There is no clear correlation between morphology and stable isotope composition of aqueous fluid inclusions.

4.2.4 Thermometry

The overall goal of fluid inclusion analysis was to use the data for thermometric calculations. In general terms, isotopic equilibrium with respect to oxygen in the carbonate system is defined by three parameters:

- $\delta^{18}O$ of the mineral forming water
- $\delta^{18}O$ of the $CaCO_3$ precipitate
- Temperature

If two of these parameters are known, the third can be calculated under the assumption of isotopic equilibrium. The literature offers a variety of models that can be used for this purpose. These models are

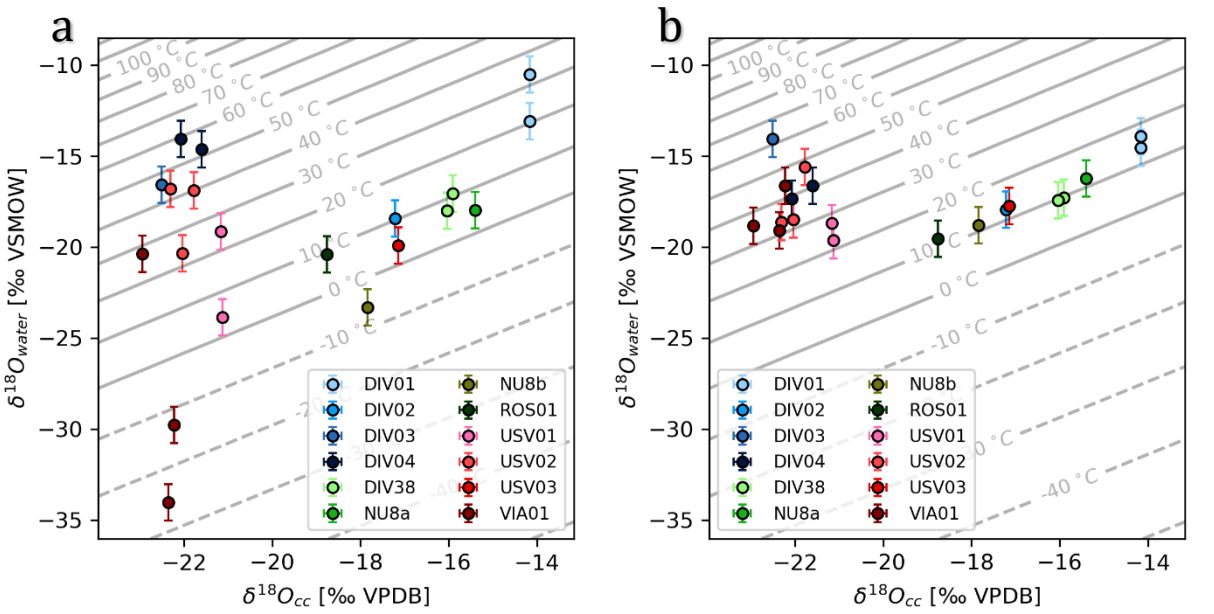

Figure 4-18: a) Results of oxygen stable isotope thermometry on CCCs using measured values of $\delta^{18}O_{cc}$ and $\delta^{18}O_{water}$. The contour lines show isotherms according to the model published by Friedman and O'Neil (1977). Temperatures below the freezing point of water are shown as dashed lines. **b)** Same as a), but instead of measured $\delta^{18}O_{water}$, values projected onto the GMWL from measured $\delta^{2}H_{water}$ are used.

usually derived from lab experiments (e.g. Friedman and O'Neil, 1977) or are calibrated using empirical data from well-studied natural sites (Craig, 1965; Dettman et al., 1999; Coplen, 2007; Tremaine et al., 2011). All models share the basic assumption of carbonate precipitation at isotopic equilibrium. They only apply to a limited range of temperatures, usually well above the freezing point of water. This means that no model is confidently defined at 0 °C.

Based on the observed offsets in $\delta^{18}O_{water}$ that have been described in section 4.2.3.3 two different values for the $\delta^{18}O_{water}$ of a sample have been used for thermometric calculations: The measured $\delta^{18}O_{water}$ as presented in table 4-2 and the $\delta^{18}O_{proj}$ value which is the $\delta^{18}O$ equivalent to the measured $\delta^{2}H_{water}$ on the GMWL ($\delta^{18}O_{proj} = (\delta^{2}H_{water} - 10) / 8$).

Figure 4-18a visualizes the results according to one of the published models (Friedman and O'Neil, 1977; $T = (2.78*10^{6} / (10^{3} \ln(\alpha) + 2.89))^{-0.5}$). A complete list of results from all cited thermometric models has been added to the appendix.

A crucial first observation is that the data points generally do not fit the 0 °C isotherm, as it would be expected for cryogenic precipitates. This holds true for all of the tested thermometric models. Only the equations by Kim and O'Neil (1997) and Dettman et al. (1999) yielded temperatures within 2 °C of freezing for samples NU8a, USV01b and USV03a.

Moreover, two clusters of data can be described in figure 4.18. 1) A cluster with relatively heavy $\delta^{18}O_{cc}$ values above -20‰ VPDB and 2) a cluster showing relatively depleted $\delta^{18}O_{cc}$ values below -20‰ VPDB. Clustering is more prominent when using projected oxygen isotope values from fluid inclusion $\delta^{2}H_{water}$ (figure 4-18b). $\delta^{18}O_{proj}$ /$\delta^{18}O_{cc}$ pairs of cluster 1) seem to be well aligned with the 10 °C isotherm while cluster 2) shows no internal trend.

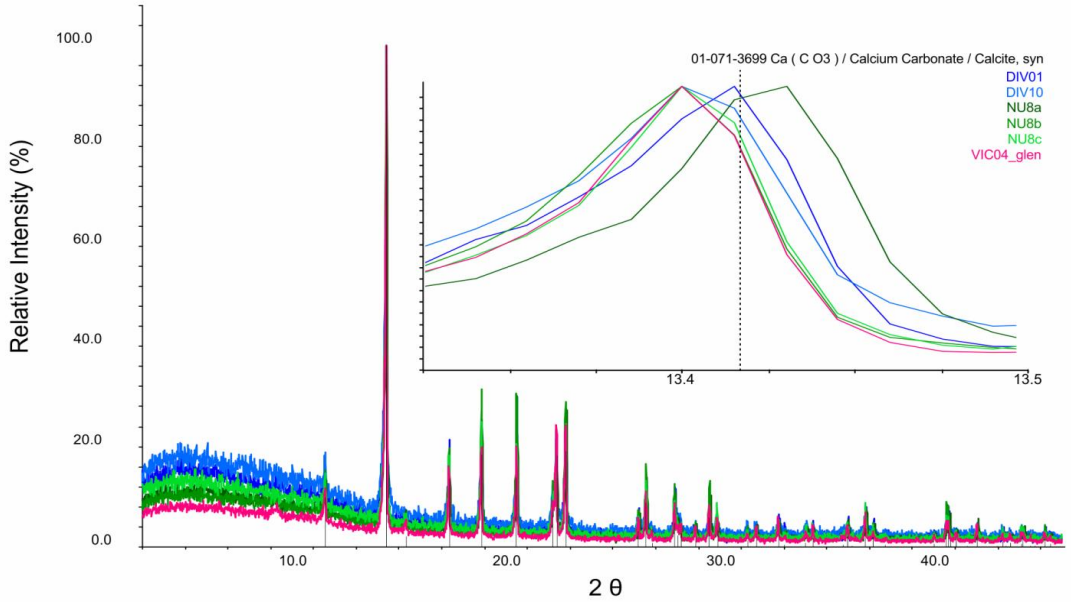

Figure 4-19: X-ray diffractograms of 7 selected CCC samples. The insert shows a close-up view of the main calcite peak at 13.42° 2θ using Mo Kα radiation ($\lambda = 70.93185*10^{-12}$m). The peaks are clearly shifted.

4.2.5 Powder X-Ray Diffraction (PXRD)

6 samples were studied using PXRD. Except for VIC05_glen (Victoria cave, Bashkortostan), all samples were taken from Div'ya cave (Northern Ural). All 6 diffractograms can be confidently matched with database entries for synthetic calcite (ICDD # 01-071-3699). There were no additional peaks observed. However, not all peaks line up exactly with the values reported in the data base but are shifted over a range of approximately 0.05° 2θ instead. Figure 4-19 shows that only DIV01 matches the synthetic calcite unequivocally. Samples NU8b, NU8c, DIV10 and VIC05_glen are shifted towards lower 2θ angles. NU8a is shifted towards higher 2θ values.

Taking morphology into consideration, the samples with the highest 2θ angles are the spherulitic specimens (DIV01, NU8a). Blocky and split morphologies (DIV10, NU8b, NU8c), as well as the glendonite sample (VIC05_glen), are consistently shifted towards a lower 2θ angle.

According to the Bragg's law, a shift in the absolute value of 2θ, while maintaining the relative position of the peaks, is generally interpreted as a change in volume of the crystallographic unit cell. A higher 2θ angle indicates a smaller volume, if all other parameters are held constant.

Considering this implication, spherulitic morphology coincides with a smaller unit cell volume in the studied samples. On the contrary, blocky or split morphology suggests a relatively large unit cell.

4.2.6 Transmission Electron Microscopy

Figure 4-20 shows bright field TEM images and selected area electron diffraction (SAED) patterns for a powdered aliquot of sample DIV01. Electron reflexes on a 500nm spot clearly show a ring pattern, indicating inhomogeneous crystallographic orientation in the analysed region of the grain. This effect may be caused by disorder associated with nano-cristallinity of the sample. The mottled texture is also indicative of sub-micrometre crystallinity. Figure 4-21 shows another grain of sample DIV01 on a smaller scale, where it was possible to obtain sharper reflexes. Strong reflexes are highlighted, that correspond to (-114) and (104) planes of the calcite lattice. These reflexes are typically interpreted as twins according

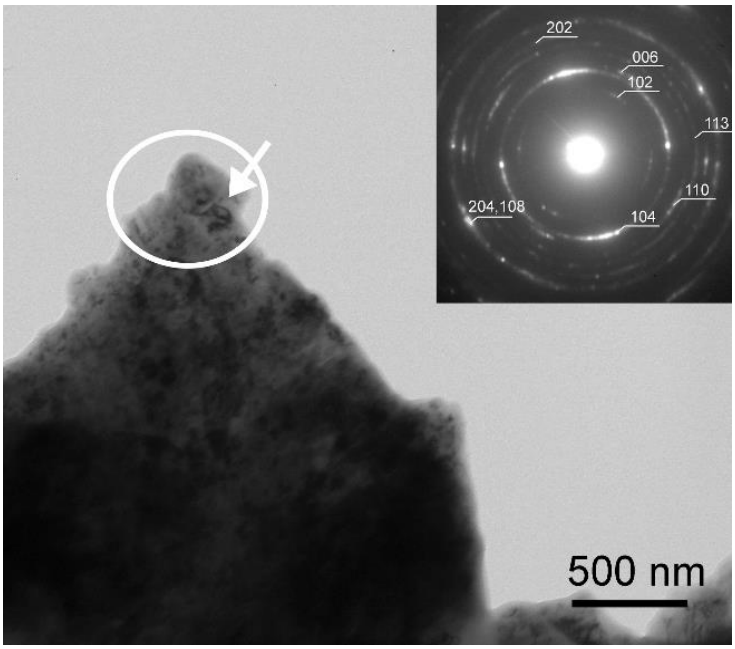

Figure 4-20: Bright field TEM image of a powder grain taken from sample DIV01. Note the mottled texture of the grain. The insert in the upper right shows the SAED pattern taken from the circled area. The electron reflexes are streaking.

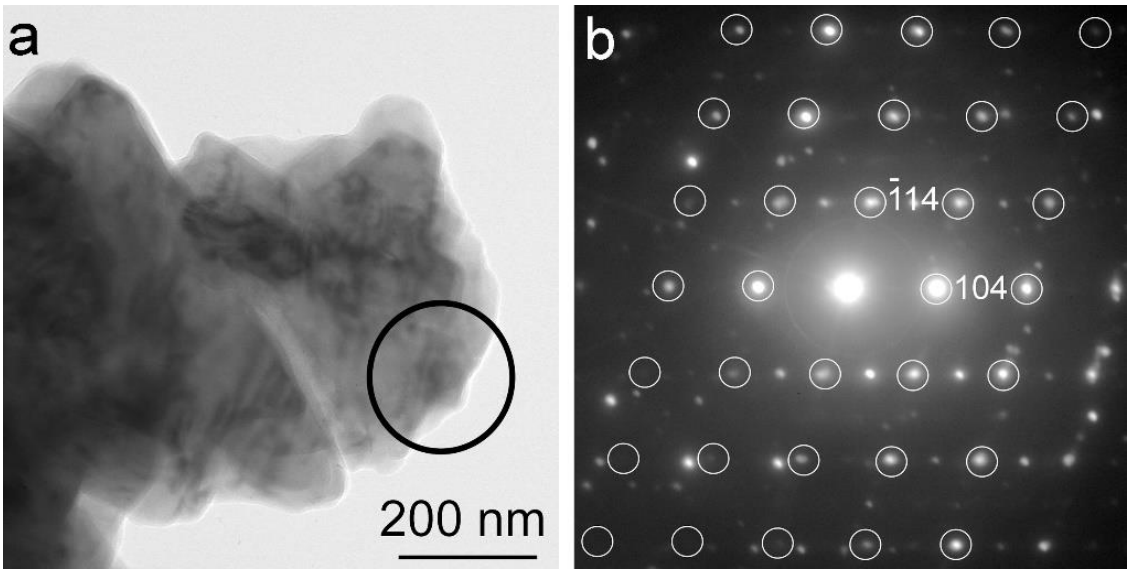

Figure 4-21: a) Bright field TEM image of a sub-micrometre sized sliver of sample DIV01. The black circle delineates the area from which the SAED pattern shown in b) was taken. **b)** SAED pattern taken from the circled area. Sharp reflexes indicate more homogenous structure as compared to figure 4-20. The indexed reflexes correspond to the (104) and (-114) lattice planes of a twinned individual according to {104} calcite twinning.

to {104} calcite twinning (Larsson and Christy, 2008). However, there are numerous reflexes that cannot be attributed to the calcite lattice unequivocally, therefore pointing towards disorder. In summary, DIV01 can be described as poorly crystalline with an average crystallite size of only 20-40 nm.

4.2.7 LA-ICP-MS

Samples DIV05 and ROS01 were also analysed with LA-ICP-MS to study their trace element composition across a full transect. Out of the 15 elements that have been measured, only Mg, P, Sr, Ba and U show significant trends. The rest is either below the detection limit or yielded very noisy data.

	DIV05	ROS01
Mg	1.30	2.29
Sr	2.22	5.51
Ba	3.26	2.31
P	94.98	1977.44
U	1.09	0.91

Table 4-3: Relative increases of trace elements from core to rim derived from LA-ICP-MS transects. The numbers quantify the relative increase as a multiplications factor:
rel.increase = (Cmax – Cmin) / Cmin

Bot samples show similar trends. Mg, Sr and Ba show a significantly increasing concentration towards the rim of each sample (figure 4-22). For DIV05, this trend is only interrupted by a sharp dip where the transect intercepts with a grain boundary. This dip coincides with a sharp increase in P by an order of magnitude.

The trends in ROS01 seem to be significantly altered by a whitish layer half-way from core to rim. All of the plotted elements asides P show changing slopes (Mg, Sr, and Ba) or even a trend reversal (U) around this layer. The sample is party coated by a milky layer at the margin of the sample that is characterized by a strong increase in P by two orders of magnitude.

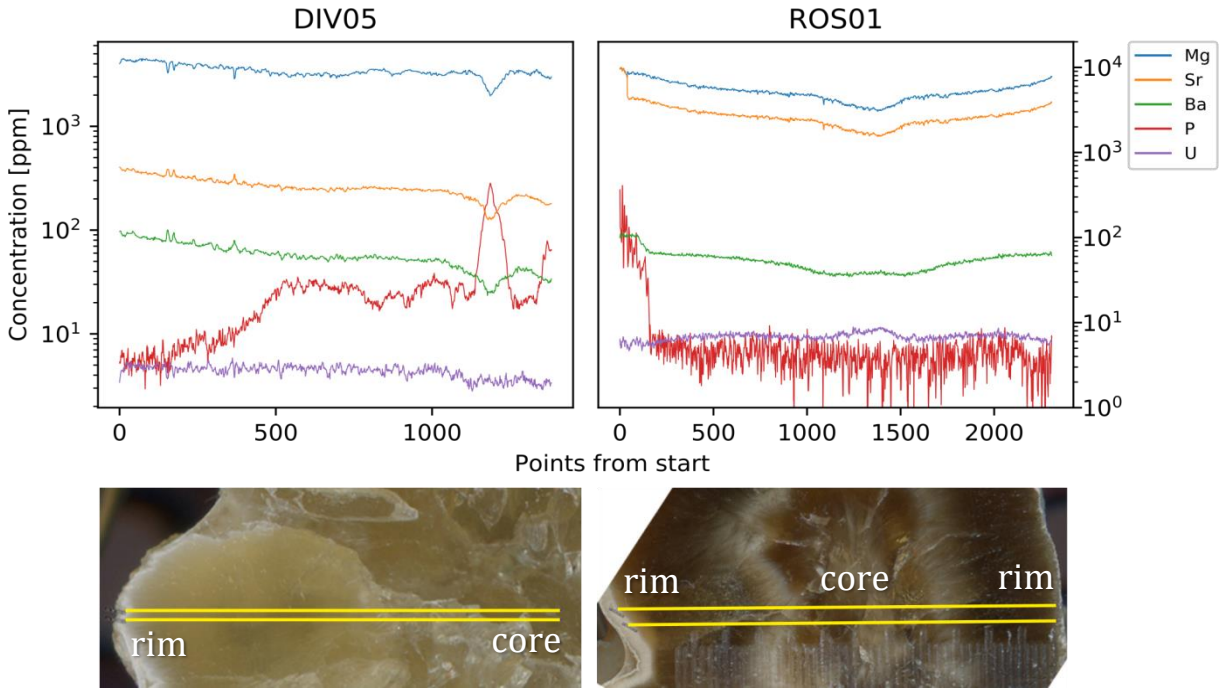

Figure 4-22: LA-ICP-MS profiles across polished slabs of samples DIV05 and ROS01.The plotted data are mean values of two separately measured ablation transects (yellow lines on lower panel). Only the 5 elements that show significant trends are shown.

In more general terms, ROS01 (split to spherulitic multi-aggregate) shows significantly higher concentrations of Mg, Ba, U and most notably Sr, as compared to DIV05 (blocky to split multi-aggregate). Also, the relative increase in Mg and Sr from core to rim is stronger in ROS01 (table 4-3). For Ba the relationship is reversed.

4.2.8 U/Th Dating

Of the samples presented in this chapter, U/Th data is only available for DIV38, NU8a, NU8b, NU8c, USV01, USV02, USV03, VIA01 and VIC05_glen (table 4-4). U concentrations are variable across all samples, ranging from 584.1 ±0.5 ppb (NU8c) up to 18,661.3 ±34.8 ppb (USV02). $^{230}Th/^{232}Th$ ratios, a measure for contamination with detrital Th, are ranging from 2,145 ±43 to 456,612 ±29,454. These values indicate that detrital contamination, which would compromise the precision of ages, is negligible. The samples are well suited for U/Th dating.

Sample VIC05_glen is an exception to the generally satisfying sample quality with respect to U/Th analysis. The $^{230}Th/^{232}Th$ ratio is 21, which is a very low value and suggests significant amount of contamination with detrital ^{232}Th. The resulting error amounts to 14% of the absolute age of 25,172 years, which renders the sample inadequate for paleoclimatic interpretation.

The ages cluster around interglacial periods and correlate to periods of increased or increasing summer insolation at 65° northern latitude (figure 4-23). An important aspect about the aliquots of sample NU8 is that they are not coeval. NU8a formed during the same climatic interval as DIV38 (GS24, Rasmussen et al., 2014). However, NU8b and NU8c are significantly younger (GS23), even though they were found in situ with NU8a.

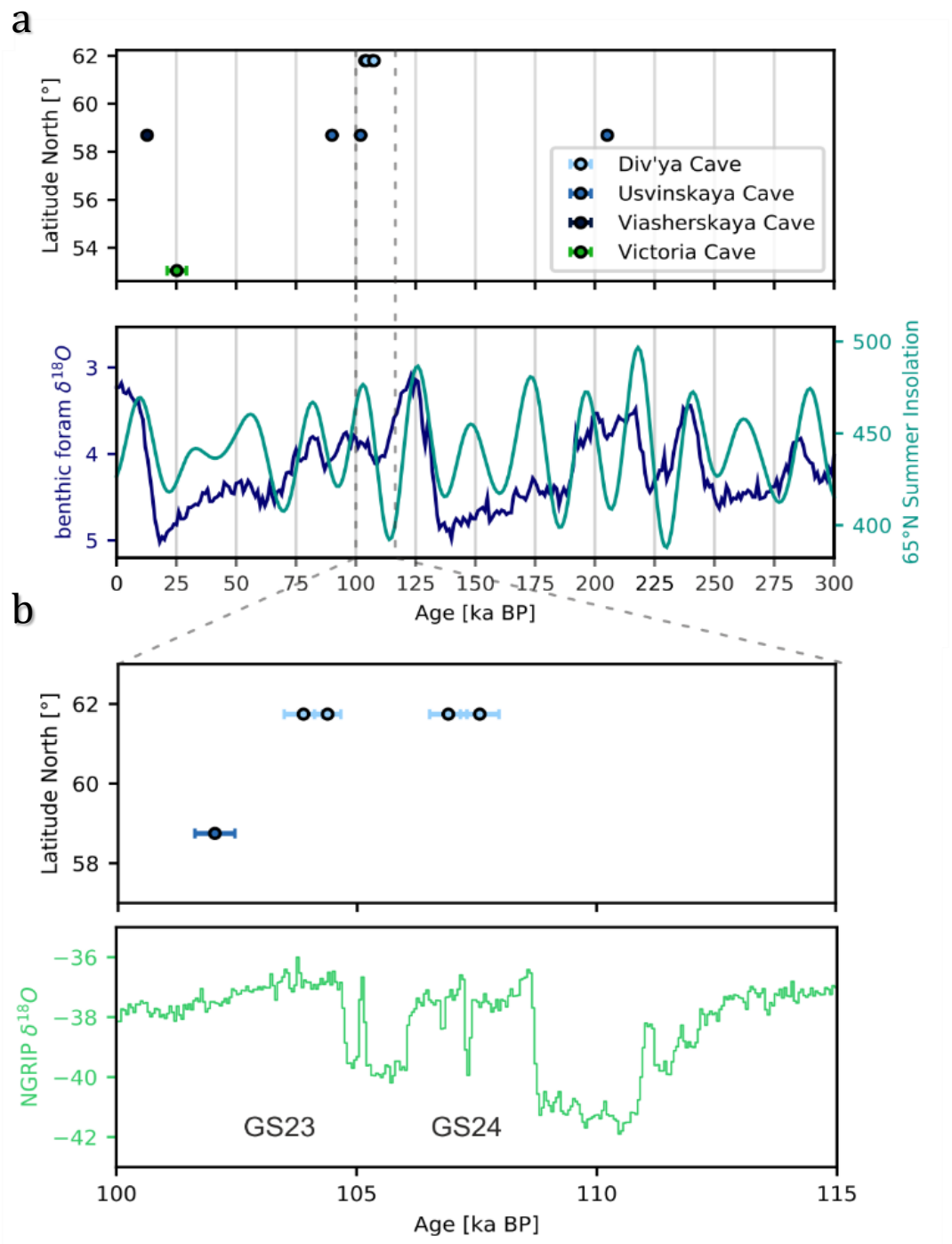

Figure 4-23: Ages of CCC samples presented in this chapter. **a)** compared to a record of benthic foraminifera $\delta^{18}O$ which is a proxy for global ice volume (Lisiecki and Raymo, 2005) and **b)** compared to the NGRIP ice core $\delta^{18}O$ (Andersen *et al.*, 2004). Solar irradiance at 65°N is reported in [Wm^{-2}] (Berger and Loutre, 1991).

Table 4-4: Summarized results of U/Th dating. The decay constants used for age calculations were $\lambda_{238} = 1.55125*10^{-10}$ (Jaffey et al., 1971), $\lambda_{234} = 2.82206*10^{-6}$ (Cheng et al., 2013) for U and $\lambda_{230} = 9.1705*10^{-6}$ for Th (Cheng et al., 2013). $\delta^{234}U_{initial}$ was calculated based on ^{230}Th age (T), i.e., $\delta^{234}U_{initial} = \delta^{234}U_{measured} * e^{\lambda 234*T}$. The values for $\delta^{234}U$ are computed with $\delta^{234}U = ([^{234}U/^{238}U]_{activity} - 1)*1000$. Corrected ^{230}Th ages assume the initial $^{230}Th/^{232}Th$ atomic ratio of $4.4 \pm 2.2*10^{-6}$. Those are the values for a material at secular equilibrium with the bulk earth $^{230}Th/^{238}U$ value of 3.8. The errors are arbitrarily assumed to be 50%. Corrected ^{230}Th ages are reported in years before present [yBP], whereas "present" means the year 1950 A.D.

Sample ID	^{238}U [ppb]		^{232}Th [ppt]		^{230}Th / ^{232}Th (atomic x10^{-6})		$d^{234}U$ (measured)		^{230}Th / ^{238}U (activity)		^{230}Th Age (yr) (uncorrected)		$d^{234}U_{Initial}$ (corrected)		^{230}Th Age [yBP] (corrected)	
NU08a	1289.7	±1.9	6800	±136	4084	±82	955.4	±2.6	1.3059	±0.0024	107049	±387	1292	±4	106915	±390
NU08b	2217.0	±3.6	5794	±116	7186	±145	751.1	±2.5	1.1389	±0.0023	103982	±404	1007	±3	103877	±404
NU08c	584.1	±0.5	8207	±164	2145	±43	1728.0	±2.7	1.8277	±0.0024	104573	±263	2320	±4	104383	±277
DIV38	1838.9	±2.3	606	±14	72023	±1722	1135.6	±2.3	1.4395	±0.0031	107645	±405	1539	±4	107574	±405
USV 01	1608.5	±2.9	134	±9	456612	±29454	1392.0	±3.3	2.3120	±0.0062	205199	±1464	2484	±12	205131	±1464
USV 02	18661.3	±34.8	5651	±114	63959	±1289	822.5	±2.3	1.1746	±0.0028	102090	±420	1097	±3	102018	±420
USV 03	1645.0	±3.4	2782	±56	20161	±408	2392.4	±4.4	2.0683	±0.0052	90135	±358	3085	±6	90056	±358
VIA 01	3142.6	±8.5	200	±5	103610	±2581	2563.2	±5.5	0.4005	±0.0013	12825	±49	2658	±6	12757	±49
VIC05_glen	997.0	±1.5	272981	±5471	21	±0	401.8	±2.6	0.3505	±0.0020	30938	±210	431	±6	25172	±4051

5 Numerical Modelling of Stable Isotope Trends

To interpret the trends observed in stable isotopic composition of CCC a forward modelling approach was chosen. The annotated model code (python 3.6) has been added to the appendix. The model is based on the approach of Žák et al. (2004) but additionally incorporates certain aspects of a more sophisticated model by Kluge et al. (2014a).

The isotopic evolution is computed based on Rayleigh distillation (eq. 5):

$$\delta_e(f) = (1000 + \delta_{e0}) * f^{(\alpha-1)} - 1000 \quad (5)$$

Where f is the residual fraction of the educt phase, $\delta_e(f)$ is the isotopic composition of the educt at fraction f, δ_{e0} is the educt's starting composition, and α is the fractionation factor from educt to product phase. The isotopic composition of the product phase $\delta_p(f)$ is defined as

$$\delta_p(f) = \alpha * (\delta_e(f) + 1000) - 1000 \quad (6)$$

Values are calculated iteratively at a resolution of $df = 1000^{-1}$. The fractionation factors used are reported in table 5-1.

The model is initialized with starting values for $\delta^{13}C_0$ and $\delta^{18}O_0$, representing the isotopic composition of the parent solution at the onset of CCC precipitation. Subsequently the evolution of $\delta^{18}O$ is calculated for ice, residual water and carbonate precipitate using Rayleigh distillation (eq. 5) for the educts and co-evolving product phases according to (eq. 6).

For the $\delta^{18}O$ evolution, the model is simply an application of these equations to the system *water – ice – calcite* with the corresponding values for α taken from table 5-1. Figure 5-1a shows model predictions for a starting composition of $\delta^{18}O_{water}$ = -13‰.

Table 5-1: List of fractionation factors used for numerical modelling of CCC isotopic evolution. Notation is $\alpha_{product\text{-}educt}$.

Fractionation	Value extrapolated to 0°C	Reference
$^{18}\alpha_{ICE\text{-}WATER}$	1.0029	Lehmann and Siegenthaler (1991)
$^{18}\alpha_{CC\text{-}WATER}$	1.0359	Friedman and O'Neil (1977)
$^{13}\alpha_{CO2\text{-}HCO3}$	0.9892	Mook and de Vries (2000)
$^{13}\alpha_{CC\text{-}HCO3}$	0.9996	Mook and de Vries (2000)

The evolution of $\delta^{13}C$ in the system is also modelled as a Rayleigh process. However, fractionation factors are treated as endmembers of a spectrum between fully closed and fully open system with respect to CO_2 degassing. The fully closed system only considers the contribution of carbonate precipitation ($^{13}\alpha_{cc\text{-}HCO3} = 0.9996$) to the isotopic evolution and neglects degassing of CO_2. The open system on the other hand assumes saturation with respect to CO_2, causing degassing at each incremental step ($^{13}\alpha_{CO2\text{-}HCO3} = 0.9892$). The isotopic composition of the carbonate precipitate is calculated based on equation (6) from the enriched HCO_3^- after degassing. As shown in figure 5-1a, this scenario leads to very heavy $\delta^{13}C_{cc}$ values at late stages of the Rayleigh process.

As a novel addition to the original version of the model (Žák et al., 2004), hybrid scenarios between fully closed and fully open are introduced. Like the end-member scenarios (fully open- and fully closed system), hybrid scenarios are modelled using equations (5) and (6). Instead of using either $^{13}\alpha_{CO2\text{-}HCO3}$ or $^{13}\alpha_{cc\text{-}HCO3,}$ however, a combined fractionation factor $^{13}\alpha_{tot}$ is calculated as

$$^{13}\alpha_{tot}(i) = \frac{i * {}^{13}\alpha_{cc-HCO3} + (1-i) * {}^{13}\alpha_{CO2-HCO3}}{\sqrt{2}} \qquad (7)$$

$$where\ 0 \leq i \leq 1.$$

The factor i refers to the relative contribution of the closed system component starting from a fully closed system ($i = 1$, i.e. 0% open system) to a fully open system ($i = 0$, i.e. 100% open system). Model prediction of the isotopic evolution of $\delta^{13}C_{cc}$ are depicted in figure 5-1a for a starting composition of $\delta^{13}C_{HCO3} = -12.0‰$ [VPDB].

Figure 5-1b displays model predictions in $\delta^{18}O$ - $\delta^{13}C$ space alongside stable isotope data of CCC_{coarse} from the Ural Mountains. For this example, the model was initiated with a starting composition of $\delta^{18}O_{water} = -13.0‰$ [VSMOW] and $\delta^{13}C_{HCO3} = -12.0‰$ [VPDB]. Most measured data are comparable to modelled hybrid systems with 10% – 20% of overall contribution open system degassing of CO_2. However, measured data plot away from the model's point of origin. Moreover, some of the internal slopes (e.g. ROS01 and USV02) cannot be explained by numerical modelling using the starting values of this particular example. Overall, the model reproduces the isotopic trends associated with CCC_{coarse}. Shortcomings arise on sample-by-sample scale and will be addressed in the subsequent chapters.

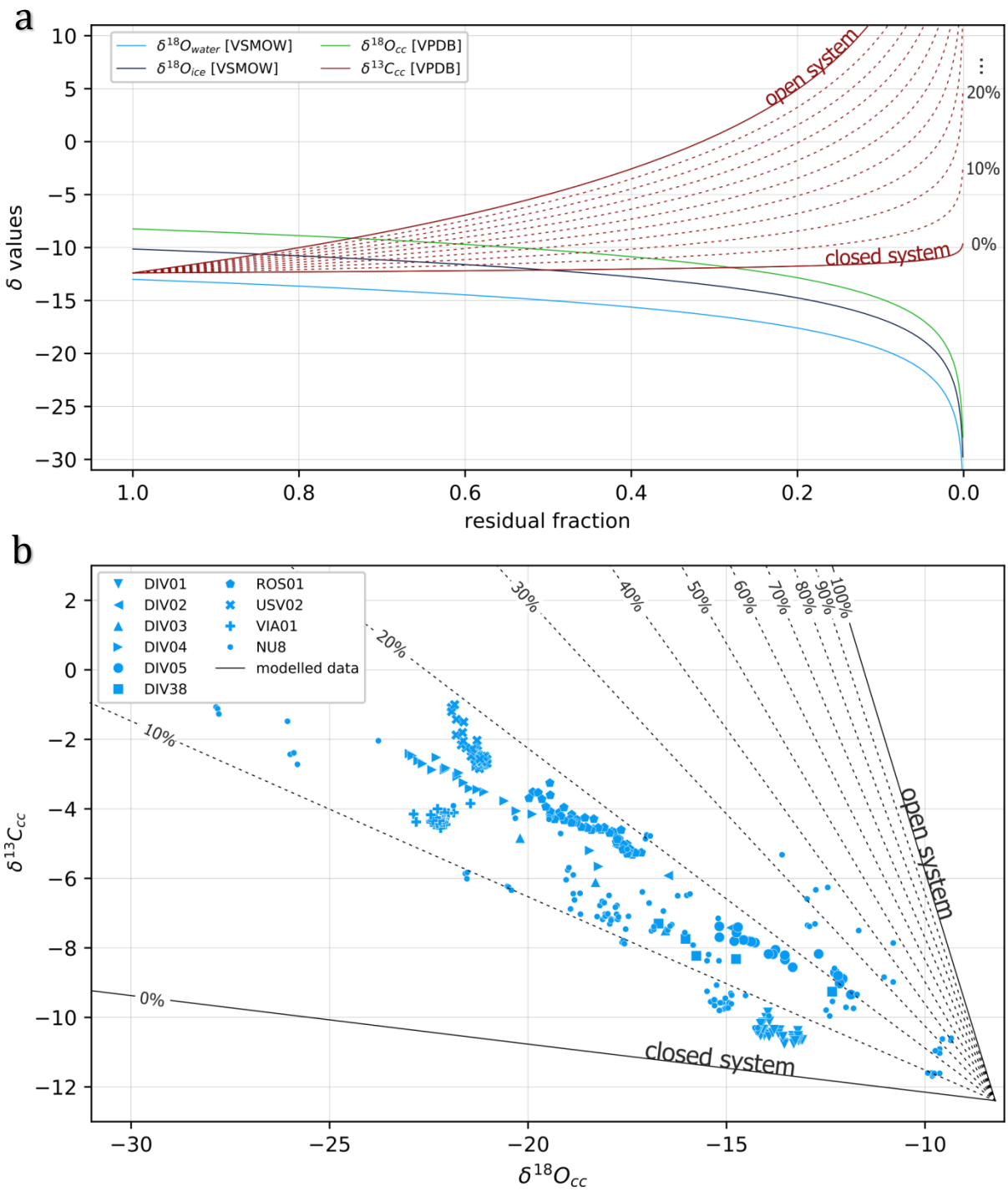

Figure 5-1: Modelled isotopic evolution of CCCs. In the depicted scenario, the Rayleigh process was initiated with a starting composition of $\delta^{18}O_{water}$ = -13.0‰ [VSMOW] and $\delta^{13}C_{HCO3}$ = -12.0‰ [VPDB], representing the systems state at the onset of CCC precipitation. **a)** Lines correspond to the evolution of O and C isotopes in relevant phases of the system. For $\delta^{13}C_{cc}$, a closed and an open system scenario with respect to degassing of CO_2 were evaluated. Dashed lines represent hybrid scenarios and percentages quantify the open system contribution to the overall fractionation. The graph is cut off at +10‰ for scaling purposes. **b)** Evaluation of the proposed model. Both open and closed systems, including intermediate scenarios are plotted against stable isotope measurements of CCCs from the Ural Mountains. Scenarios between 10% and 20% of open system contribution manage to reproduce the isotopic evolution of most samples.

6 Interpretation and Discussion

6.1 Stable Isotopic composition of CCC_{coarse}

The question of how morphology should be reflected in stable isotopes hinges on the predictive capability of the genetic model (Žák et al., 2004; Žák et al., 2008; Žák et al., 2012; Žák et al., 2018). Figure 6-1 depicts the isotopic evolution of a system during freezing and CCC precipitation. Progressive freezing of water leads to lower $\delta^{18}O_{water}$ values ($\alpha_{water\text{-}ice} = 1.0029$ Lehmann and Siegenthaler, 1991). Assuming a closed system where CO_2 cannot escape, a pool of water with composition (A) would gradually move towards (B). Arriving at (B), saturation with respect to calcite is reached ($SI_{cc} > 1$) and precipitation of carbonate composed of heavy isotopes begins (light grey dots). Stoichiometrically, each mole of $CaCO_3$ precipitate also produces one mole of CO_2 which will shift the remaining HCO_3^- towards heavier $\delta^{13}C$ values ($\alpha_{CO2\text{-}HCO3} = 0.9880$ Mook and de Vries, 2000). Similarly, the precipitate will preferentially remove ^{12}C from the solution at 0 °C but less efficiently ($\alpha_{CaCO3\text{-}HCO3} = 0.9996$ Mook and de Vries, 2000). The effects of CO_2 concentration on pH and SI_{cc} are neglected for the time being. Eventually precipitation will cease at point (C) because the available HCO_3^- has been consumed ($SI_{cc} \leq 1$), the sample is entrapped in ice or because lowered pH due to rising $CO_{2(aq)}$ concentration inhibits precipitation.

The stable isotope composition of the solution doesn't necessarily have to follow the pathway (A) – (B) – (C) though. An open system with respect to the degassing of CO_2 would rapidly rise in $\delta^{13}C$ until calcite saturation is reached. This pathway (D) – (B) is comparable to the process of "normal" speleothem precipitation and does not require freezing to induce mineral precipitation. However, it is useful to think of this process as a hypothetical endmember, contrary to the completely closed system pathway (A) – (B).

In reality, a mix between both (A) – (B) and (D) – (B) is likely to occur. Initial degassing occurs until the cave pool has superficially frozen and developed an ice lid, inhibiting further degassing, following roughly the pathway (E) – (B).

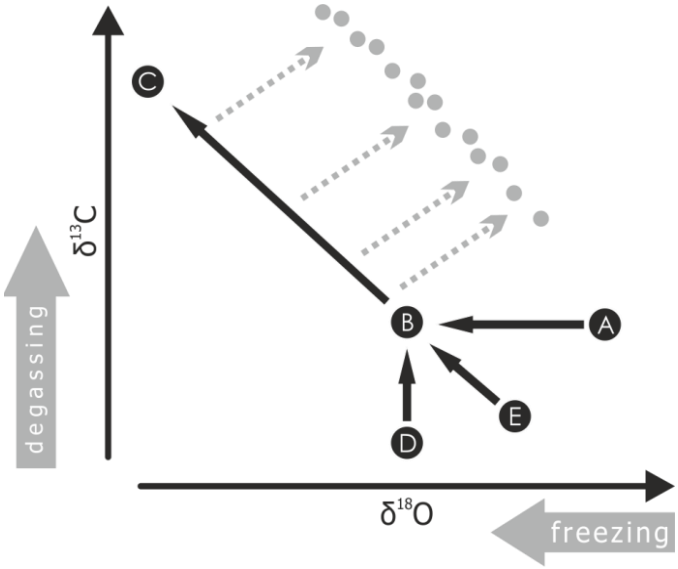

Figure 6-1: Schematic model of the isotopic evolution of $\delta^{13}C$ and $\delta^{18}O$ in the solution during CCC formation. Light grey dots show a hypothetic stable isotope transect through a CCC sample, similar to those presented in chapter 4.2. Points A, D and E represent the isotopic signatures of three different parent solutions before the freezing process begins. B and C correspond to the isotopic composition of the solution at the onset of cryogenic precipitation of $CaCO_3$. Light grey arrows indicate how freezing of water and degassing of CO_2 would qualitatively change the solutions isotopic signature. For a detailed explanation refer to the main text.

Figure 6-2 shows how differences in slope and position of isotopic trends in $\delta^{18}O$ – $\delta^{13}C$ space can be rationalised. The following elaborate on this conceptual model.

6.1.1 $\delta^{18}O$ evolution

The position of a sample along the $\delta^{18}O$ axis can be altered by three factors:

- The starting $\delta^{18}O_{water}$ value of the parent solution,
- the saturation state of the parent solution at the time of infiltration into the cave and
- the extent of freezing prior to precipitation.

Without further analytical constraints, it is not possible to attribute a quantitative contribution to one of these factors. Fluid inclusion data – in the best case – can provide information about the solution at the onset of precipitation, which presumably happens after a significant shift in $\delta^{18}O_{water}$ due to prior freezing. However, most of the acquired fluid inclusion data lies within roughly 2 ‰ $\delta^{18}O$ of the GMWL. According to Rayleigh fractionation ($\alpha_{water\text{-}ice} = 1.0029$ Lehmann and Siegenthaler, 1991) a shift of -2.00‰ $\delta^{18}O_{water}$ corresponds to 51% of ice formed. A shift of -5.00‰ $\delta^{18}O_{water}$ would already require 83% of ice formation. Assuming freezing of average karst water[2] in open system conditions, it is unlikely that saturation would take so long to be achieved. In a closed system, the effects of CO_2 accumulation on pH need to be considered. This has not been done so far in a quantitative sense, highlighting an important gap in our understanding of CCC_{coarse} precipitation.

The second factor is rooted in the natural variability of cave waters. Again, fluid inclusion data provide important constraints. Compared to modern precipitation from the Ural area (GNIP database, figure 4-16) fluid inclusions from CCC_{coarse} are situated on the lighter end of the spectrum. In theory, freezing shifts the isotopic composition of water towards lower values along a slope of 7 (Lehmann and Siegenthaler, 1991) as compared to 8 for the GMWL. Empirical data from cave ice yield similar results (Perşoiu et al., 2011). Consequently, the observed tendency towards lower values can at least partly be attributed to prior freezing.

6.1.2 $\delta^{13}C$ evolution

Two factors primarily influence the relative position of a sample with respect to $\delta^{13}C$.

- The initial $\delta^{13}C$ value of DIC of the infiltrating water and
- degassing of isotopically light CO_2 prior to precipitation.

[2] There is very little information about the actual composition of CCC forming water. The assumption of "normal" karst water might be a red herring.

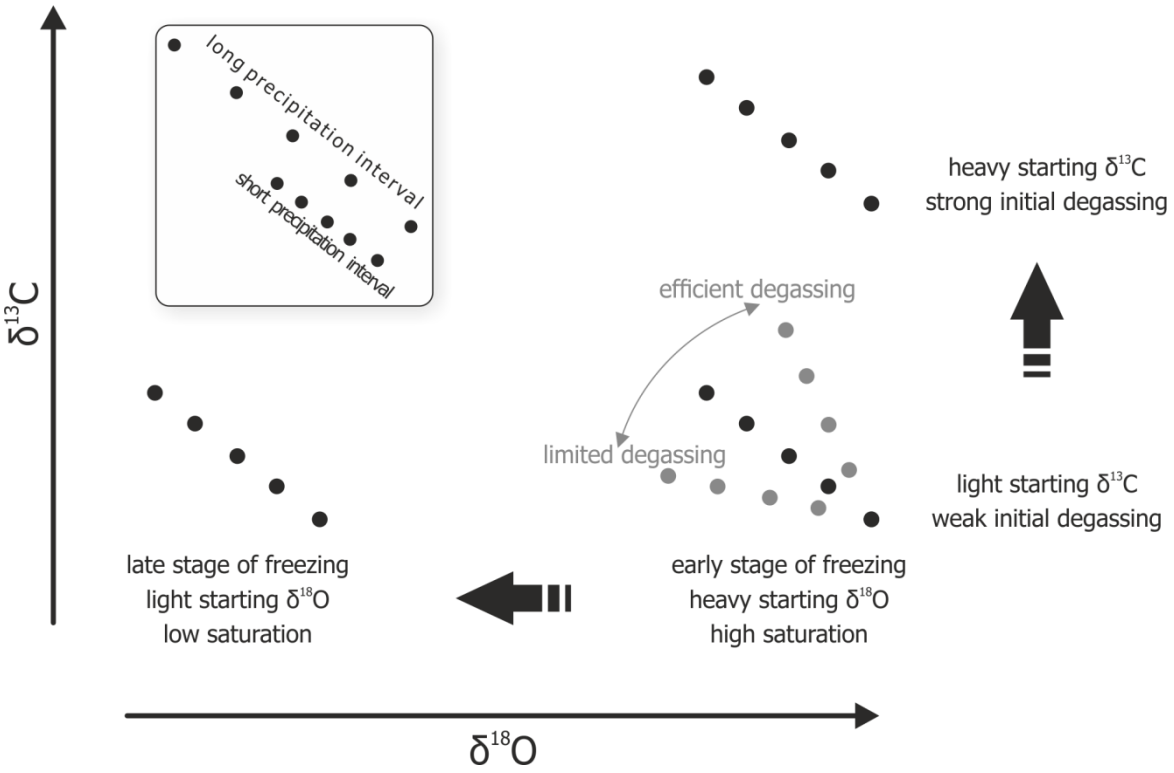

Figure 6-2: Conceptual model on the interpretation of isotopic trends observed in CCCs. Black dots schematically depict the isotopic composition of a CCC specimen along a transect.

The isotopic composition of DIC acquired prior to infiltration into the cave chamber is unequivocally a strong contributor to $\delta^{13}C_{cc}$ in cave calcite. In speleothem research, this measure is usually interpreted as a proxy for biological soil activity, that can sometimes even provide quantitative constraints on paleo-temperatures (Johnston et al., 2018). With respect to CCCs, higher values of $\delta^{13}C_{cc}$ have been attributed to higher cave elevation and stronger ventilation (Žák et al., 2018) or vegetation density above the cave. Both of these parameters are well constrained for the data presented herein due to careful choice of sample locations, and prominent contributions can be excluded.

In poorly ventilated cave chambers, gaseous CO_2 in the cave atmosphere equilibrates with DIC in proximity to the water/air interface within seconds (Dreybrodt and Scholz, 2011). The *open system* term of the genetic model of CCC_{coarse} formation refers to this situation. In a stagnant water pool however, equilibration slows down exponentially with increasing depth in the water column (Kluge et al., 2014a). As a result, $\delta^{13}C_{cc}$ values are enriched with depth (Wiedner et al., 2008).

In figure 6-2, initial degassing prior to carbonate precipitation causes $\delta^{13}C_{cc}$ to increase. This process is well documented and is the main driver of regular speleothem formation (Fairchild and Baker, 2012). For CCCs however, freezing and degassing cannot be uncoupled so easily, since freezing induced supersaturation will affect the concentration of DIC species and therefore cause degassing. Initial degassing forced by progressive freezing of water will therefore always be accompanied by lowering of $\delta^{18}O_{water}$ to some extent.

Like with shifts in $\delta^{18}O_{cc}$, it is difficult to quantitatively attribute changes in $\delta^{13}C_{cc}$ to either initial degassing or DIC starting composition.

6.1.3 Slope of the $\delta^{18}O$ - $\delta^{13}C$ trend

During precipitation of $CaCO_3$ three factors (partly depicted in figure 6-1) determine the isotopic evolution of the system:

- Precipitation rate of the calcite,
- freezing rate of water,
- and rate of CO_2 degassing.

Depending on which process is dominant, the slope of the resulting isotope transect will change (figure 6-2). Conceivably, the relative contribution of each process will be subject to change with variations in pH and SI_{cc}, which would result in a non-linear trend.

In a poorly ventilated cave chamber, heat flux from infiltrating water hinges almost exclusively on the heat capacity of the host rock (Luetscher and Jeannin, 2004; Luetscher et al., 2008), which is effectively constant in karst environments. The freezing rate of water is therefore unlikely to change significantly. This makes CO_2 degassing rate the dominant factor for the slope of the isotopic evolution during CCC_{coarse} precipitation as depicted in figure 6-2.

6.1.4 Spread if isotope data

Observed spread in $\delta^{18}O_{cc}$ can be accounted for with gradual depletion in heavy ^{18}O of the residual liquid during freezing of water in equilibrium with precipitating calcite. Because of the exponential nature of the Rayleigh process, the rate of change of $\delta^{18}O$ increases progressively. Early precipitates are consequently expected to show less spread per freezing increment than late precipitates. The inference that longer precipitation intervals "*record*" more variability is trivial. Consequently, it can be stated that the range of $\delta^{18}O_{cc}$ values covered in a sample relates to two fundamental aspects.

- The length of the freezing interval during which precipitation took place,
- and the relative position of said interval from start to end of the Rayleigh process.

6.1.5 Interpretation of CCC trends

In the light of these theoretical considerations the position of an individual sample in $\delta^{18}O$ – $\delta^{13}C$ space can be interpreted. It must be noted however, that the conceptual model outlined beforehand is simplified. Potential contributions to the isotopic evolution due to i) disequilibrium effects between water and DIC at high precipitation rates, ii) O equilibration between HCO_3^- and $CO_{2(aq)}$ and iii) effects introduced by speciation of C at various pH values are not accounted for. Points i) and ii) have been addressed in a quantitative sense by Kluge et al. (2014a), but have not been empirically shown to contribute significantly to the isotopic trends observed in CCC_{coarse}.

Samples DIV01, DIV02, DIV03, DIV05 and DIV38 originate at the lower right-hand side of the CCC_{coarse} trend (figure 4-11). Accordingly, these samples are considered early precipitates from waters with comparably high SI_{cc}. For sample DIV01, this notion is emphasized by the low spread of $\delta^{18}O_{cc}$, indicating either early precipitation and/or a short precipitation interval. The light $\delta^{13}C_{cc}$ composition and rather flat slope might indicate inefficient degassing both prior to and after the starting point of precipitation.

Samples DIV02, DIV03, DIV05 and DIV38 all show considerable spread of isotopic data. Comparably heavy $\delta^{18}O_{cc}$ indicates precipitation at an early stage, which in turn points to a relatively long precipitation interval as an explanation for the spread. The $\delta^{13}C_{cc}$ are heavier than for DIV01 indicating either substantial degassing prior to precipitation, or weaker biological soil activity above the cave chamber during formation.

The upper left corner of figure 4-11 hosts samples DIV04, ROS01, USV03 and VIA01. The light $\delta^{18}O_{cc}$ and heavy $\delta^{13}C_{cc}$ values combined provide evidence for significant freezing induced degassing prior to precipitation. Variations in initial water composition are unlikely to cause such large variations. This observation provides further constraints to interpret the spread of isotope properties in the samples. Late precipitates are expected to show larger internal variability caused by the steepness of the Rayleigh process towards the end. However, VIA01 and USV02 cluster tightly with respect to $\delta^{18}O_{cc}$ indicating very short precipitation intervals.

The individual grains of sample NU8 scatter along an extremely wide range of $\delta^{18}O_{cc}$ and $\delta^{13}C_{cc}$ values (figure 4-12). U/Th ages of selected morphologies suggest that multiple generations of CCC_{coarse} may be present (age difference ca. 3000 years). This introduces additional uncertainties with respect to the starting composition of infiltrating water, as both $\delta^{18}O_{water}$ and $\delta^{13}C_{HCO3}$ are likely to vary with time. Moreover, it is not possible to reproduce the variability of sample NU8 without introducing variability in the starting composition. These analytical observations imply that sample NU8 is an accumulation of multiple generations of CCC_{coarse} that have formed over the course of at least 2250 years during the last interglacial period.

6.2 Relationship between Chemistry and Morphology

The stable isotope transects indicate that multi-aggregates cover a wider range of values in the $\delta^{18}O$ – $\delta^{13}C$ plot, than the morphologically homogeneous spherulitic aggregates. Multi-aggregates thus track the isotopic evolution of the system over a larger part of the freezing process. As shown in figure 4-10, for each individual sample stable isotope values will always increase with respect to $\delta^{13}C_{cc}$ and decrease with respect to $\delta^{18}O_{cc}$ from core to rim. In a similar fashion, the fabric changes from low to high propensity to crystal splitting. These observations suggest a causal connection between the evolutionary state of the system and the crystal morphology that is being produced.

Calcite fabrics of common speleothems (i.e. stalagmites and flowstones) have previously been related to SI_{cc}, pH, drip rate, Mg/Ca ratio and impurity content of the solution from which carbonate minerals precipitate (Frisia, 2015). In most cases, these relationships are based on empirical observations like the comparison of recently formed stalagmites with monitoring data on drip water chemistry and cave ventilation. Direct crystallographic evidence explaining structural variations is rare (Frisia et al., 2000; Demény et al., 2017). For CCC_{coarse} in particular, research focusing on morphology is even more so in its infancy. Some authors have analysed their samples using XRD, but the data was hardly discussed beyond qualitative phase analyses (Richter et al., 2010; Spötl and Cheng, 2014; Colucci et al., 2017). Richter and Riechelmann (2008) provide details on the crystallographic orientation of crystallites and report significantly diverging c-axes by 40° within a fan-like sub crystal of a spherulitic sample.

Similarly, only little data on the chemical composition of CCC_{coarse} were published. Richter et al. (2010) briefly mention qualitative observations of rare earth element and Mn^{++} distribution through cathodoluminescence. Chaykovskiy et al. (2014) studied samples from the same caves as reported herein with electron microscopy and found low normative contents of $MgCO_3$ and $CaSO_4$ without indications of zoning.

In section 4.2, data on trace element composition and X-ray diffraction patterns are reported. Contrary to Chaykovskiy et al. (2014), LA-ICP-MS transects show a clearly increasing trend from core to rim of both analysed samples (DIV05 and ROS01). Freezing induced supersaturation implies a gradually increasing ionic strength of the residual aqueous solution which consequently will increase partitioning coefficients with respect to compatible trace elements such as Mg, Sr or Ba (Stoll et al., 2012). The increasing trend towards higher trace element content from core to rim of a sample is therefore in agreement with the accepted genetic model of CCC formation (Žák et al., 2018). Relative increases in Mg, Sr and Ba along the growth axes are thus expected to be found in other CCC samples as well.

Variations in lattice parameters were inferred from minute shifts of XRD peak positions of spherulitic CCC samples (DIV01 and NU8a), relative to morphologically less evolved samples (DIV10, NU8b and NU8c). Based on the available data, spherulitic morphology can therefore be related to small unit cells.

The Mg concentration of the parent solution can modify the crystallization mechanism of calcite, causing lattice strain and giving rise to elongated crystal habit (Davis et al., 2000). Mg has also been shown to affect calcite lattice parameters in biogenic formations (Paris et al., 2011). Both observations are related to the relatively small ionic radius of Mg^{++} (72 pm) as compared to Ca^{++} (100 pm). Experimental studies have found a link between the incorporation of divalent cations with ionic radii smaller than Ca^{++} and the formation of spherulites through non-crystallographic branching (Fernández-Díaz et al., 2006).

Therefore, a connection between calcite fabrics in CCC_{coarse} and rising Mg^{++} concentrations due to freezing induced supersaturation can be proposed. A parent solution gradually accumulates Mg that is rejected from the forming ice. Experiments have shown that the segregation coefficient between water and ice is larger for Mg^{++} than for Ca^{++} and Sr^{++}, amplifying the partitioning of Mg^{++} into calcite (Killawee et al.,

1998). The chemically forced incorporation of Mg gradually distorts the crystallographic unit cells and leads to increasing disorder and spherulitic growth.

This model can, to a certain extent, explain the trend from blocky to split fabric that is the base of the morphological classification proposed in section 4.1. Factors like growth rate, SI_{cc} or pH cannot be ruled out from contributing to the macroscopic morphology of CCC_{coarse}. However, these factors are difficult to constrain analytically, as was shown in section 6.1. The presented dataset is too small to state a causal relationship with high confidence, but certainly opens directions for future, more dedicated research efforts.

6.3 Metastable Precursors to Calcite

Metastable precursor phases have been a subject of discussion since the very beginning of analytical studies revolving around CCCs (Žák et al., 2004). In a carbonate system at temperatures close to freezing, four $CaCO_3$ polymorphs are commonly mentioned:

- Ikaite ($CaCO_3 * 6\ H_2O$, monoclinic)
- Monohydrocalcite ($CaCO_3 * H_2O$, trigonal)
- Vaterite ($CaCO_3$, hexagonal)
- Amorphous $CaCO_3$ (ACC)

All four are unstable at room temperature and ambient pressure and are consequently not expected to be identified by standard XRD analysis. Nevertheless, reports of their finding are numerous, especially in low temperature environments (Jansen et al., 1987; Grasby, 2003; Dahl and Buchardt, 2006).

The TEM analyses performed on sample DIV01 yielded evidence for high degrees of disorder and nano-crystalline grain size distribution. Demény et al. (2016b) reported similar observations alongside other analytical constraints and inferred ACC as a precursor to calcite in a recently forming stalagmite from Hungary. The observed 104 twinning structure has previously been interpreted as an artefact of recrystallization (Larsson and Christy, 2008).

Advances in the understanding of biomineralisation are based on the idea that crystal growth does not necessarily happen in a monomer-by-monomer fashion (de Yoreo, 2003; Checa et al., 2013). Instead, alternative pathways have been proposed involving crystallization by particle attachment (*CPA*, de Yoreo et al., 2015). The generally accepted model proposes that ions, prior to crystallization, form accumulations of different size and structure, including oligomers, amorphous nanoparticles, poorly crystalline nanoparticles or even fully formed nanocrystals. These transitional particles then aggregate in a more or less systematic way to form a bulk crystal. The bulk crystal may then inherit structural artefacts associated with the crystallization pathway in the form of defects and nano-domains. However, CPA calls for in situ observation to be confirmed since structural artefacts cannot be attributed to CPA

unequivocally. Moreover, recrystallization easily overprints CPA artefacts making detection unlikely after a stable phase has been formed.

Experimental studies show that the degree of supersaturation, pH, Mg^{++} concentration and the presence of impurities such as organic polymers are important factors in CPA (Bots et al., 2012; Rodriguez-Blanco et al., 2012). $CaCO_3$ morphologies yielded by some of these studies show striking resemblance to split morphologies observed in CCCs (Sand et al., 2012). Mg^{++} concentration also has significant influence on the stability of metastable $CaCO_3$ polymorphs in carbonate systems (Marland, 1975a, 1975b; Bischoff et al., 1993; Purgstaller et al., 2016; Purgstaller et al., 2017).

The observed structural anomalies in DIV01 strongly suggest non-classical crystallization pathways to play a significant role in the formation of CCCs.

6.4 Fluid Inclusions and Geothermometry

Fluid inclusion analyses on CCC_{coarse} have shown that most of the measured samples contain water resembling comparably light modern-day precipitation with respect to stable isotopic composition. However, significant $\delta^{18}O_{water}$ offset form the GMWL is frequently observed and cannot be explained by analytical error. In fact, some samples appear to be more prone to offset measurements than others (compare VIA01 to DIV38). A linear relationship was found between the amount of offset and the magnitude of erratic pre-CO peaks, suggesting the offset is introduced by interference an unknown compound that is contained in some samples. Further research is required to clarify the origin of the unknown compound.

Because $\delta^{18}O_{water}$ results are clearly compromised by the occurrence of pre-CO peaks, the $\delta^{18}O$ signal was reconstructed by projecting measurements of $\delta^{2}H$ to onto the GMWL. This approach is conventionally used when $\delta^{18}O$ values derived via this method are not trusted (Wainer et al., 2011; Johnston et al., 2013). Effects of freezing prior to fluid entrapment are expected to shift the isotopic composition of the parent solution along a line with a slope of 7 as compared to 8 for the GMWL (Lehmann and Siegenthaler, 1991; Perşoiu et al., 2011). Ideally, these effects would be accounted for when using projected $\delta^{18}O$ values. This would require knowledge of the extent of freezing, which has been shown to be extremely challenging to estimate. However, samples with little to no significant pre-CO peak contribution also show little offset with respect to $\delta^{18}O_{water}$ (e.g. DIV38). This inspires confidence that projected $\delta^{18}O_{water}$ values along the GMWL are an appropriate estimate to use for subsequent thermometry calculations.

The dataset comprising projected $\delta^{18}O_{water}$ and $\delta^{18}O_{cc}$ values can be grouped into two clusters based on their $\delta^{18}O_{cc}$ values. For samples with a $\delta^{18}O_{cc} > -20‰$ [VPDB], the isotopic composition of fluid inclusions and carbonate strongly correlate:

$$\delta^{18}O_{water} = 0.85 * \delta^{18}O_{cc} + 28.64 \quad (8)$$

$R^2 = 0.9622$
$p = 8.56 * 10^{-6}$

Unexpectedly, paleotemperatures derived from fluid inclusion data are consistently above 0 °C for all commonly used equations (Craig, 1965; Friedman and O'Neil, 1977; Kim and O'Neil, 1997; Coplen, 2007; Tremaine et al., 2011). For the correlated part of the data set, temperatures also cluster around the 12 °C isotherm in (figure 4-18). Similar results have been reported previously and attributed to isotopic disequilibrium during cryogenic precipitation (Kluge et al., 2014a). However, a correlation between $\delta^{18}O_{water}$ and $\delta^{18}O_{cc}$ like the one observed in fluid inclusions suggests that there may be a causal relationship between the two measures. Isotopic equilibrium is therefore proposed for values above $\delta^{18}O_{cc}$ = -20‰ [VPDB], contrary to the conclusions drawn by Kluge et al. (2014a). The second cluster of data with a light isotopic composition of $\delta^{18}O_{cc} <$ -20‰ [VPDB] yields temperatures consistently above 20°C and, more importantly, lacks internal correlation.

If the concepts outlined in section 6.1 are applied, the isotopically heavy cluster represents early precipitates as opposed to isotopically light late precipitates in the other cluster. This relationship indicates that cryogenic precipitation starts at or close to isotopic equilibrium. As freezing progresses, equilibrium is lost and kinetic effects become dominant to overall isotope fractionation. This interpretation supports a model where degassing of CO_2 prior to carbonate precipitation, which is a kinetic fractionation process, serves as the primary cause of a samples position in $\delta^{18}O$ - $\delta^{13}C$ space.

Still, the question remains why calculated temperatures are too high. The fractionation factors used for thermometric equations are based on empirical data, either from precipitation experiments or in-situ measurements in caves. Yet, none of them were calibrated at 0 °C. Using these fractionation factors for freezing conditions therefore necessarily involves extrapolation. Moreover, influence of growth rate and chemical composition on fractionation factors has been shown to play a role for aragonite (Kim et al., 2007). Similar effects can be anticipated for other $CaCO_3$ polymorphs. Consequently, there is little reason to expect paleotemperatures derived with conventional fractionation factors to be applicable to cryogenic precipitates without reservation.

Cryogenic precipitation – by definition – occurs at or very close to 0 °C. Assuming that samples with $\delta^{18}O_{cc}$ > -20‰ [VPDB] did in fact precipitate at isotopic equilibrium, the data can be used to calculate a new fractionation factor for oxygen between calcite and water at 0 °C:

$$^{18}\alpha_{cc-water} = \left[\sum_{i=0}^{n} \frac{1000 + \delta^{18}_{i}O_{cc}}{1000 + \delta^{18}_{i}O_{water}}\right] * n^{-1} \quad (9)$$

For the reported data equation (9) yields a value of $^{18}\alpha_{cc-water} = 1.0318 \pm 0.0005$, conventionally denoted as $1000 \ln {}^{18}\alpha_{cc-water} = 31.3 \pm 0.5$. This value can be used with the numerical model presented in chapter 5. To achieve a comparable fit to measured stable isotope data, an initial $\delta^{18}O_{water}$ of -9.0‰ instead of -13.0‰ [VSMOW] must be chosen. Both values are reasonable but lack independent validation.

7 Conclusions

CCC_{coarse} from the Ural Mountains were analysed for isotopic composition of carbonate and fluid inclusion water, X-ray and electron diffraction properties, trace element composition, and were also examined petrographically. A classification scheme based on microscopic fabrics was proposed to simplify morphological description. Moreover, a numerical model of stable isotope evolution was developed to assess different precipitation scenarios and conceptually identify processes that govern the isotopic evolution of cryogenic carbonate precipitation.

In general, results agree with the current understanding of CCC formation and the genetic model (Žák et al., 2018). However, new evidence presented in this contribution made it possible to address some of the open questions that have not been addressed adequately in previous studies.

7.1 The Morphology of CCC_{coarse}

Crystal splitting was identified as the dominant process in the development of calcite fabrics in CCC_{coarse}. LA-ICP-MS and XRD analyses point towards increasing Mg^{++} incorporation due to freezing induced supersaturation as an important factor for the morphological evolution of CCC specimens from core to rim. These findings complement the proposed classification scheme that correlates macroscopic morphology to the propensity for non-crystallographic branching, i.e. crystal splitting. Quantification of physico-chemical properties such as pH or SI_{cc} based on macroscopic morphology is not possible. Morphology however does allow for comparison of samples in that respect in a qualitative sense. Comparison can be enhanced by using stable isotopes to provide further constraints on the composition of the parent solution.

7.2 Adaptations to the Genetic Model

The stable isotopic trends exhibited by CCC_{coarse} with respect to $\delta^{13}C_{cc}$ are attributed to variations in the efficiency of CO_2 degassing from the solution. In accordance with experimental studies (Killawee et al., 1998), a model of degassing by bubble entrapment in ice is proposed. In this model, the efficiency of degassing is determined by the nucleation rate of gas bubbles, which amongst other factors, is influenced by chemical composition and freezing rate of the parent solution. Generally, degassing contributes from 10 to 20% of overall carbon isotope fractionation. It is not possible to reconstruct the original composition of the parent solution from CCCs quantitatively. However, by combining isotopic, petrographic and chemical analyses it is possible to constrain physico-chemical properties in a relative sense.

Paleothermometric calculations suggest isotopic equilibrium during the early stages of precipitation. However, the isotopic fractionation factor ($^{18}\alpha_{cc-water} = 1.0318 \pm 0.0005$) differs significantly from literature values. These observations suggest that extrapolation of experimentally derived fractionation factors to freezing conditions is not appropriate. Previous studies proposing isotopic disequilibrium during CCC precipitation may need to be be re-evaluated (Kluge et al., 2014a).

7.3 Precursor Phases

The existence of glendonites, calcite pseudomorphs after ikaite that were found in situ with calcite CCC_{coarse} unambiguously confirms that CCC forming environments can bring forth $CaCO_3$ polymorphs other than calcite. Furthermore, TEM analyses on sample DIV01 suggest that crystallisation followed a pathway via poorly crystalline or even amorphous precursors to calcite. The model of CPA provides explanatory potential with respect to SI_{cc}, trace element concentration and the presence of organic polymers during crystallisation as unique characteristics of CCC_{coarse} amongst speleothems.

The existence of transitory precursor phases, especially hydrated forms like monohydrocalcite and ikaite, has profound implications on the use of CCC_{coarse} as permafrost markers. Recrystallization dehydration can be accompanied by loss of U and consequently increase dating uncertainties. This study highlights the role of transitional precursors during CCC precipitation and calls for further research to provide constraints on permafrost reconstructions by dating CCC_{coarse}.

8 References

Andersen, K. K.; Azuma, N.; Barnola, J-M; Bigler, M.; Biscaye, P.; Caillon, N. et al. (2004): *High-resolution record of Northern Hemisphere climate extending into the last interglacial period.* Nature 431 (7005). DOI: 10.1038/nature02805.

Bartolomé, M., Sancho, C., Osácar, M.C., Moreno, A., Leunda, M., Spötl, C., Luetscher, M., López-Martínez, J., Belmonte, A. (2015): *Characteristics of cryogenic carbonates in a Pyrenean ice cave (northern Spain)*. Geogaceta 58.

Berger, A.; Loutre, M. F. (1991): *Insolation values for the climate of the last 10 million years.* Quaternary Science Reviews 10 (4), 297–317. DOI: 10.1016/0277-3791(91)90033-Q.

Bischoff, J.L., Fitzpatrick, J.A., Rosenbauer, R.J. (1993): *The Solubility and Stabilization of Ikaite ($CaCO_3$ * $6H_2O$) from 0° to 25°C: Environmental and Paleoclimatic Implications for Thinolite Tufa.* Journal of Geology 101, 21–33.

Bots, P., Benning, L.G., Rodriguez-Blanco, J.-D., Roncal-Herrero, T., Shaw, S. (2012): *Mechanistic Insights into the Crystallization of Amorphous Calcium Carbonate (ACC).* Crystal Growth & Design 12 (7), 3806–3814.

Bourdon, B. (Ed.) (2003): *Uranium-series geochemistry.* Reviews in mineralogy & geochemistry 52. Geochemical Society, Special Issue, 656 pp.

Chaykovskiy, I.I., Kadebskaya, O., Žák, K. (2014): *Morphology, composition, age and origin of carbonate spherulites from caves of Western Urals*. Geochemistry International 52 (4), 336–346.

Checa, A.G., Bonarski, J.T., Willinger, M.G., Faryna, M., Berent, K., Kania, B., González-Segura, A., Pina, C.M., Pospiech, J., Morawiec, A. (2013): *Crystallographic orientation inhomogeneity and crystal splitting in biogenic calcite.* Journal of the Royal Society, Interface 10 (86), 20130425.

Cheng, H., Lawrence Edwards, R., Shen, C.-C., Polyak, V.J., Asmerom, Y., Woodhead, J., Hellstrom, J., Wang, Y., Kong, X., Spötl, C., Wang, X., Calvin Alexander, E. (2013): *Improvements in ^{230}Th dating, ^{230}Th and ^{234}U half-life values, and U–Th isotopic measurements by multi-collector inductively coupled plasma mass spectrometry.* Earth and Planetary Science Letters 371-372, 82–91.

Clark, I.D., Lauriol, B. (1992): *Kinetic enrichment of stable isotopes in cryogenic calcites.* Chemical Geology 102 (1-4), 217–228.

Clark, I.D., Lauriol, B. (1997): *Aufeis of the Firth River Basin, Northern Yukon, Canada: Insights into Permafrost Hydrogeology and Karst.* Arctic and Alpine Research 29 (2), 240.

Colucci, R.R., Luetscher, M., Forte, E., Guglielmin, M., Lenaz, D., Princivalle, F., Vita, F. (2017): *First alpine evidence of in Situ coarse cryogenic cave carbonates (CCC_{coarse}).* Geografia Fisica e Dinamica Quaternaria 40, 53–59.

Coplen, T.B. (2007): *Calibration of the calcite–water oxygen-isotope geothermometer at Devils Hole, Nevada, a natural laboratory.* Geochimica et Cosmochimica Acta 71 (16), 3948–3957.

Craig, H. (1965): *The measurement of oxygen isotope paleotemperatures.* in: Tongiorgi, E. (Ed.), *Stable Isotopes in Oceanographic Studies and Paleotemperatures.* Spoleto Conferences in Nuclear Geology. Proceedings. Consiglio nazionale delle ricerche, Laboratorio di geologia nucleare.

Dahl, K., Buchardt, B. (2006): *Monohydrocalcite in the Arctic Ikka Fjord, SW Greenland: First Reported Marine Occurrence.* Journal of Sedimentary Research 76 (3), 460–471.

Davis, K.J., Dove, P.M., de Yoreo, J.J. (2000): *The role of Mg^{2+} as an impurity in calcite growth.* Science 290 (5494), 1134–1137.

Demény, A., Czuppon, G., Kern, Z., Leél-Őssy, S., Németh, A., Szabó, M., Tóth, M., Wu, C.-C., Shen, C.-C., Molnár, M., Németh, T., Németh, P., Óvári, M. (2016a): *Recrystallization-induced oxygen isotope changes in inclusion-hosted water of speleothems – Paleoclimatological implications.* Quaternary International 415, 25–32.

Demény, A., Németh, P., Czuppon, G., Leél-Őssy, S., Szabó, M., Judik, K., Németh, T., Stieber, J., (2016b): *Formation of amorphous calcium carbonate in caves and its implications for speleothem research.* Scientific reports 6, 39602.

Demény, A., Németh, A., Kern, Z., Czuppon, G., Molnár, M., Leél-Őssy, S., Óvári, M., Stieber, J. (2017): *Recently forming stalagmites from the Baradla Cave and their suitability assessment for climate–proxy relationships.* Central European Geology 60 (1), 1–34.

Dettman, D.L., Reische, A.K., Lohmann, K.C. (1999): *Controls on the stable isotope composition of seasonal growth bands in aragonitic fresh-water bivalves (unionidae).* Geochimica et Cosmochimica Acta 63 (7-8), 1049–1057.

Dreybrodt, W., Scholz, D. (2011): *Climatic dependence of stable carbon and oxygen isotope signals recorded in speleothems: From soil water to speleothem calcite.* Geochimica et Cosmochimica Acta 75 (3), 734–752.

Dublyansky, Y. (2012): *Design of two crushing devices for release of the fluid inclusion volatiles.* Central European Journal of Geosciences 4 (2), 247.

Dublyansky, Y., Kadebskaya, O., Cheng, H., Luetscher, M., Spötl, C. (2015): *Crygenic cave carbonates as an archive of Late Pleistocene permafrost in the Ural Mountains: preliminary results*. Geophysical Research Abstracts 17.

Dublyansky, Y., Kadebskaya, O., Luetscher, M., Cheng, H., I. I. Chaykovskiy, Spötl, C. (2014): *Preliminary data on the Pleistocene history of permafrost in central Urals (Russia) derived from cryogenic cave carbonates.* INQUA-SEQS conference abstract.

Dublyansky, Y., Spötl, C. (2009): *Hydrogen and oxygen isotopes of water from inclusions in minerals: design of a new crushing system and on-line continuous-flow isotope ratio mass spectrometric analysis.* Rapid communications in mass spectrometry 23 (17), 2605–2613.

Dublyansky, Y., Spötl, C., Stienbauer, C. (2009): *Stegbachgraben, a mineralized hypogene cave in the Grossarl valley, Austria.* in: Klimchouk, A., Ford, D. (Eds.), Hypgene Speleogenesis and Karst Hydrogeology of Artesian Basins, Simferopol.

Fairchild, I.J., Baker, A. (2012): *Speleothem Science: From Process to Past Environments,* 1st ed. Blackwell Quaternary Geoscience Series v.3. Wiley-Blackwell, 416 pp.

Fernández-Díaz, L., Astilleros, J.M., Pina, C.M. (2006): *The morphology of calcite crystals grown in a porous medium doped with divalent cations.* Chemical Geology 225 (3-4), 314–321.

Friedman, I., O'Neil, J.R. (1977): Chapter KK: *Compilation of Stable Isotope Fractionation Factors of Geochemical Interest.* in: USGS (Ed.), Data of Geochemistry, 6 ed. US Printing Office, Washington.

Frisia, S. (2015): *Microstratigraphic logging of calcite fabrics in speleothems as tool for palaeoclimate studies.* International Journal of Speleology 44 (1), 1–16.

Frisia, S., Borsato, A., Fairchild, I.J., McDermott, F. (2000): *Calcite Fabrics, Growth Mechanisms, and Environments of Formation in Speleothems from the Italian Alps and Southwestern Ireland.* Journal of Sedimentary Research 70 (5), 1183–1196.

Grasby, S.E. (2003): *Naturally precipitating vaterite (μ-CaCO3) spheres: Unusual carbonates formed in an extreme environment.* Geochimica et Cosmochimica Acta 67 (9), 1659–1666.

Grigor'ev, D.P. (1961): *Ontogeny of Minerals: Lvov Izdatel'stvo L'vovskogo.* english translation (1965). Israel Program for Scientific Translations.

Henderson, G.M. (2006): *Climate. Caving in to new chronologies.* Science 313 (5787), 620–622.

Hill, C.A., Forti, P. (1986): *Cave minerals of the world.* National Speleological Society, Huntsville, Ala., 238 pp.

ICDD, International Centre for Diffraction Data (2015): *PDF4+ Data Base v 4.1503*.

Jaffey, A.H., Flynn, K.F., Glendenin, L.E., Bentley, W.C., Essling, A.M. (1971): *Precision Measurement of Half-Lives and Specific Activities of ^{235}U and ^{238}U.* Physical Reviews C, 4 (5), 1889–1906.

Jansen, J.H.F., Woensdregt, C.F., Kooistra, M.J., van der Gaast, S.J. (1987): *Ikaite pseudomorphs in the Zaire deep-sea fan: An intermediate between calcite and porous calcite.* Geology 15 (3), 245.

Jochum, K.P., Weis, U., Stoll, B., Kuzmin, D., Yang, Q., Raczek, I., Jacob, D.E., Stracke, A., Birbaum, K., Frick, D.A., Günther, D., Enzweiler, J. (2011): *Determination of Reference Values for NIST SRM 610-617 Glasses Following ISO Guidelines.* Geostandards and Geoanalytical Research 35 (4), 397–429.

Johnston, V.E., Borsato, A., Frisia, S., Spötl, C., Dublyansky, Y., Töchterle, P., Hellstrom, J.C., Bajo, P., Edwards, R.L., Cheng, H. (2018): *Evidence of thermophilisation and elevation-dependent warming during the Last Interglacial in the Italian Alps.* Scientific reports 8 (1), 2680.

Johnston, V.E., Borsato, A., Spötl, C., Frisia, S., Miorandi, R. (2013): *Stable isotopes in caves over altitudinal gradients: Fractionation behaviour and inferences for speleothem sensitivity to climate change*. Climate of the Past 9 (1), 99–118.

Kaufman, A., Broecker, W. (1965): *Comparison of ^{230}Th and ^{14}C ages for carbonate materials from lakes Lahontan and Bonneville.* Journal of Geophysical Research 70 (16).

Killawee, J.A., Fairchild, I.J., Tison, J.-L., Janssens, L., Lorrain, R. (1998): *Segregation of solutes and gases in experimental freezing of dilute solutions: Implications for natural glacial systems.* Geochimica et Cosmochimica Acta 62 (23-24), 3637–3655.

Kim, S.-T., O'Neil, J.R., Hillaire-Marcel, C., Mucci, A. (2007): *Oxygen isotope fractionation between synthetic aragonite and water: Influence of temperature and Mg^{2+} concentration.* Geochimica et Cosmochimica Acta 71 (19), 4704–4715.

Kim, S.-T., O'Neil, J.R. (1997): *Equilibrium and nonequilibrium oxygen isotope effects in synthetic carbonates.* Geochimica et Cosmochimica Acta 61 (16), 3461–3475.

Kluge, T., Affek, H.P., Zhang, Y., Dublyansky, Y., Spötl, C., Immenhauser, A., Richter, D.K. (2014a): *Clumped isotope thermometry of cryogenic cave carbonates.* Geochimica et Cosmochimica Acta 126, 541–554.

Kluge, T., Marx, T., Aeschbach-Hertig W., Spötl, C., Richter, D.K. (2014b): *Noble gas concentrations in fluid inclusions as tracer for the origin of coarse-crystalline cryogenic cave carbonates.* Chemical Geology 368, 54–62.

Kotlyakov, V.M., Khromova, T. (2002): *Land Resources of Russia: Maps of Permafrost and Ground Ice,* 1st ed. NSIDC: National Snow and Ice Data Center, Boulder, Colorado.

Kracht, O., Hilkert, A. (2016): *EA-IRMS: Fast and Precise Isotope Analysis of Liquids on a Delta V Isotope Ratio MS with a High Temperature Conversion Elemental Analyzer.* Thermo Scientific Application Note.

Lacelle, D., Lauriol, B., Clark, I.D. (2006): *Effect of chemical composition of water on the oxygen-18 and carbon-13 signature preserved in cryogenic carbonates, Arctic Canada: Implications in paleoclimatic studies.* Chemical Geology 234 (1-2), 1–16.

Lacelle, D., Lauriol, B., Clark, I.D. (2009): *Formation of seasonal ice bodies and associated cryogenic carbonates in Caverne de L'ours, Québec, Canada: Kinetic isotope effects and pseudo-biogenic crystal structures.* Journal of Cave and Karst Studies 71 (1), 48–62.

Larsson, A.-K., Christy, A.G. (2008): *On twinning and microstructures in calcite and dolomite.* American Mineralogist 93 (1), 103–113.

Lehmann, M., Siegenthaler, U. (1991): *Equilibrium oxygen- and hydrogen-isotope fractionation between ice and water.* Journal of Glaciology 37 (125), 23–26.

Lisiecki, L. E.; Raymo, M. E. (2005): *A Pliocene-Pleistocene stack of 57 globally distributed benthic $\delta^{18}O$ records.* Paleoceanography 20 (1), DOI: 10.1029/2004PA001071.

Luetscher, M., Borreguero, M., Moseley, G.E., Spötl, C., Edwards, R.L. (2013): *Alpine permafrost thawing during the Medieval Warm Period identified from cryogenic cave carbonates.* The Cryosphere 7 (4), 1073–1081.

Luetscher, M., Jeannin, P.-Y. (2004): *Temperature distribution in karst systems: The role of air and water fluxes.* Terra Nova 16 (6), 344–350.

Luetscher, M., Lismonde, B., Jeannin, P.-Y. (2008): *Heat exchanges in the heterothermic zone of a karst system: Monlesi cave, Swiss Jura Mountains.* Journal of Geophysical Research 113 (F2), 487.

Luetscher, M., Moseley, G.E., Edwards, R.L. (2017): *Dating the demise of permafrost in South-Western Britain with cryogenic cave carbonates.* Geophysical Research Abstracts 19.

Maleev, M.N. (1972): *Diagnostic features of spherulites formed by splitting of a single-crystal nucleus. Growth mechanism of chalcedony.* TMPM Tschermaks Mineralogische und Petrographische Mitteilungen 18 (1), 1–16.

Marland, G. (1975a): *Phase equilibria in the system calcium carbonate-water*. Geochimica et Cosmochimica Acta 39 (8), 1193–1197.

Marland, G. (1975b): *The stability of $CaCO_3$ ($6H_2O$) (Ikaite).* Geochimica et Cosmochimica Acta 39, 83–91.

Mattey, D.P., Fairchild, I.J., Atkinson, T.C., Latin, J.-P., Ainsworth, M., Durell, R. (2010): *Seasonal microclimate control of calcite fabrics, stable isotopes and trace elements in modern speleothem from St Michaels Cave, Gibraltar.* Geological Society, London, Special Publications 336 (1), 323–344.

May, B., Spötl, C., Wagenbach, D., Dublyansky, Y., Liebl, J. (2010): *First investigations of an ice core from Eisriesenwelt cave (Austria).* The Cryosphere Discuss. 4 (3), 1525–1559.

McDermott, F. (2004): *Palaeo-climate reconstruction from stable isotope variations in speleothems: A review.* Quaternary Science Reviews 23 (7-8), 901–918.

Mook, W., de Vries, J.J. (2000): *Environmental Isotopes in the Hydrological Cycle, Principles and Applications.* Volume 1: Introduction - Theory, Methods, Review.

Müller, W., Shelley, M., Miller, P., Broude, S. (2009): *Initial performance metrics of a new custom-designed ArF excimer LA-ICPMS system coupled to a two-volume laser-ablation cell.* Journal of Analytic Atomic Spectrometry 24 (2), 209–214.

Nakai, N., Wada, H., Kiyosu, Y., Takimoto, M. (1975): *Stable isotope studies on the origin and geological history of water and salts in the Lake Vanda area, Antarctica.* Geochemical Journal 9 (1), 7–24.

Paris, O., Aichmayer, B., Al-Sawalmih, A., Li, C., Siegel, S., Fratzl, P. (2011): *Mapping Lattice Spacing and Composition in Biological Materials by Means of Microbeam X-Ray Diffraction.* Advanced Engineering Materials 13 (8), 784–792.

Pavuza, R., Spötl, C. (2017): *Neue Daten zu Vorkommen und Entstehung kryogener Calcite in ostalpinen Höhlen.* Die Höhle 68 (1-4).

Perşoiu, A., Onac, B.P., Wynn, J.G., Bojar, A.-V., Holmgren, K. (2011): *Stable isotope behaviour during cave ice formation by water freezing in Scărişoara Ice Cave, Romania.* Journal of Geophysical Research 116 (D2), 423.

Purgstaller, B., Dietzel, M., Baldermann, A., Mavromatis, V. (2017): *Control of temperature and aqueous Mg^{2+}/Ca^{2+} ratio on the (trans-)formation of ikaite.* Geochimica et Cosmochimica Acta 217, 128–143.

Purgstaller, B., Mavromatis, V., Immenhauser, A., Dietzel, M. (2016): *Transformation of Mg-bearing amorphous calcium carbonate to Mg-calcite – In situ monitoring.* Geochimica et Cosmochimica Acta 174, 180–195.

Rasmussen, S.O., Bigler, M., Blockley, S.P., Blunier, T., Buchardt, S.L., Clausen, H.B., Cvijanovic, I., Dahl-Jensen, D., Johnsen, S.J., Fischer, H., Gkinis, V., Guillevic, M., Hoek, W.Z., Lowe, J.J., Pedro, J.B., Popp, T., Seierstad, I.K., Steffensen, J.P., Svensson, A.M., Vallelonga, P., Vinther, B.M., Walker, M.J.C., Wheatley, J.J., Winstrup, M. (2014): *A stratigraphic framework for abrupt climatic changes during the Last Glacial period based on three synchronized Greenland ice-core records: Refining and extending the INTIMATE event stratigraphy.* Quaternary Science Reviews 106, 14–28.

Richter, D.K., Meissner, P., Immenhauser, A., Schulte, U., Dorsten, I. (2010): *Cryogenic and non-cryogenic pool calcites indicating permafrost and non-permafrost periods: A case study from the Herbstlabyrinth-Advent Cave system (Germany).* The Cryosphere 4 (4), 501–509.

Richter, D.K., Neuser, R.D., Voigt, S. (2008): *Kryogene Calcitpartikel aus der Heilenbecker Höhle in Ennepetal (NE Bergisches Land/Nordrhein-Westfalen).* Die Höhle 59 (1-4), 37–47.

Richter, D.K., Riechelmann, D.F. (2008): *Late Pleistocene cryogenic calcite spherolites from the Malachitdom Cave (NE Rhenish Slate Mountains, Germany): origin, unusual internal structure and stable C-O isotope composition.* International Journal of Speleology 37 (2), 119–129.

Rodriguez-Blanco, J.D., Shaw, S., Bots, P., Roncal-Herrero, T., Benning, L.G. (2012): *The role of pH and Mg on the stability and crystallization of amorphous calcium carbonate.* Journal of Alloys and Compounds 536, 477-479.

Sand, K.K., Rodriguez-Blanco, J.D., Makovicky, E., Benning, L.G., Stipp, S.L.S. (2012): *Crystallization of $CaCO_3$ in Water–Alcohol Mixtures: Spherulitic Growth, Polymorph Stabilization, and Morphology Change.* Crystal Growth & Design 12 (2), 842–853.

Self, C.A., Hill, C.A. (2003): *How Speleothems Grow: An Introduction to the Ontogeny od Cave Minerals.* Journal of Cave and Karst Studies 62 (2), 130–151.

Shtukenberg, A.G., Punin, Y.O., Gunn, E., Kahr, B. (2012): *Spherulites.* Chemical reviews 112 (3), 1805–1838.

Socki, R., Niles, P., Fu, Q., Gibson, E. (2010): *Cryogenic Carbonate Formation on Mars: Clues from Stable Isotope Variations seen in Experimental Studies.* Lunar and Planetary Institute Science Conference Abstracts.

Spötl, C. (2008): *Kryogene Karbonate im Höhleneis der Eisriesenwelt.* Die Höhle 59 (1-4).

Spötl, C. (2011): *Long-term performance of the Gasbench isotope ratio mass spectrometry system for the stable isotope analysis of carbonate microsamples.* Rapid communications in mass spectrometry 25 (11), 1683–1685.

Spötl, C., Cheng, H. (2014): *Holocene climate change, permafrost and cryogenic carbonate formation: Insights from a recently deglaciated, high-elevation cave in the Austrian Alps.* Climate of the Past 10 (4), 1349–1362.

Spötl, C., Vennemann, T.W. (2003): *Continuous-flow isotope ratio mass spectrometric analysis of carbonate minerals.* Rapid communications in mass spectrometry 17 (9), 1004–1006.

Stoll, H.M., Müller, W., Prieto, M. (2012): *I-STAL, a model for interpretation of Mg/Ca, Sr/Ca and Ba/Ca variations in speleothems and its forward and inverse application on seasonal to millennial scales.* Geochemistry, Geophysics, Geosystems 13 (9), 114.

Sunagawa, I. (2005): *Crystals: Growth, morphology, and perfection.* Cambridge University Press, Cambridge, 295 pp.

Tremaine, D.M., Froelich, P.N., Wang, Y. (2011): *Speleothem calcite farmed in situ: Modern calibration of $\delta^{18}O$ and $\delta^{13}C$ paleoclimate proxies in a continuously-monitored natural cave system.* Geochimica et Cosmochimica Acta 75 (17), 4929–4950.

Wainer, K., Genty, D., Blamart, D., Daëron, M., Bar-Matthews, M., Vonhof, H., Dublyansky, Y., Pons-Branchu, E., Thomas, L., van Calsteren, P., Quinif, Y., Caillon, N. (2011): *Speleothem record of the last ^{18}O ka in Villars cave (SW France): Investigation of a large $\delta^{18}O$ shift between MIS6 and MIS5.* Quaternary Science Reviews 30 (1-2), 130–146.

Wiedner, E., Scholz, D., Mangini, A., Polag, D., Mühlinghaus, C., Segl, M. (2008): *Investigation of the stable isotope fractionation in speleothems with laboratory experiments.* Quaternary International 187 (1), 15–24.

de Yoreo, J.J. (2003): *Principles of Crystal Nucleation and Growth.* Reviews in Mineralogy and Geochemistry 54 (1), 57–93.

de Yoreo, J.J., Gilbert, P.U.P.A., Sommerdijk, N.A.J.M., Penn, R.L., Whitelam, S., Joester, D., Zhang, H., Rimer, J.D., Navrotsky, A., Banfield, J.F., Wallace, A.F., Michel, F.M., Meldrum, F.C., Cölfen, H., Dove, P.M. (2015): *Crystallization by particle attachment in synthetic, biogenic, and geologic environments.* Science 349 (6247).

Žák, K., Urban, J., Cílek, V., Hercman, H. (2004): *Cryogenic cave calcite from several Central European caves: Age, carbon and oxygen isotopes and a genetic model.* Chemical Geology 206 (1-2), 119–136.

Žák, K., Onac, B.P., Perşoiu, A. (2008): *Cryogenic carbonates in cave environments: A review.* Quaternary International 187 (1), 84–96.

Žák, K., Hercman, H., Orvošová, M., Jačková, I. (2009): *Cryogenic cave carbonates from the Cold Wind Cave, Nízke Tatry Mountains, Slovakia: Extending the age range of cryogenic cave carbonate formation to the Saalian.* International Journal of Speleology 38 (2), 139–152.

Žák, K., Richter, D.K., Filippi, M., Živor, R., Deininger, M., Mangini, A., Scholz, D. (2012): *Coarsely crystalline cryogenic cave carbonate - a new archive to estimate the Last Glacial minimum permafrost depth in Central Europe.* Climate of the Past 8 (6), 1821–1837.

Žák, K., Onac, B.P., Kadebskaya, O., Filippi, M., Dublyansky, Y., Luetscher, M. (2018): *Cryogenic Mineral Formation in Caves,* in: Perşoiu, A., Lauritzen, S.-E. (Eds.), Ice caves, First edition ed. Elsevier, Amsterdam, Netherlands.

Appendix

Cave Plans

The following cave plans depict the caves from which samples presented herein were taken. Red stars mark the chamber(s) where the samples were found.

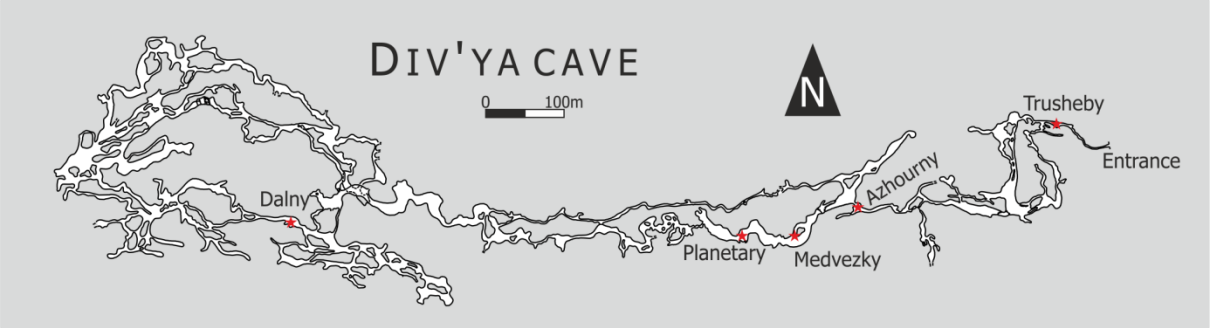

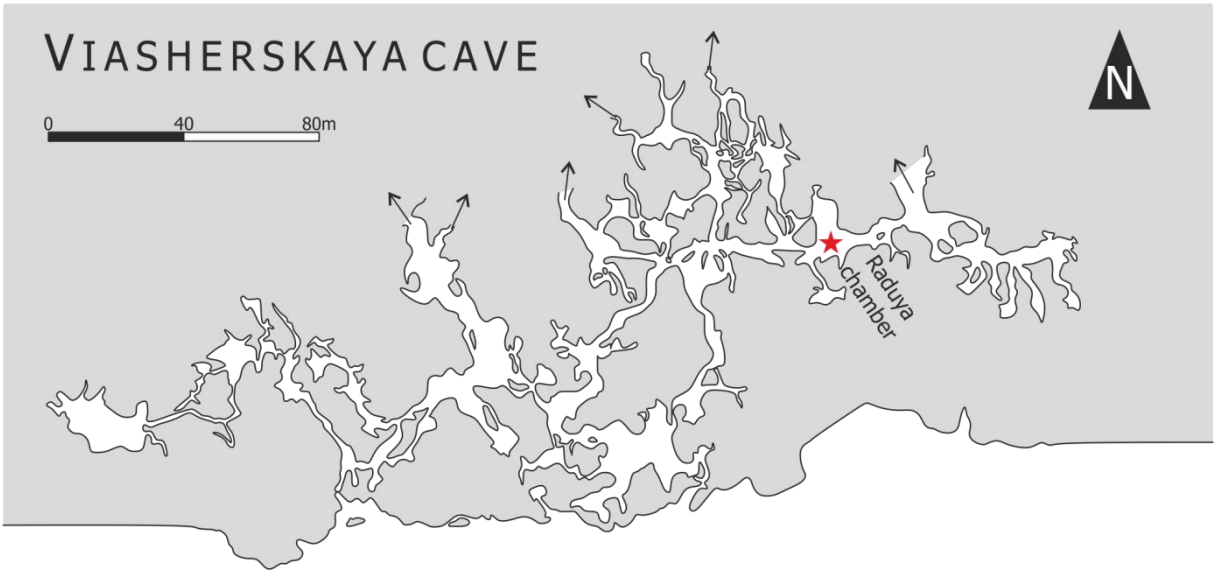

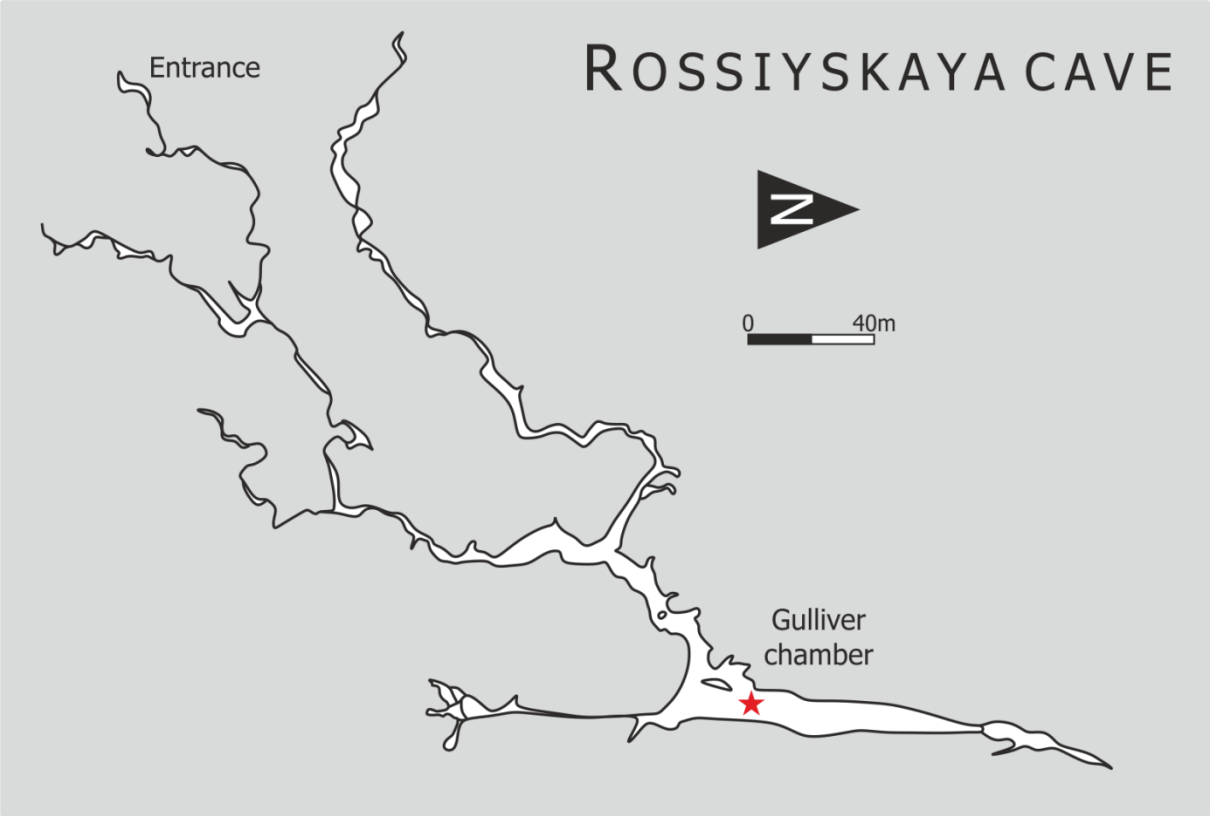
ROSSIYSKAYA CAVE
Entrance
N
0
40m
Gulliver
chamber

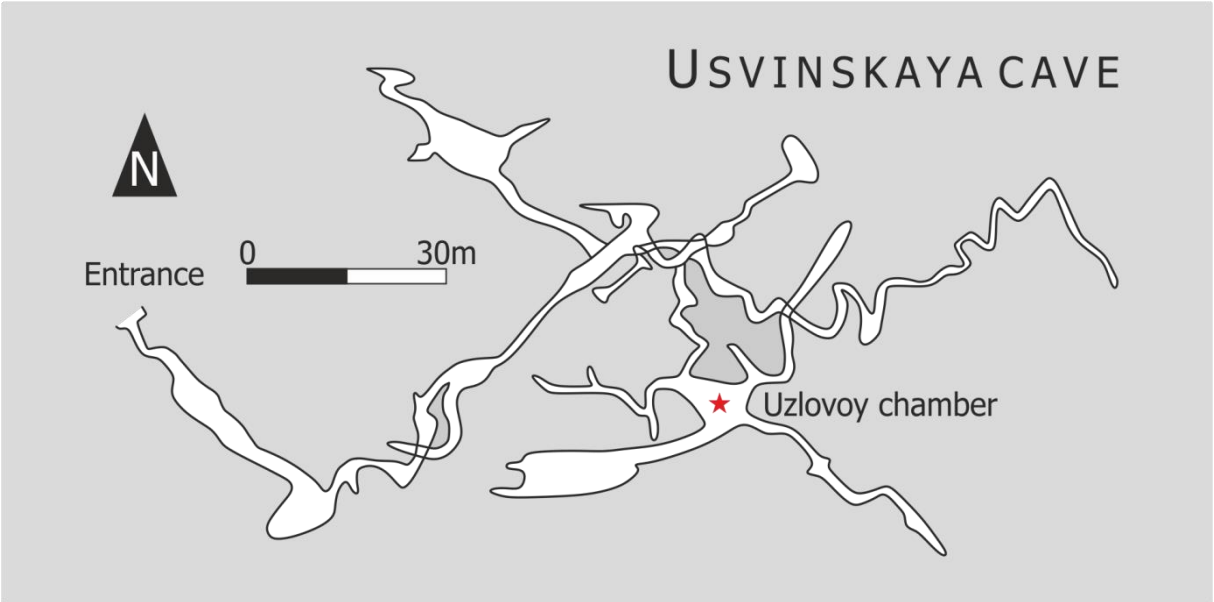
USVINSKAYA CAVE
N
Entrance
0
30m
Uzlovoy chamber

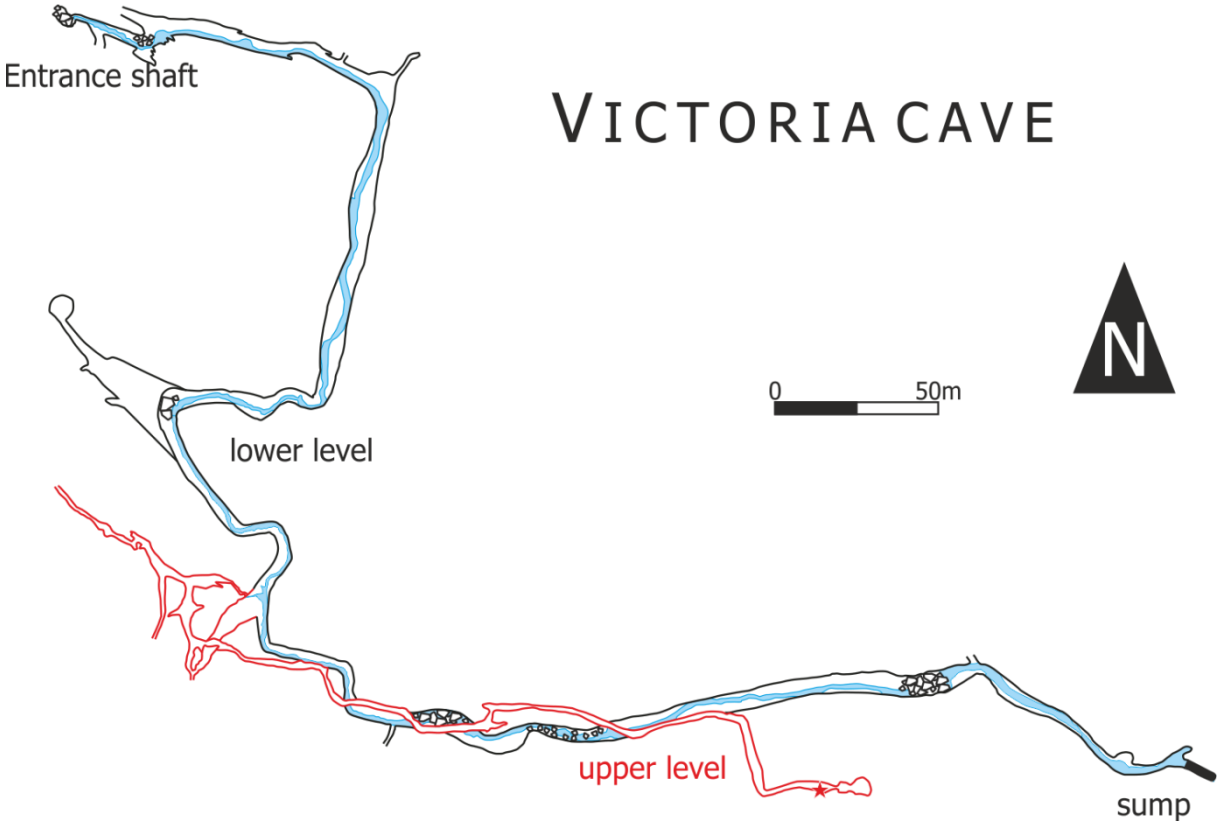
VICTORIA CAVE
Entrance shaft
lower level
upper level
sump
0
50m
N

NU8 sample list

Sample ID	Grainsize	$\delta^{13}C_{cc}$	$\delta^{18}O_{cc}$	notes
NU8_2-4mm-1	2-4 mm	-9.50	-15.29	
NU8_2-4mm-1	2-4 mm	-9.63	-14.97	
NU8_2-4mm-1	2-4 mm	-9.58	-14.93	

Sample ID	Grainsize	δ13Ccc	δ18Occ	notes
NU8_2-4mm-2	2-4 mm	-9.55	-15.40	
NU8_2-4mm-2	2-4 mm	-9.57	-15.10	
NU8_2-4mm-2	2-4 mm	-9.45	-15.03	

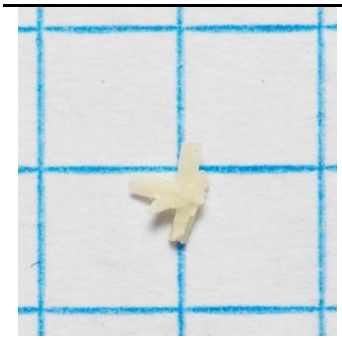

Sample ID	Grainsize	$\delta^{13}C_{cc}$	$\delta^{18}O_{cc}$	notes
NU8_2-4mm-3	2-4 mm	-11.60	-9.84	
NU8_2-4mm-3	2-4 mm	-11.69	-9.81	
NU8_2-4mm-3	2-4 mm	-11.61	-9.63	

Sample ID	Grainsize	$\delta^{13}C_{cc}$	$\delta^{18}O_{cc}$	notes
NU8_2-4mm-4	2-4 mm	-7.49	-16.48	
NU8_2-4mm-4	2-4 mm	-7.36	-16.42	
NU8_2-4mm-4	2-4 mm	-7.33	-16.38	

Sample ID	Grainsize	$\delta^{13}C_{cc}$	$\delta^{18}O_{cc}$	notes
NU8_2-4mm-5	2-4 mm	-9.76	-15.06	
NU8_2-4mm-5	2-4 mm	-9.74	-15.02	
NU8_2-4mm-5	2-4 mm	-9.61	-14.88	

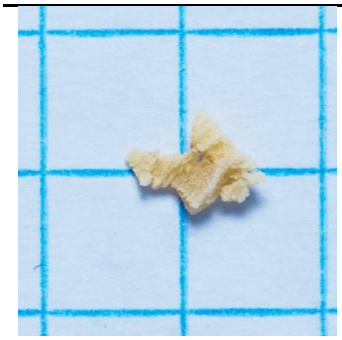

Sample ID	Grainsize	$\delta^{13}C_{cc}$	$\delta^{18}O_{cc}$	notes
NU8_2-4mm-6	2-4 mm	-6.50	-16.23	
NU8_2-4mm-6	2-4 mm	-6.49	-16.00	
NU8_2-4mm-6	2-4 mm	-6.45	-15.92	

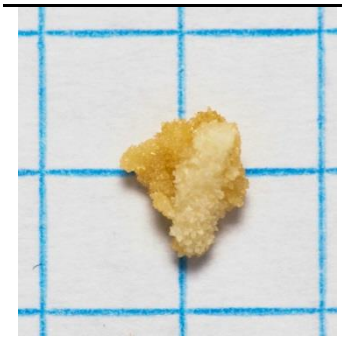

Sample ID	Grainsize	$\delta^{13}C_{cc}$	$\delta^{18}O_{cc}$	notes
NU8_2-4mm-7	2-4 mm	-9.54	-12.33	
NU8_2-4mm-7	2-4 mm	-9.71	-11.99	
NU8_2-4mm-7	2-4 mm	-9.74	-11.80	

Sample ID	Grainsize	$\delta^{13}C_{cc}$	$\delta^{18}O_{cc}$	notes
NU8_2-4mm-8	2-4 mm	-10.62	-9.56	
NU8_2-4mm-8	2-4 mm	-10.66	-9.35	
NU8_2-4mm-8	2-4 mm	-10.60	-9.34	

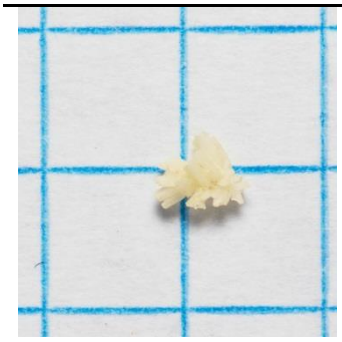

Sample ID	Grainsize	$\delta^{13}C_{cc}$	$\delta^{18}O_{cc}$	notes
NU8_2-4mm-9	2-4 mm	-11.60	-9.93	
NU8_2-4mm-9	2-4 mm	-11.65	-9.79	
NU8_2-4mm-9	2-4 mm	-11.61	-9.77	

Sample ID	Grainsize	$\delta^{13}C_{cc}$	$\delta^{18}O_{cc}$	notes
NU8_2-4mm-10	2-4 mm	-7.03	-18.06	
NU8_2-4mm-10	2-4 mm	-7.19	-17.88	
NU8_2-4mm-10	2-4 mm	-7.03	-17.77	

Sample ID	Grainsize	$\delta^{13}C_{cc}$	$\delta^{18}O_{cc}$	notes
NU8_2-4mm-11	2-4 mm	-5.86	-21.58	
NU8_2-4mm-11	2-4 mm	-6.01	-21.54	
NU8_2-4mm-11	2-4 mm	-5.83	-21.53	

Sample ID	Grainsize	$\delta^{13}C_{cc}$	$\delta^{18}O_{cc}$	notes
NU8_2-4mm-12	2-4 mm	-6.78	-18.19	
NU8_2-4mm-12	2-4 mm	-6.66	-18.13	
NU8_2-4mm-12	2-4 mm	-6.70	-18.08	

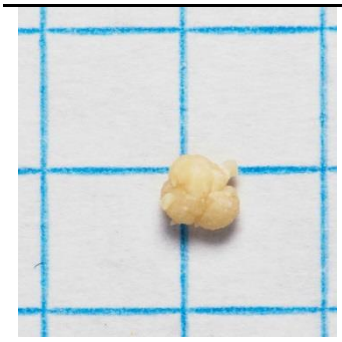

Sample ID	Grainsize	$\delta^{13}C_{cc}$	$\delta^{18}O_{cc}$	notes
NU8_2-4mm-13	2-4 mm	-6.23	-20.52	
NU8_2-4mm-13	2-4 mm	-6.25	-20.49	
NU8_2-4mm-13	2-4 mm	-6.34	-20.42	

Sample ID	Grainsize	$\delta^{13}C_{cc}$	$\delta^{18}O_{cc}$	notes
NU8_2-4mm-14	2-4 mm	-7.18	-18.12	
NU8_2-4mm-14	2-4 mm	-7.10	-18.07	
NU8_2-4mm-14	2-4 mm	-7.09	-18.05	

Sample ID	Grainsize	$\delta^{13}C_{cc}$	$\delta^{18}O_{cc}$	notes
NU8_2-4mm-15	2-4 mm	-1.07	-27.86	
NU8_2-4mm-15	2-4 mm	-1.12	-27.82	
NU8_2-4mm-15	2-4 mm	-1.27	-27.79	

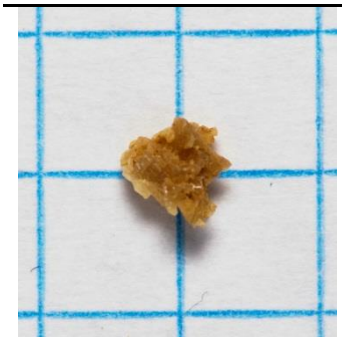

Sample ID	Grainsize	$\delta^{13}C_{cc}$	$\delta^{18}O_{cc}$	notes
NU8_2-4mm-16	2-4 mm	-5.76	-19.00	
NU8_2-4mm-16	2-4 mm	-5.69	-18.97	
NU8_2-4mm-16	2-4 mm	-5.90	-18.86	

Sample ID	Grainsize	$\delta^{13}C_{cc}$	$\delta^{18}O_{cc}$	notes
NU8_2-4mm-17	2-4 mm	-7.10	-18.26	
NU8_2-4mm-17	2-4 mm	-7.02	-17.99	

Sample ID	Grainsize	$\delta^{13}C_{cc}$	$\delta^{18}O_{cc}$	notes
NU8_2-4mm-18	2-4 mm	-9.66	-15.30	
NU8_2-4mm-18	2-4 mm	-9.80	-15.18	
NU8_2-4mm-18	2-4 mm	-9.58	-15.16	

Sample ID	Grainsize	$\delta^{13}C_{cc}$	$\delta^{18}O_{cc}$	notes
NU8_2-4mm-19	2-4 mm	-6.44	-18.86	
NU8_2-4mm-19	2-4 mm	-6.62	-18.83	
NU8_2-4mm-19	2-4 mm	-6.43	-18.69	

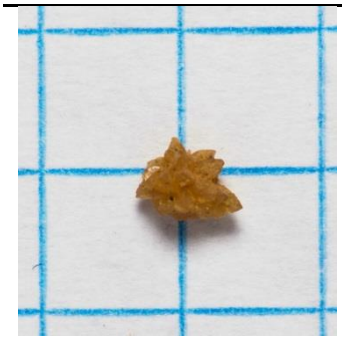

Sample ID	Grainsize	$\delta^{13}C_{cc}$	$\delta^{18}O_{cc}$	notes
NU8_2-4mm-20	2-4 mm	-4.86	-17.04	
NU8_2-4mm-20	2-4 mm	-4.75	-17.01	
NU8_2-4mm-20	2-4 mm	-4.78	-16.92	

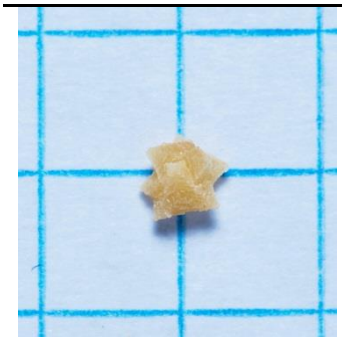

Sample ID	Grainsize	$\delta^{13}C_{cc}$	$\delta^{18}O_{cc}$	notes
NU8_2-4mm-21	2-4 mm	-7.51	-16.89	
NU8_2-4mm-21	2-4 mm	-7.47	-16.83	
NU8_2-4mm-21	2-4 mm	-7.39	-16.83	

Sample ID	Grainsize	$\delta^{13}C_{cc}$	$\delta^{18}O_{cc}$	notes
NU8_2-4mm-22	2-4 mm	-7.35	-12.96	
NU8_2-4mm-22	2-4 mm	-7.38	-12.91	
NU8_2-4mm-22	2-4 mm	-7.31	-12.77	

Sample ID	Grainsize	$\delta^{13}C_{cc}$	$\delta^{18}O_{cc}$	notes
NU8_2-4mm-23	2-4 mm	-7.31	-17.94	
NU8_2-4mm-23	2-4 mm	-7.17	-17.91	
NU8_2-4mm-23	2-4 mm	-7.21	-17.91	

Sample ID	Grainsize	$\delta^{13}C_{cc}$	$\delta^{18}O_{cc}$	notes
NU8_2-4mm-24	2-4 mm	-2.43	-25.99	
NU8_2-4mm-24	2-4 mm	-2.39	-25.90	
NU8_2-4mm-24	2-4 mm	-2.72	-25.81	

Sample ID	Grainsize	$\delta^{13}C_{cc}$	$\delta^{18}O_{cc}$	notes
NU8_2-4mm-25	2-4 mm	-7.18	-17.74	
NU8_2-4mm-25	2-4 mm	-7.11	-17.72	
NU8_2-4mm-25	2-4 mm	-7.46	-17.54	

Sample ID	Grainsize	$\delta^{13}C_{cc}$	$\delta^{18}O_{cc}$	notes
NU8_2-4mm-26	2-4 mm	-7.84	-17.63	
NU8_2-4mm-26	2-4 mm	-7.79	-17.60	
NU8_2-4mm-26	2-4 mm	-7.88	-17.57	

Sample ID	Grainsize	$\delta^{13}C_{cc}$	$\delta^{18}O_{cc}$	notes
NU8_4mm-1	> 4 mm	-9.31	-14.89	
NU8_4mm-1	> 4 mm	-9.07	-15.25	rim

Sample ID	Grainsize	$\delta^{13}C_{cc}$	$\delta^{18}O_{cc}$	notes
NU8_4mm-2	> 4 mm	-9.36	-14.87	core
NU8_4mm-2	> 4 mm	-9.73	-14.96	rim

Sample ID	Grainsize	$\delta^{13}C_{cc}$	$\delta^{18}O_{cc}$	notes
NU8_4mm-3	> 4 mm	-9.96	-13.93	core
NU8_4mm-3	> 4 mm	-9.37	-14.52	rim

Sample ID	Grainsize	$\delta^{13}C_{cc}$	$\delta^{18}O_{cc}$	notes
NU8_4mm-4	> 4 mm	-7.03	-18.68	
NU8_4mm-4	> 4 mm	-6.88	-18.93	

Sample ID	Grainsize	$\delta^{13}C_{cc}$	$\delta^{18}O_{cc}$	notes
NU8_4mm-5	> 4 mm	-7.86	-10.80	
NU8_4mm-5	> 4 mm	-9.34	-11.71	

Sample ID	Grainsize	$\delta^{13}C_{cc}$	$\delta^{18}O_{cc}$	notes
NU8_4mm-6	> 4 mm	-7.37	-16.42	core
NU8_4mm-6	> 4 mm	-7.09	-17.47	rim

Sample ID	Grainsize	$\delta^{13}C_{cc}$	$\delta^{18}O_{cc}$	notes
NU8_4mm-7	> 4 mm	-6.39	-17.12	core
NU8_4mm-7	> 4 mm	-4.71	-19.18	rim

Sample ID	Grainsize	$\delta^{13}C_{cc}$	$\delta^{18}O_{cc}$	notes
NU8_4mm-8	> 4 mm	-7.56	-16.05	

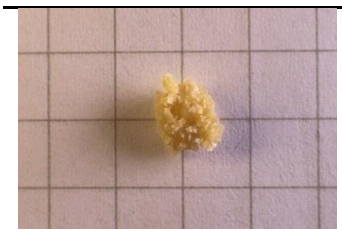

Sample ID	Grainsize	$\delta^{13}C_{cc}$	$\delta^{18}O_{cc}$	notes
NU8_4mm-9	> 4 mm	-9.79	-12.49	
NU8_4mm-9	> 4 mm	-9.96	-12.40	

Sample ID	Grainsize	$\delta^{13}C_{cc}$	$\delta^{18}O_{cc}$	notes
NU8_4mm-10	> 4 mm	-7.15	-15.21	

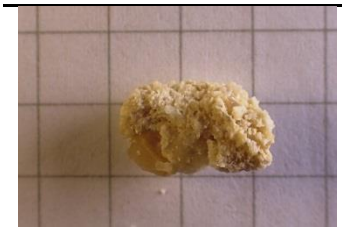

Sample ID	Grainsize	$\delta^{13}C_{cc}$	$\delta^{18}O_{cc}$	notes
NU8_4mm-11	> 4 mm	-6.94	-16.59	fine
NU8_4mm-11	> 4 mm	-6.71	-16.95	coarse

Sample ID	Grainsize	$\delta^{13}C_{cc}$	$\delta^{18}O_{cc}$	notes
NU8_4mm-12	> 4 mm	-4.24	-19.47	
NU8_4mm-12	> 4 mm	-4.30	-19.47	

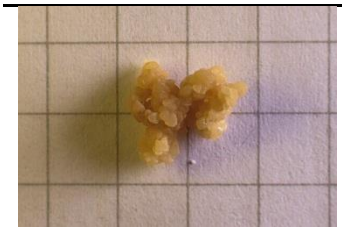

Sample ID	Grainsize	$\delta^{13}C_{cc}$	$\delta^{18}O_{cc}$	notes
NU8_4mm-13	> 4 mm	-8.84	-11.03	
NU8_4mm-13	> 4 mm	-8.98	-10.80	

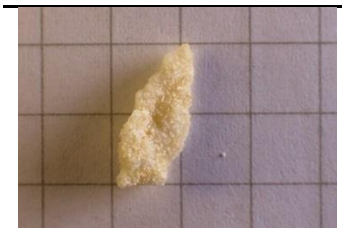

Sample ID	Grainsize	$\delta^{13}C_{cc}$	$\delta^{18}O_{cc}$	notes
NU8_4mm-14	> 4 mm	-8.19	-15.45	
NU8_4mm-14	> 4 mm	-8.37	-15.49	

Sample ID	Grainsize	$\delta^{13}C_{cc}$	$\delta^{18}O_{cc}$	notes
NU8_4mm-15	> 4 mm	-8.37	-15.19	clean
NU8_4mm-15	> 4 mm	-7.92	-15.84	coated

Sample ID	Grainsize	$\delta^{13}C_{cc}$	$\delta^{18}O_{cc}$	notes
NU8_4mm-16	> 4 mm	-5.32	-13.60	coating
NU8_4mm-16	> 4 mm	-6.04	-19.04	

Sample ID	Grainsize	$\delta^{13}C_{cc}$	$\delta^{18}O_{cc}$	notes
NU8_4mm-17	> 4 mm	-10.30	-14.28	
NU8_4mm-17	> 4 mm	-10.30	-14.21	

Sample ID	Grainsize	$\delta^{13}C_{cc}$	$\delta^{18}O_{cc}$	notes
NU8_4mm-18	> 4 mm	-8.59	-12.28	
NU8_4mm-18	> 4 mm	-6.59	-12.97	

Sample ID	Grainsize	$\delta^{13}C_{cc}$	$\delta^{18}O_{cc}$	notes
NU8_4mm-19	> 4 mm	-6.33	-12.75	
NU8_4mm-19	> 4 mm	-6.26	-12.45	

Sample ID	Grainsize	$\delta^{13}C_{cc}$	$\delta^{18}O_{cc}$	notes
NU8_4mm-20	> 4 mm	-1.48	-26.06	core
NU8_4mm-20	> 4 mm	-2.04	-23.77	rim

Sample ID	Grainsize	$\delta^{13}C_{cc}$	$\delta^{18}O_{cc}$	notes
NU8_4mm-21	> 4 mm	-7.50	-11.67	core
NU8_4mm-21	> 4 mm	-4.27	-20.32	rim

Sample ID	Grainsize	$\delta^{13}C_{cc}$	$\delta^{18}O_{cc}$	notes
NU8_4mm-22	> 4 mm	-0.42	-29.11	core
NU8_4mm-22	> 4 mm	0.13	-28.85	rim

Sample ID	Grainsize	$\delta^{13}C_{cc}$	$\delta^{18}O_{cc}$	notes
NU8_4mm-23	> 4 mm	-5.16	-17.50	light
NU8_4mm-23	> 4 mm	-3.91	-21.88	dark

Thermometry Results

Table 7: Calculated temperatures using measured $\delta^{18}O_{water}$ values as input. Temperatures are reported in °C.

	Coplen (2007)	Friedman & O'Neil (1977)	Craig (1965)	Kim & O'Neil (1997)	Tremaine et al. (2011)	Dettman et al. (1999)
DIV01b	41.1	33.0	33.9	31.5	40.3	32.0
DIV01d	27.0	20.4	21.5	18.7	25.2	18.5
DIV02b	15.4	10.3	11.9	8.0	12.8	7.8
DIV03a	55.0	45.9	46.3	44.1	55.3	45.9
DIV04a	68.7	59.1	58.9	56.4	70.2	60.3
DIV04b	61.8	52.3	52.5	50.1	62.6	52.9
DIV38ia	15.8	10.6	12.2	8.4	13.2	8.1
DIV38ob	11.8	7.3	9.1	4.7	9.0	4.6
DIV38oc	11.8	7.3	9.1	4.7	9.0	4.6
NU8a	9.0	4.9	7.0	2.2	6.1	2.1
NU8b	-4.0	-6.0	-2.2	-9.8	-7.7	-9.3
ROS01a	13.3	8.5	10.3	6.1	10.6	5.9
USV01a	32.1	24.9	25.8	23.3	30.6	23.3
USV01b	8.2	4.2	6.4	1.4	5.2	1.4
USV02a	52.5	43.5	44.0	41.8	52.5	43.3
USV02b	30.3	23.3	24.3	21.7	28.7	21.6
USV02c	48.6	39.9	40.5	38.3	48.4	39.5
USV03a	8.0	4.1	6.2	1.3	5.0	1.2
VIA01a	35.3	27.8	28.6	26.2	34.0	26.3
VIA01b	-28.3	-25.6	-14.4	-32.4	-33.1	-29.7
VIA01c	-12.7	-13.1	-7.4	-17.9	-16.8	-16.7

Table 8: Calculated temperatures using projected $\delta^{18}O_{water}$ values from $d^{2}H_{water}$ onto the global meteoric water line as input. Temperatures are reported in °C.

	Coplen (2007)	Friedman & O'Neil (1977)	Craig (1965)	Kim & O'Neil (1997)	Tremaine et al. (2011)	Dettman et al. (1999)
DIV01b	22.7	16.7	17.9	14.7	20.6	14.5
DIV01d	19.5	13.9	15.3	11.8	17.2	11.6
DIV02b	17.8	12.4	13.9	10.3	15.4	10.0
DIV03a	71.8	62.1	61.7	59.1	73.5	63.7
DIV04a	47.8	39.2	39.7	37.5	47.5	38.6
DIV04b	49.2	40.4	41.0	38.8	49.0	40.0
DIV38ia	14.7	9.7	11.4	7.4	12.1	7.2
DIV38ob	14.6	9.6	11.3	7.3	11.9	7.1
DIV38oc	14.6	9.6	11.3	7.3	11.9	7.1
NU8a	17.4	12.0	13.5	9.8	14.9	9.6
NU8b	16.6	11.4	12.9	9.2	14.1	8.9
ROS01a	17.6	12.2	13.7	10.0	15.1	9.8
USV01a	34.6	27.1	28.0	25.6	33.3	25.7
USV01b	29.3	22.5	23.5	20.8	27.7	20.7
USV02a	41.5	33.4	34.1	31.9	40.7	32.4
USV02b	40.7	32.6	33.4	31.1	39.8	31.6
USV02c	56.7	47.5	47.8	45.6	57.1	47.6
USV03a	18.5	13.0	14.4	10.9	16.1	10.6
VIA01a	44.1	35.7	36.4	34.2	43.5	34.9
VIA01b	39.2	31.3	32.1	29.8	38.2	30.1
VIA01c	52.9	43.9	44.4	42.2	53.0	43.8

52°E 54°E 56°E 58°E 60°E 62°E 64°E

62°N 60°N 58°N 56°N 54°N 52°N

N

Mountains

Ural

DIV

VIA

ROS

USV

VIC

Nyagan

Serov

Berezniki

Perm

Nizhny Tagil

Pervouralsk

Yekaterinburg

Izhevsk

Birsk

Ufa

Zlatoust

Chelyabinsk

Kurgan

Sterlitamak

Magnitogorsk

Oostanay

Orenburg

1:6 000 000

Kilometers

0 50 100 200 300 400

Coordinate System: WGS 1984 Web Mercator Auxiliary Sphere
Projection: Mercator Auxiliary Sphere
Datum: WGS 1984
Central Meridian: 0.0
Standard Parallel 1: 0.0
Auxiliary Sphere Type: 0.0
Units: Meter

Caves

- Northern Ural
- Central Ural
- Southern Ural

Modern Permafrost

- continuous (90-100%)
- discontinuous (50-90%)
- sporadic (10-50%)
- isolated (0-10%)

Topography

1800 m a.s.l.

-200 m a.s.l.

- Lakes
- Rivers

Numerical Model

April 5, 2018

This script is a simple numerical forward model similar to a model described in Zak et al. (2004). For a detailled description on the additions, the reader is referred to the main text. The code is written in python 3.6.

```
In [1]: import numpy as np
        import pandas as pd
        import matplotlib.pyplot as plt
```

Since we're working with oxygen isotopes in both VSMOW and VPDB standards, we'll probably need to convert between the two at one stage. Here the two conversion functions are defined:

```
In [2]: def toVPDB( delta ):
            return 0.97001 * delta - 29.99

        def toVSMOW( delta ):
            return 1.03092 * delta + 30.92
```

1 Rayleigh Process

Here we define the rayleigh process. The function takes a starting isotopic composition delta0 and a process specific fractionation factor alpha as arguments. It returns a dataframe containing the isotopic composition of the product phase and the residuum. δ-values are calculated at a resolution of 0.1% of freezing from 0.1 to 99.9%.

The notation of fractionation factors is important:

a_product_educt

for example: if we use this function to model the isotopic evolution of rain (product) from water vapour (educt), the rain will be isotopically heavier than the cloud it condensed from. This means that $\alpha_{rain-vapour} > 1$.

The 'educt' column will contain the isotopic evolution of the water vapour, and the 'product' column will contain the values for the corresponding rain condensing from that vapour.

```
In [3]: def rayleigh( delta0, alpha ):

            fraction = np.linspace( 1, 0, 1001 )
            delta_e = ( delta0 + 1000 ) * fraction ** ( alpha - 1 ) - 1000 #educt
            delta_p = alpha * ( delta_e + 1000 ) - 1000 #product

            d = np.array( ( delta_e, delta_p) ).transpose( )
```

```
    ans = pd.DataFrame( data = d,
                        index = fraction,
                        columns = [ 'educt', 'product' ] )

    return ans.drop( ans.tail( 1 ).index )
```

2 Fractionation Factors

```
In [4]: a_ice_water = 1.0029 # Lehmann & Siegenthaler (1991)
        a_cc_water = 1.0359 # Friedman & O'neil (1977)
        a_co2_hco3 = 0.9892 # Mook et al (2000)
        a_cc_hco3 = 0.9996 # Mook et al. (2000)
```

3 Initialisation

These variables represent the initial isotopic composition of seepage waters with respect to $\delta^{18}O_{water}$ and $\delta^{13}C_{HCO3}$ at the onset of CCC precipitation.

```
In [5]: init_water = -13 #VSMOW
        init_hco3 = -12 #VPDB
```

3.1 calcite $\delta^{18}O$

```
In [6]: O18_water = rayleigh( init_water,
                              a_ice_water ) #educt is water, product is ice

        O18_cc = toVPDB( a_cc_water * ( O18_water[ 'educt' ] + 1000) - 1000 )
```

3.2 calcite $\delta^{13}C$

3.2.1 open system

```
In [7]: C13_hco3_o = rayleigh( init_hco3,
                               a_co2_hco3 ) #educt is hco3, product is co2

        C13_cc_o = ( a_cc_hco3 * ( C13_hco3_o[ 'educt' ] + 1000 ) - 1000 )
```

```
C:\ProgramData\Anaconda3\lib\site-packages\ipykernel_launcher.py:4: RuntimeWarning: divide by ze
  after removing the cwd from sys.path.
```

3.2.2 closed system

```
In [8]: C13_cc_c = rayleigh( init_hco3,
                             a_cc_hco3 )
```

```
C:\ProgramData\Anaconda3\lib\site-packages\ipykernel_launcher.py:4: RuntimeWarning: divide by ze
  after removing the cwd from sys.path.
```

3.2.3 semi-closed system

```
In [9]: x = np.linspace( 0, 1, 11 )

        a_tot = ( x * a_cc_hco3 + ( 1-x ) * a_co2_hco3 ) / ( 2 * 0.5 )

        C13_cc = [ ]


        for a in a_tot:

            C13_hco3 = rayleigh( init_hco3,
                                 a).educt #educt is hco3, product is calcite

            ans = ( a_cc_hco3 * ( C13_hco3 + 1000 ) - 1000 )

            C13_cc.append( ans )
```

```
C:\ProgramData\Anaconda3\lib\site-packages\ipykernel_launcher.py:4: RuntimeWarning: divide by ze
  after removing the cwd from sys.path.
```

4 Plots

The following section of the code generate the figures depicted in the main text boby to visualize modelling results.

4.1 isotopic evolution

```
In [10]: from cycler import cycler
         #color cycle
         clrs = [
                 'xkcd:azure',
                 'xkcd:navy',
                 'xkcd:green',
                 'xkcd:dark red',
                ]

         ######################################################################

         f, ax = plt.subplots( figsize = ( 8, 4 ),
                               dpi = 200 )

         ax.set_prop_cycle( cycler( 'color',
                                    clrs ) )

         ######################################################################
```

```
ax.plot( O18_water[ 'educt' ],
         linewidth = 0.5 )

ax.plot( O18_water[ 'product' ],
         linewidth = 0.5 )

ax.plot( O18_cc,
         linewidth = 0.5 )

######################################################################
n = 1 / ( len( C13_cc ) )

for i in C13_cc:

    ax.plot( i,
             linewidth = 0.5,
             color = 'xkcd:dark red',
             alpha = n )

    n += 1 / ( len( C13_cc ) + 1 )

######################################################################

Litems = [
          r'$\delta^{18}O_{water}$ [VSMOW]',
          r'$\delta^{18}O_{ice}$ [VSMOW]',
          r'$\delta^{18}O_{cc}$ [VPDB]',
          r'$\delta^{13}C_{cc}$ [VPDB]'
         ]

plt.legend( Litems,
            fontsize = 7,
            ncol = 2,
            loc = 1 )

plt.gca( ).invert_xaxis( )
ax.grid( linewidth = 0.2 )

ax.set_ylim( -31, 11 )

ax.set_ylabel( r'$\delta$ values' )
ax.set_xlabel( 'residual fraction of water' )

######################################################################

plt.savefig( 'isotopes1.svg',
             format = 'svg' )
```

```
f
```

Out[10]:

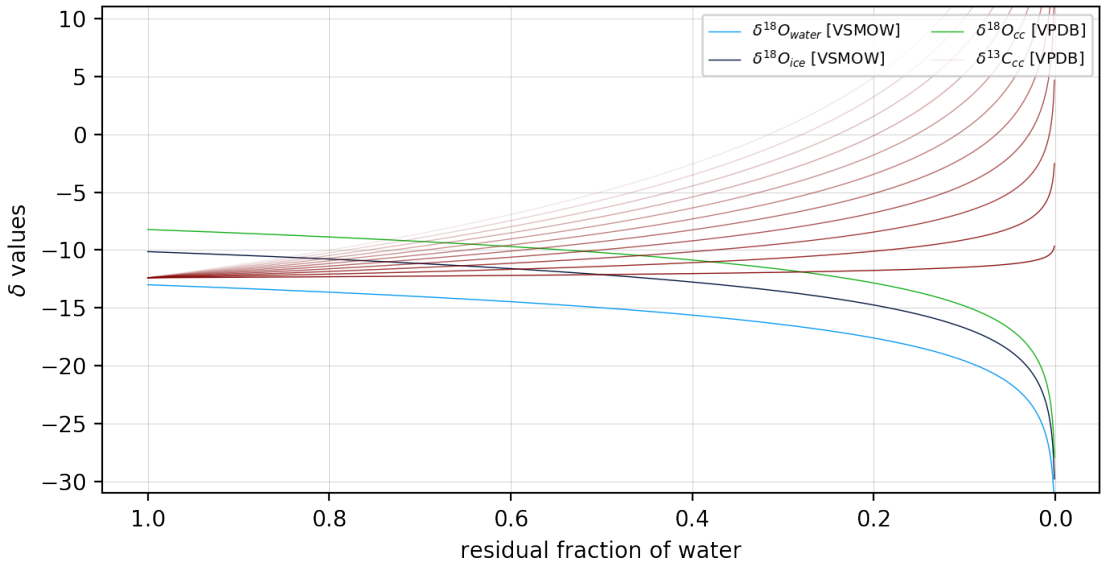

4.2 model validation

```
In [11]: df = pd.read_excel( 'Profiles.xlsx' )
         Samples = [
                    'DIV01',
                    'DIV02',
                    'DIV03',
                    'DIV04',
                    'DIV05',
                    'DIV38',
                    'ROS01',
                    'USV02',
                    'VIA01'
                   ]

         NU8 = pd.read_excel( 'NU8_SIdata.xls' )

         ########################################################################

         f2, ax2 = plt.subplots( figsize = ( 8, 5 ),
                                 dpi = 200 )


         ########################################################################
```

```
symbols = [
            'v',
            '<',
            '^',
            '>',
            'o',
            's',
            'p',
            'X',
            'P'
          ]

n = 0

for smpl in Samples:

    cols = [ col for col in df.columns if smpl in col ]

    ax2.plot( df[ cols[ 1 ] ],
              df[ cols[ 0 ] ],
              symbols[ n ],
              ms = 5,
              markeredgecolor = 'w',
              markeredgewidth = 0.2,
              color = 'xkcd:azure',
              label = smpl)
    n += 1

ax2.plot( NU8.del18O,
          NU8.del13C,
          'o',
          ms = 3,
          markeredgecolor = 'w',
          markeredgewidth = 0.2,
          color = 'xkcd:azure',
          label = 'NU8' )

#########################################################################

X = O18_cc
Y3 = C13_cc

n = 1 / ( len( C13_cc ) )

for i in C13_cc:
    ax2.plot( X,
              i,
```

```
                linewidth = 0.5,
                color = 'k',
                alpha = n )

        n += 1 / ( len( C13_cc ) + 1 )

    ######################################################################


    items = [
                'DIV01',
                'DIV02',
                'DIV03',
                'DIV04',
                'DIV05',
                'DIV38',
                'ROS01',
                'USV02',
                'VIA01',
                'NU8',
                'modelled data'
            ]

    ax2.legend( items,
                fontsize = 7,
                ncol = 2,
                loc = 1 )

    ax2.grid( linewidth = 0.2 )

    ax2.set_ylabel( r'$\delta^{13}C_{cc}$',
                    fontsize = 9 )
    ax2.set_xlabel( r'$\delta^{18}O_{cc}$',
                    fontsize = 9 )

    ax2.set_yticks( np.linspace( -12, 2, 8 ) )
    ax2.set_ylim( -13, 3 )
    ax2.set_xlim( -31, -8 )

    ######################################################################

    plt.savefig( 'isotopes2.svg',
                 format = 'svg' )

    f2
```

Out[11]:

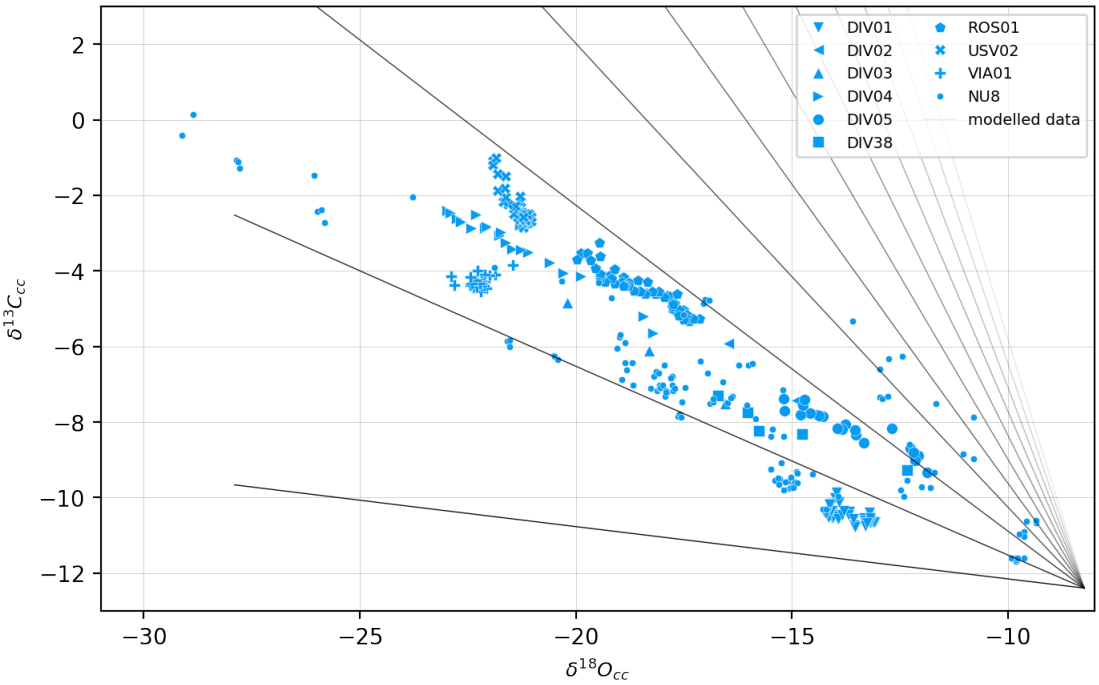
DIV01
DIV02
DIV03
DIV04
DIV05
DIV38
ROS01
USV02
VIA01
NU8
modelled data
2
0
−2
−4
−6
−8
−10
−12
−30
−25
−20
−15
−10
$\delta^{13}C_{cc}$
$\delta^{18}O_{cc}$